

Fall 12-18-2015

Three Dimensional Nanowire Array Piezo-phototronic and Piezo- photo-magnetotronic Sensors

Satish C. Rai
University of New Orleans, bhu.satish@gmail.com

Follow this and additional works at: <https://scholarworks.uno.edu/td>



Part of the [Nanoscience and Nanotechnology Commons](#)

Recommended Citation

Rai, Satish C., "Three Dimensional Nanowire Array Piezo-phototronic and Piezo-photo-magnetotronic Sensors" (2015). *University of New Orleans Theses and Dissertations*. 2104.
<https://scholarworks.uno.edu/td/2104>

This Dissertation is protected by copyright and/or related rights. It has been brought to you by ScholarWorks@UNO with permission from the rights-holder(s). You are free to use this Dissertation in any way that is permitted by the copyright and related rights legislation that applies to your use. For other uses you need to obtain permission from the rights-holder(s) directly, unless additional rights are indicated by a Creative Commons license in the record and/or on the work itself.

This Dissertation has been accepted for inclusion in University of New Orleans Theses and Dissertations by an authorized administrator of ScholarWorks@UNO. For more information, please contact scholarworks@uno.edu.

Three Dimensional Nanowire Array Piezo-phototronic and Piezo-photo-magnetotronic Sensors

A Dissertation

Submitted to the Graduate Faculty of the
University of New Orleans
in partial fulfillment of the
requirements for the degree of

Doctor of Philosophy
in
Engineering and Applied Science
Physics

By

Satish Chandra Rai

M.Tech. Indian Institute of Technology-Banaras Hindu University, 2008
M.S. Banaras Hindu University, 2005

December, 2015

Copyright 2015, Satish Chandra Rai

“To Almighty”

Acknowledgements

I would like to express my gratitude to my mentor Prof. Weilie Zhou who primarily provided me an opportunity to be a part of his group and had been consistently thoughtful about my research progress with timely input to avoid and remove deadlocks arising in my research endeavor.

I am grateful to my committee members Profs. Kevin L. Stokes, Leszek Malkinski, Ashok Puri and Paul J. Schilling for agreeing to be in my doctoral committee and the mentoring they provided during the period of my doctoral work.

I would like to express my thankfulness to my collaborators Profs. Scott M. Grayson, Yong Zhang and Zhong Lin Wang for their scientific advice and contributions in making of this dissertation. I am indebted Prof. Yong Zhang for PL measurements and Prof. Zhong Lin Wang for electron microscopy characterizations. Their feedback about fundamentals of semiconducting materials optical and piezo-phototronic behavior have nourished my intellect towards a better understanding.

I would like to have this chance to appreciate the training on various scientific instruments and help I received from my former group members Dr. Baobao Chao, Dr. Kun Yao, Dr. Jiajun Chen, Dr. Kai Wang that made this dissertation evolve in its current format. Especially, I would like to thank Drs. Jiajun Chen and Kai Wang for teaching me many aspect of materials synthesis, characterization and device fabrication and measurement along with scientific discussion on the content of the dissertation. I would also like to express my sense of gratitude to my friends Dr. Sarah Wozny, Dr. Hui Ma and Dr. Haiqiao Su with whom I have pleasure sharing the office. I

would also acknowledge the bright thoughts that my friends Zhi Zheng, Shuke Yan, Nooraldin Alkurd, Manish Bhatt shared to me.

I would like to thank Dr. Yong Ding for carrying out electron microscopy characterization, Jason K. Marmon for carrying out PL measurements and Dr. Ejaz Mohammad with whom I learned a bit about polymer chemistry.

Here I would like to acknowledge my friends Dr. Shiva Adireddy, Dr. Debashish Mahanty, Dr. Girija Choubey, Dr. Dinesh Mishra, Abhishek Srivastava, Rahmatollah Eskandari, Taha Rostamzadeh, Darius Montasserasadi and Shankar Khanal for the fun filled time spent at UNO.

I am thankful to present and past AMRI office staff Poncho De Leon, Jennifer Tickle, and Amanda Lamastus for their help in making the paperwork and chemical purchasing easier and swift. I am also indebted to Harry J. Rees for troubleshooting and fixing of key instruments vital to my research work.

No word of gratitude is sufficient to express my thankfulness to my mother and my sister Amrita who, in spite of being far away, provided me emotional support over the course of my stay at UNO. I'd especially thank my wife Akanksha for her unconditional and untiring support whom I also consider an excellent human being and feel blessed to have her in my life and owe a lot to her for the sacrifices she made for our family. My little bundle of joy, my son Adwik is an angel who played a key role in making my life happier than I could have ever imagined and I consider him a blessing.

I would like to thank office of research/UNO for assistantship support and financial support for the research work by the DARPA Grant No.HR0011-07-1-0032 and research grants from

Louisiana Board of Regents Contract Nos. LEQSF (2008-11)-RD-B-10 and LEQSF (2011-13)-RD-B-08. I would also like to thank AMRI for providing travel funds for conference meetings.

Last but not least, I would like to thank almighty for giving me an opportunity and strength to carry out the dissertation work and finally making it a reality. I dedicate this achievement to my late father who is no more to see the outcome of his life teachings which made me what I am today.

Table of Contents

List of Figures	x
Abstract	xviii
Chapter 1 Introduction and Background	1
1.1 Photosensors	1
1.2 Nanostructured photosensors	6
1.2.1 Quantum dot (0D) and thin film (2D) photodetector.....	6
1.2.2 Nanowire (1D) photodetector	9
1.2.3 Piezo-phototronic photodetector.....	10
1.3 Nanostructured magneto sensors	12
1.4 Overview of this dissertation	13
References.....	15
Chapter 2 Theoretical Framework	22
2.1 Piezoelectric nanostructures.....	23
2.2 Coupling of piezoelectric and semiconducting properties.....	25
2.2.1 Piezotronic effect	27
2.2.2 Piezo-phototronic effect.....	32
2.3 Coupling of piezoelectric-semiconducting and magnetic properties.....	36
2.4 Conclusion	39
References.....	40
Chapter 3 CdSe/ZnTe core/shell nanowire array piezo-phototronic photodetector	43
3.1 Introduction.....	43
3.2 Experimental.....	45
3.2.1 CVD growth of CdSe nanowire array on mica.....	46
3.2.2 CdSe/ZnTe core/shell nanowire array by PLD.....	46
3.2.3 Materials characterization.....	48
3.2.4 Device fabrication and measurements	48
3.3 Results and Discussion	50
3.3.1 Structure characterization	50
3.3.2 CdSe/ZnTe Core/Shell Nanowire Array Photodetector.....	52
3.4 Working mechanism of piezo-phototronic photodetector	59
3.5 Conclusion	62

References.....	63
<u>Chapter 4 Piezo-phototronic photodetector based on fully wide band gap type-II core/shell nanowire array</u>	68
4.1 Introduction.....	68
4.2 Experimental.....	70
4.2.1 CVD growth of ZnO nanowire array on ITO/glass substrate	70
4.2.2 ZnO/ZnS core/shell nanowire array by PLD	71
4.2.3 Materials characterization.....	72
4.2.4 Device fabrication and measurements	72
4.3 Results and Discussion	75
4.3.1 Structure characterization	75
4.3.2 ZnO/ZnS core/shell nanowire array photodetector.....	76
4.4 Working principle of fully wide band gap type-II piezo-phototronic photodetector.....	85
4.5 Conclusions.....	89
References.....	90
<u>Chapter 5 3D ZnO nanowire based piezo-magneto-photo sensor</u>	97
5.1 Introduction.....	97
5.2 Experimental.....	99
5.2.1 Synthesis and Characterization	99
5.2.2 Device fabrication and measurements	99
5.3 Results and Discussion	100
5.3.1 Structure characterization	100
5.3.2 ZnO nanowire array piezo-magneto sensor	102
5.3.3 Working mechanism of piezo-magneto sensor.....	108
5.3.4 ZnO nanowire array piezo-magneto-photo sensor.....	111
5.3.5 Working mechanism of piezo-magneto-photo sensor	116
5.4 Conclusions.....	118
References.....	120
<u>Chapter 6 Conclusion and Perspective</u>	125
<u>Appendix: Copyright Permissions</u>	127
<u>VITA</u>	133

List of Figures

Figure 1.1 Optical absorption coefficient for some common photodetector semiconductors.

Figure 1.2 Schematics of Schottky junction formation between n-type semiconductor and metal where work function of metal $\Phi_m > \Phi_s$, (a) relative position of Fermi levels and band energies before metallurgical junction formation and (b) equilibrium band positions in dark after junction formation and electron transfer from semiconductor conduction band minima (CBM) to metal Fermi level has occurred. Due to increase in electron energies, the CBM and VBM moves downward creating an upward band bending near metal-semiconductor interface leading to formation of barrier restricting net flow of charge carriers across junction. The bottom picture represents the formation of mobile charge carrier free depletion region.

Figure 1.3 A metal n-type semiconductor (MS) metallurgical junction formation and its influence on relative alignment of conduction band minimum (CBM) and valence and maxima (VBM). (a) MS junction under reverse bias (d) under forward bias. The *I-V* curve in the center shows the two modes of electrical conduction where the MS diode is off resulting in no current in reverse bias and MS diode on resulting in high current under forward bias.

Figure 1.4 Schematics of charge separation mechanism, device structure and configurations of few nanostructured photodetectors, (a) Drift and diffusion of both electrons and holes are exploited in photodiodes. This spatial band diagram depicts the junction between a p-type (hole-rich, left side) and n-type (electron-rich, right side) semiconductor near equilibrium, (b) In a photoconductor, one type of carrier is trapped while the other circulates under the influence of an electric field (electrons are trapped in this depiction), (c) Bulk-heterojunction photodiodes made from a polymer–nanocrystal (NC) composite exploit charge separation across the interface between the polymer matrix and the nanoparticles, and rely on differences in work function between the top and bottom contacts, (d) photodiodes consist of a single phase of a quantum-dot thin film across which electrical contacts having different work functions. (e) lateral photoconductors employ coplanar electrodes coated with a continuous film of nanocrystals (f) The conductance of this lateral three-terminal photodetector can be modulated by electrical and/or optical fields (shown in red). The channel in this device is a carbon nanotube. The localized gates

V_1 , V_2 and the global back gate V_g achieve selective electrostatic doping along the SWNT. V_{SD} is the source-drain voltage.

Figure 1.5 Piezoelectric potential distribution in a ZnO nanowire under transverse and longitudinal deformation, (a) transversely bent piezoelectric nanowire, (b) c-axis grown nanowire under axial strain. The dimensions of the nanowire are $L= 600$ nm and $a= 25$ nm; the external force is $f_y = 80$ nN.

Figure 2.1 A schematics representing the non-centrosymmetry in (a) tetrahedral Zn^{2+} and O^{2-} ionic co-ordination under external stress, (b) resulting microscopic dipole in one such tetrahedral unit, (c) several such unit cell participation resulting into macroscopic polarization, and (d) COMSOL simulated pictorial representation of polarization with color code scheme and magnitude of piezo-potential.

Figure 2.2 Piezopotential created inside a nanostructure, as represented by the color code, is the fundamental physics for nanogenerator and piezotronics. (a) Nanogenerator is based on a process of piezopotential driven flow of electrons in the external load. (b) Piezotronics is about the devices fabricated using a process of piezopotential tuned/controlled charge carrier transport at the metal–semiconductor interface or p–n junction. Piezo-phototronics is about the devices fabricated using piezopotential to control charge carrier generation, separation, transport and recombination processes at the interface/junction.

Figure 2.3 A metal n-type semiconductor (MS) metallurgical junction formation and its influence on relative alignment of conduction band minimum (CBM) and valence and maxima (VBM). (a) before metallurgical contact of semiconductor to metal is made, (b) equilibrium contact position of Fermi levels and energy bands after junction formation and in the absence of external bias and illumination, (c) the same MS junction under reverse bias and illumination and (d) under forward bias and illumination. The I-V curve in the center shows the two modes of electrical conduction where the MS diode is off resulting in no current in reverse bias and MS diode on resulting in high current under forward bias.

Figure 2.4 Energy band diagram for illustrating the effects of laser excitation and piezoelectricity on a Schottky contacted metal–semiconductor interface, (a) Band diagram at a Schottky contact

after exciting by a laser that has a photon energy higher than the bandgap, which is equivalent to a reduction in the Schottky barrier height, (b) Band diagram at the Schottky contact after applying a strain in the semiconductor. The piezopotential created in the semiconductor has a polarity with the end in contacting with the metal being low.

Figure 2.5 Ideal metal–semiconductor Schottky contacts with the presence of piezoelectric charges at applied voltage $V=0$ (thermal equilibrium). (a) Space charges distribution; (b) electric field and (c) energy band diagram with the presence of piezoelectric charges. Dashed lines indicate electric field and energy band in the absence of piezoelectric charges, and the solid lines are for the cases when a piezopotential is present in the semiconductor.

Figure 2.6 Illustration of ideal metal–semiconductor–metal structures with the presence of piezo-charges and photon generated charges. (a) Space charge distribution and corresponding (b) energy band diagram in the presence of piezo charges and photo generated charges. Dashed lines stand for original barriers without strain nor photoexcitation. The solid line is the finally tuned band structure by the piezo-charges, with one end being lifted up and one side being lowered. (adapted with permission from reference¹)

Figure 3.1 Schematics of (a) CdSe nanowire array synthesis by CVD and (b) CdSe/ZnTe core/shell nanowire by PLD.

Figure 3.2 Schematics of the device configuration and measurement set-up, (a-c) Preparation of substrate for CdSe nanowire array growth, (d) Perpendicular CdSe nanowire array grown by CVD, (e) CdSe/ZnTe core/shell nanowire array achieved by pulsed laser ablation of ZnTe shell, (f) PMMA layer spin coating, (g) Device positioned on PVC board with illumination source underneath and connected to measurement system (inset is a cross sectional view of the assembled device).

Figure 3.3 (a) a photograph of a typical prototype device. The dashed white rectangle (3mm×5mm) represents the area in which CdSe/ZnTe core/shell nanowire is grown. A 100 nm Ag coated polyester grating as top electrode is positioned on top of core/shell nanowire array, (b) UV-Vis absorption profile of a muscovite mica substrate, mica/CdSe thin film and CdSe/ZnTe core/shell nanowire array. The results indicate that light absorption occurs predominately in the nanowire array.

Figure 3.4 Morphology and structural analysis of CdSe and CdSe/ZnTe core/shell nanowire arrays, (a) Low magnification SEM image of a CdSe nanowire array, (b) Low magnification SEM image of a CdSe/ZnTe core/shell nanowire array, (c) HRTEM image of a single CdSe/ZnTe core/shell nanowire and (d) a lateral energy dispersive (EDS) line scan across a CdSe/ZnTe core/shell nanowire that demonstrates characteristic core/shell elemental peaks.

Figure 3.5. (a) I - V measurements of a CdSe/ZnTe core/shell nanowire array device under blue (465 nm) light illumination at variable intensities, (b) Absolute current of the device with respect to intensity, (c) On-off response of the device at a bias of 1.8 V and under blue illumination, (d) Photon responsivity of the device relative to the intensity density of the blue (465 nm) excitation source and bias voltage of 1.8 V.

Figure 3.6 (a) I - V measurements of a CdSe/ZnTe core/shell nanowire array device under green (520 nm) illumination at variable intensities, (b) Absolute current of the device with respect to intensity, (c) On-off response of the device at a bias of 1.8 V and under a blue excitation source, (d) Photon responsivity of the device relative to intensity of a green excitation source.

Figure 3.7 (a) I - V measurements for a CdSe/ZnTe core/shell nanowire array device under UV (385 nm) illumination at variable intensities, (b) Absolute current of the device with respect to intensity, (c) On-off response of the device at 1.8 V of applied bias and under a blue excitation source, (d) Photon responsivity of the device relative to intensity of a UV excitation source.

Figure 3.8 (a) I - V characteristic of CdSe/ZnTe core/shell nanowire array device under blue, green and UV illumination, (b-d) A typical I - V for a CdSe/ZnTe core/shell array device under different compressive loads and blue, green and UV illumination, respectively, (e) Absolute current of the device relative to compressive load under blue, green and UV illumination, (f) Change in responsivity of the device subjected to load differences and constant illumination, where R_0 is the responsivity at zero load.

Figure 3.9 Cross sectional view of the piezo-potential distribution, (a) along the x-y plane (nanowire diameter), (b) along the x-z plane (longitudinal or growth axis - the color scale shows the potential distribution).

Figure 3.10 Schematic band alignment of the Ag/ZnTe/CdSe structure. a) At equilibrium. b) Under illumination only. c) Under simultaneous application of compressive load and illumination. d) Under a compressive load of more than 0.25 kgf.

Figure 4.1 Schematic illustration of the ZnO/ZnS core/shell nanowire photodetector fabrication process. (a) ZnO nanowire array on ITO substrate synthesized through chemical vapor deposition (CVD), (b) a ZnS shell layer was deposited by pulsed laser ablation, (c) a $\sim 2 \mu\text{m}$ PMMA layer was spin coated onto the ZnO/ZnS core/shell nanowire array, and (d) the finished device mounted on a measurement cell. To achieve nanowire compression, load is applied on top of silver coated polyester zigzag electrode (inset figure d).

Figure 4.2 (a) photograph of the ZnO/ZnS core/shell nanowire array device with dimensional details and (b) piezo effect of ZnO/ZnS core/shell nanowire array under variable loads.

Figure 4.3 Structural characterization of a ZnO/ZnS core/shell nanowire showing low magnification top view, FESEM images of (a) an as-grown, ZnO nanowire array and (b) a ZnO/ZnS core/shell nanowire array, (c) an HRTEM image of a single ZnO/ZnS core/shell nanowire, and (d) the corresponding energy dispersive spectroscopy (EDS) lateral line scan depicting elemental peaks characteristic to core/shell nanowire structure.

Figure 4.4 Electrical characterization of a ZnO/ZnS core/shell nanowire array device under UV illumination. (a) I - V measurements at different illumination densities, (b) Illumination density dependence of photo-current, (c) the device's on-off response, and (d) the variation in responsivity under several UV illumination densities.

Figure 4.5 Electrical characterization of a ZnO/ZnS core/shell nanowire array device under blue illumination. (a) I - V measurements at different illumination densities, (b) illumination density dependence of photo-current, (c) the on-off response of the device, and (d) variation in device responsivity with respect to blue illumination densities.

Figure 4.6 Electrical characterization of a ZnO/ZnS core/shell nanowire array device under green illumination. (a) I - V measurements at different illumination densities, (b) illumination density dependence of photo-current, (c) the on-off response of the device and (d) variation in device responsivity as a function of green illumination densities.

Figure 4.7 Room temperature PL for ZnO/ZnS core/shell nanowires collected with comparable laser power $\sim 145 \mu\text{W}$ under 532, 442, and 325 nm excitation, respectively. Spectra range from 1.3 eV to the edge of each laser's emission. ZnO produces green emission at 2.40 eV. Lower excitation energies produced broader type-II transition peaks. (Inset) Magnification of the type-II transition PL peaks. The dotted orange line marks the broad peak center at ~ 1.95 eV.

Figure 4.8 Electrical characterization of ZnO/ZnS core/shell nanowire array devices showing (a) the photocurrent response under dark, green, blue and UV excitation, (b-d) photocurrent response at a fixed illumination densities of 1.32 mW/cm^2 (UV), 3.0 mW/cm^2 (blue) and 3.2 mW/cm^2 (green), respectively, with variable compressive loads. (e) Photocurrent response with respect to compressive loads and (f) the (%) change in responsivity with compressive loads.

Figure 4.9 Equilibrium band position of an Ag/ZnS/ZnO interface (a) that demonstrates an abrupt, type-II band alignment at the ZnS/ZnO core/shell interface before the silver contact is made, (b) silver (Ag) contact with ZnS promotes Fermi level realignment that induces band bending (c) under illumination only, displaying direct band-to-band and an indirect type-II transition, and (d) under illumination with compressive strain together leading to a piezopotential-induced band bending. The core is wurtzite structured ZnO, and the shell is the zinc blend structured ZnS (in green color). Dotted line in figure (b) represents the initial position of the valence band maxima and the conduction band minima, whereas the solid lines represent the respective positions after band realignment and/or compression of a nanowire.

Figure 4.10 Simulated piezoelectric potential distribution in ZnO core of ZnO/ZnS core/shell nanowire under (a) uniaxial compression combined with bending, vertical color code scheme represents the piezo-potential distribution mapping with strain (b) uniaxial compression only and (c) bending only. This simulation neglects any piezo-potential contribution from the zinc-blend ZnS shell.

Figure 5.1 Schematic illustration of the ZnO nanowire array piezo-magneto-photo sensor fabrication process. (a) ZnO nanowire array on ITO substrate synthesized through chemical vapor deposition (CVD), (b) a $\sim 2 \mu\text{m}$ PMMA layer was spin coated onto the ZnO nanowire array, and (c) the finished device mounted on a measurement cell, and (d) to achieve nanowire bending, load is applied on top of silver coated polyester zigzag electrode.

Figure 5.2 Structural characterization of a ZnO nanowire array, showing (a) low and (b) high magnification tilted top view, FESEM images of as-grown, ZnO nanowire array, (c) low magnification TEM image of a single ZnO nanowire, and (d) HRTEM image and (inset) SAED pattern of ZnO nanowire depicting characteristic single crystal diffraction pattern.

Figure 5.3 Typical I - V characteristic of ZnO nanowire array based piezo-magneto sensor in dark under (a) compressional strain only and (b-f) under compressional strain combined with 600-3000 μ T of external magnetic field. A successive decrease in peak current is apparent with increasing magnetic field strength for any particular fixed strain amount.

Figure 5.4 Typical I - V characteristic of ZnO nanowire array based piezo-magneto sensor in dark under high magnetic field strength (a) for 10 gf compressional load, and (b) under 20 gf compressional load.

Figure 5.5 Typical I - V characteristic of ZnO nanowire array based piezo-magneto sensor in dark under fixed compressional loads of (a) 0gf, (b) 5gf, (c) 20 gf, (d) 50 gf, and (e) 100 gf with varying magnetic field strengths of 0-3000 μ T. In each measurement condition the decreasing trend in peak current (insets) with increasing magnetic field strength is preserved.

Figure 5.6 Summary of change in peak current in dark with (a) fixed strain and variable external magnetic field strength and (b) fixed external magnetic field strength with variable strain.

Figure 5.7 Working mechanism of ZnO nanowire array piezo-magneto sensor, where (a) represents the energy band diagram of Ag-ZnO before metallurgical contact is made, (b) after contact in equilibrium under external forward bias and in dark, (c) under compressional load generated polarization charge at inner surface of ZnO in proximity of Ag-ZnO interface, and (d) under influence of external magnetic field applied parallel to the Ag-ZnO interface and perpendicular to c-axis of ZnO nanowire growth. Direction of Lorentz force is displayed by \times for electrons and by \cdot for holes. Solid lines and circles represent static and dotted ones represent dynamic condition where band position are altered (dotted blue lines) and dotted circles (empty/filled) represents charge carrier flow direction with arrows.

Figure 5.8 Typical I - V characteristic of ZnO nanowire array based piezo-magneto-photo sensor under UV illumination density of 1.32 mW/cm² (a) compressional strain only and (b-f) under

compressional strain combined with 600-3000 μT of external magnetic field. A gradual increase in peak current is apparent with increasing magnetic field strength under steady UV illumination density.

Figure 5.9 *I-V* measurements of ZnO nanowire array piezo-magneto-photo sensor in (a) dark and under UV illumination density of 1.32 mW/cm^2 (b) steady state UV illumination density of 1.32 mW/cm^2 combined with varying magnetic field strengths of 600 to 3000 μT , and (c-f) in presence of steady state UV illumination and fixed loads of 5, 20, 50 and 100 gf with variable magnetic field strength of 600 to 3000 μT , respectively in each load condition. Insets represents the enlarged view of the changes in peak current.

Figure 5.10 Summary of change in peak current under UV illumination density of 1.32 mW/cm^2 with (a) fixed strain and variable external magnetic field strength and (b) fixed external magnetic field strength with variable strain.

Figure 5.11 Working mechanism of ZnO nanowire array piezo-photo-magneto sensor, where (a) under compressional load generated polarization charge at inner surface of ZnO in proximity of Ag-ZnO interface in presence of magnetic field applied parallel to the interface and perpendicular to c-axis of ZnO nanowire growth, bottom nanowire drawing represents the trapping of free electrons by desorbed Oxygen molecule and (b) in presence of magnetic field, strain and UV illumination., bottom nanowire drawing represents hole trapping by surface states releasing Oxygen molecule and increasing the conductance. Direction of Lorentz force is displayed by \times for electrons and by \cdot for holes. Solid lines and circles represent static and dotted ones represent dynamic condition where band position are altered (dotted blue lines) and dotted circles (empty/filled) represents charge carrier flow direction.

Abstract

Piezotronic and piezo-phototronic is a burgeoning field of study which emerges from the coupling of intrinsic materials properties exhibited by non-centrosymmetric semiconductors. In the past decade research efforts were mainly focused on the wurtzite family of 1D nanostructures, with major emphasis on ZnO nanowire nanogenerators, MS piezotronic transistors, LEDs and photodetectors mainly integrated on single nanowires. In view of previously known advantages of charge carrier separation in radial heterojunctions, particularly in type-II core/shell nanowires, it can be anticipated that the performance of photosensing devices can be largely enhanced by piezo-phototronic effect. Moreover, the performance metrics can be further improved in an array of nanowires where geometrical feature enabled multiple reflection can efficiently trap incident illumination. The crux of this dissertation lies in the development of 3D type-II core/shell nanowire array based piezo-phototronic device and also to investigate the effect of magnetic field on ZnO nanowire arrays based piezotronic and piezo-phototronic device for new class of sensors.

In this regard, prototype piezo-phototronic broadband photodetectors integrated on two material systems, namely type-II CdSe/ZnTe 3D core/shell nanowire arrays and fully wide band gap type-II ZnO/ZnS 3D core/shell nanowire arrays have been developed where the photodetection performance of each device exhibits high sensitivity, fast response and large responsivity. The application of piezo-phototronic effect further improves the device performance by three to four orders of magnitude change numerically calculated from absolute responsivities at multiple wavelengths.

A 3D ZnO nanowire array based new class of piezo-photo-magnetotronic sensor is also developed for detection of pressure, illumination and magnetic field suggesting multiple functionality of a

single device where more than one effect can be coupled together to exhibit piezo-magnetotronic or piezo-photo-magnetotronic type of device behavior.

Keywords: 3D Photodetector, Piezoelectric, Piezotronic, Piezo-phototronic, Magnetic field, Piezo-magnetotronic, Piezo-photo-magnetotronic.

Chapter 1 Introduction and Background

1.1 Photosensors

Photosensor, which is a member of optoelectronic device family, is a generic name for two distinct device types, namely photodetectors and photovoltaics. In a photodetector, resistance (conductivity) changes in the presence of light whereas photovoltaic device produces a current or voltage as its output under light.¹ Photodetectors are important in data transmission over optical fibers by demodulation of optical variations into electrical variations which is amplified and processed for information transfer in addition to other common applications found in relay switches and security systems. The device function involves the interaction of photon with semiconductor *via* three basic processes: 1) electron-hole pair generation by incident photon, 2) charge carrier transport, and 3) extraction of charge carriers for signal generation.³ The photodetectors must also satisfy certain requirements as high sensitivity at operating wavelengths and high response speed with minimum noise in addition to physical requirements such as compact size, low biasing voltage need and reliable under operating conditions.⁵ There are two classes of photodetectors, namely thermal detectors which detect light by sensing the temperature rise and photon detectors. The discussion of this work will be mainly focused on the semiconductor photon detectors only which detect photons via quantum photoelectric effect through the photocurrent contribution from photo excited charge carriers. As a pre-requisite for photons of a particular wavelength to be absorbed in semiconductor materials the following relationship is obvious

$$\lambda = \frac{hc}{\Delta E} = \frac{1.24}{\Delta E(eV)} \quad (\mu m) \quad \mathbf{1.1}$$

here, λ is photon wavelength, h is Plank's constant, c is speed of light and ΔE is the gap between energy levels. Here λ represents the minimum wavelength detection limit and $h\nu > \Delta E$ can also cause photoexcitation. Usually ΔE corresponds to the band gap energy of semiconductors but it can also be barrier height as in metal-semiconductor photodetector or transition energy between the impurity level and band edge as in extrinsic photoconductor depending on the type of photodetector for which the type of material and wavelength of detection are optimized. In general, the amount of light absorption, that determines the quantum efficiency of the photodetector, is indicated by absorption coefficient which can be high for highly absorbing materials where absorption mainly occurs near the surface. Low absorption coefficient value indicates that light penetrates deeper into the materials and at extreme side the material can also be transparent for incident wavelength causing no photoexcitation. Figure 1.1 represents the optical absorption profile of some of the common semiconductor photodetectors.

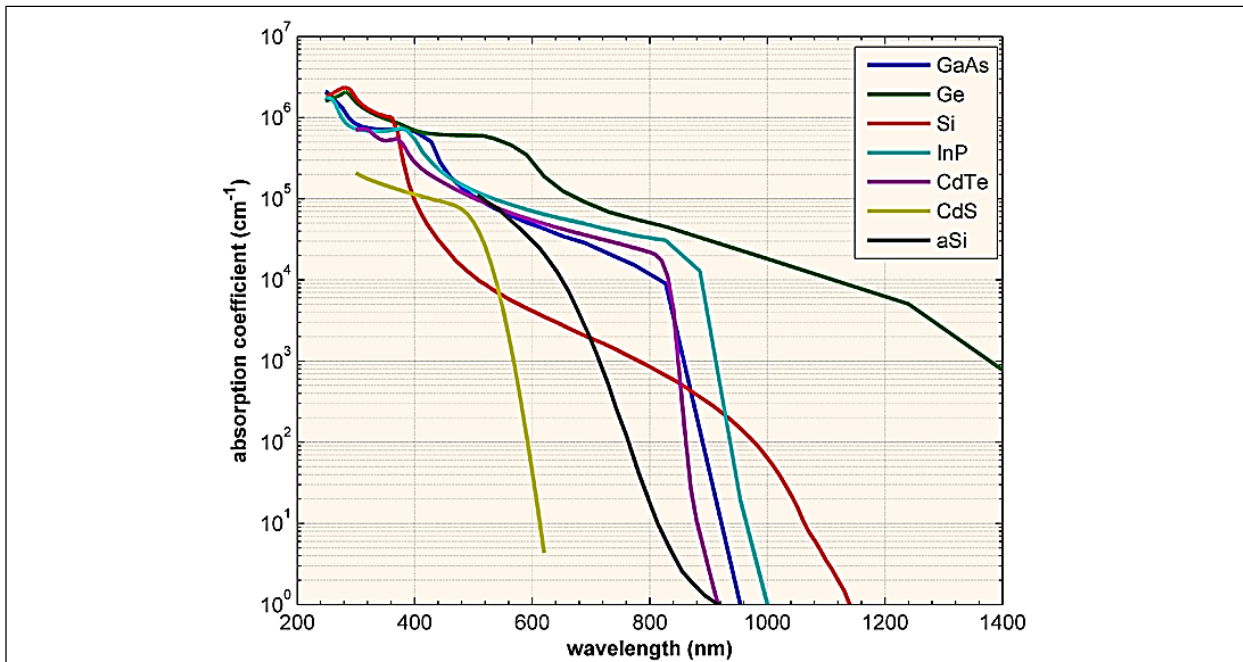


Figure 1. 1 Optical absorption coefficient for some common photodetector semiconductors.

© PV Education

It is apparent from Figure 1.1 that the optical absorption coefficient is highly dependent on wavelength of the photon and is usually non-uniform with maximum absorption taking place at band gap edge. The signal of the photocurrent should be maximized for the sensitivity for which the basic metric is quantum efficiency defined as the number of carriers produced per photon:

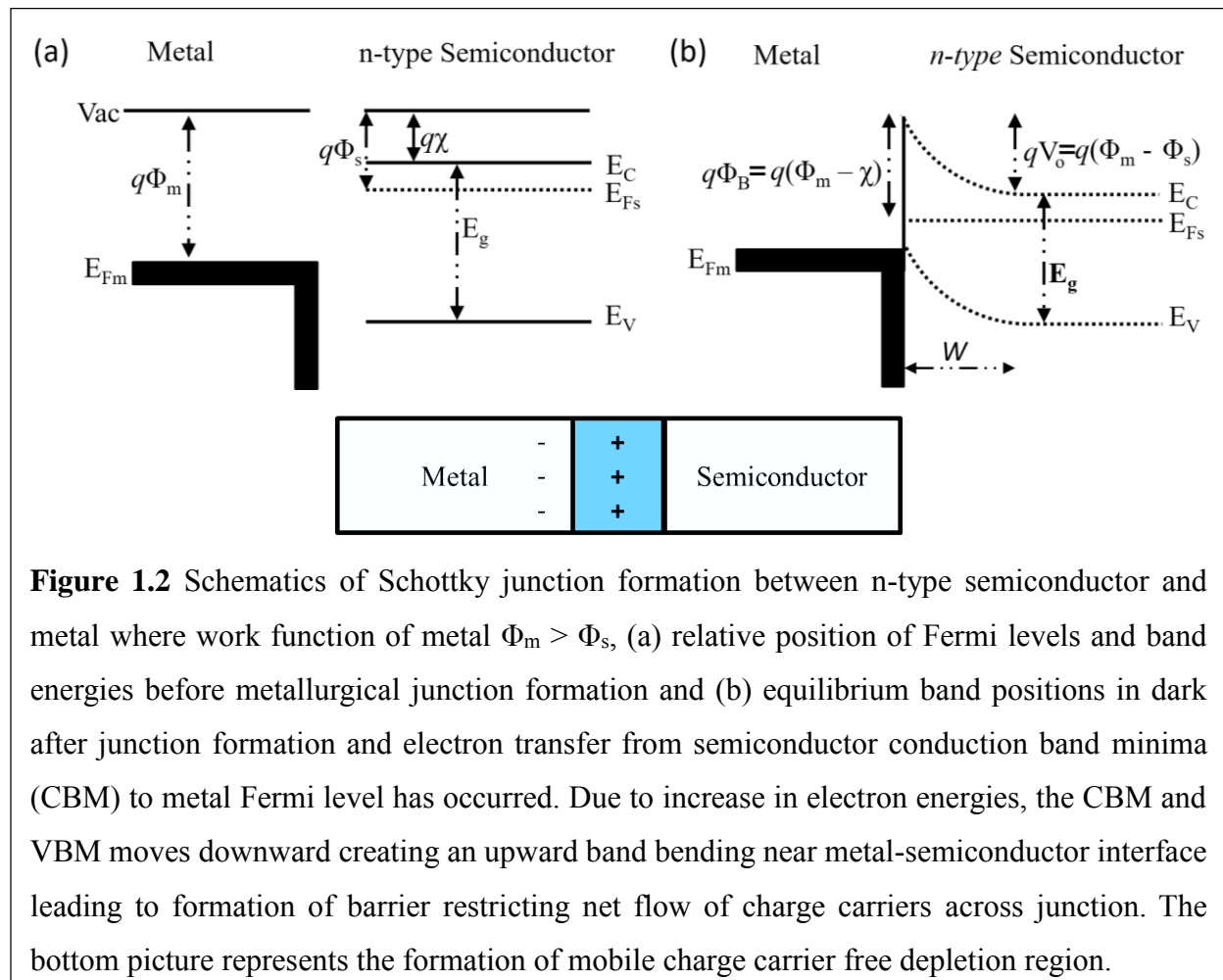
$$\eta = \frac{I_{ph}}{q\phi} = \frac{I_{ph}}{q} \left(\frac{hv}{P_{opt}} \right) \quad 1.2$$

where, I_{ph} is the photocurrent, ϕ is the photon flux, h is Plank's constant, ν is frequency of photon and P_{opt} is optical power.⁵ It can be seen in equation 1.1 that quantum efficiency η is a function of wavelength principally because absorption coefficient α is dependent on wavelength. The ideal quantum efficiency is unity however the losses occur either because of reflection, incomplete absorption or recombination leading to reduced photocurrent. Another metric to photodetectors is responsivity, described as

$$R_\lambda = \frac{I_{ph}}{P_{opt}} = \frac{\eta q}{hv} = \frac{\eta \lambda (\mu m)}{1.24} \text{ A/W} \quad 1.3$$

The responsivity (R_λ) relates the electric current flowing in the device to the incident optical power, ideally if every photon generates a single photoelectron a photon flux ϕ would produce an electron flux ϕ corresponding to a short circuit current $I_{ph} = e \phi$. From equation 1.3 it can be seen that R_λ increases with wavelength because photoelectric detectors are responsive to photon flux rather than optical power. As wavelength increases, a given optical power is carried by more electrons which in turn produces more electrons.⁶ These basic formulations applies equally well to photoconductors which is a slab of semiconductor with Ohmic metal contacts, photodiodes which works on the principle of depletion approximation formed between p - n junction and Schottky barrier diodes where p (or n) semiconductor is replaced by a thin metal film which forms Schottky

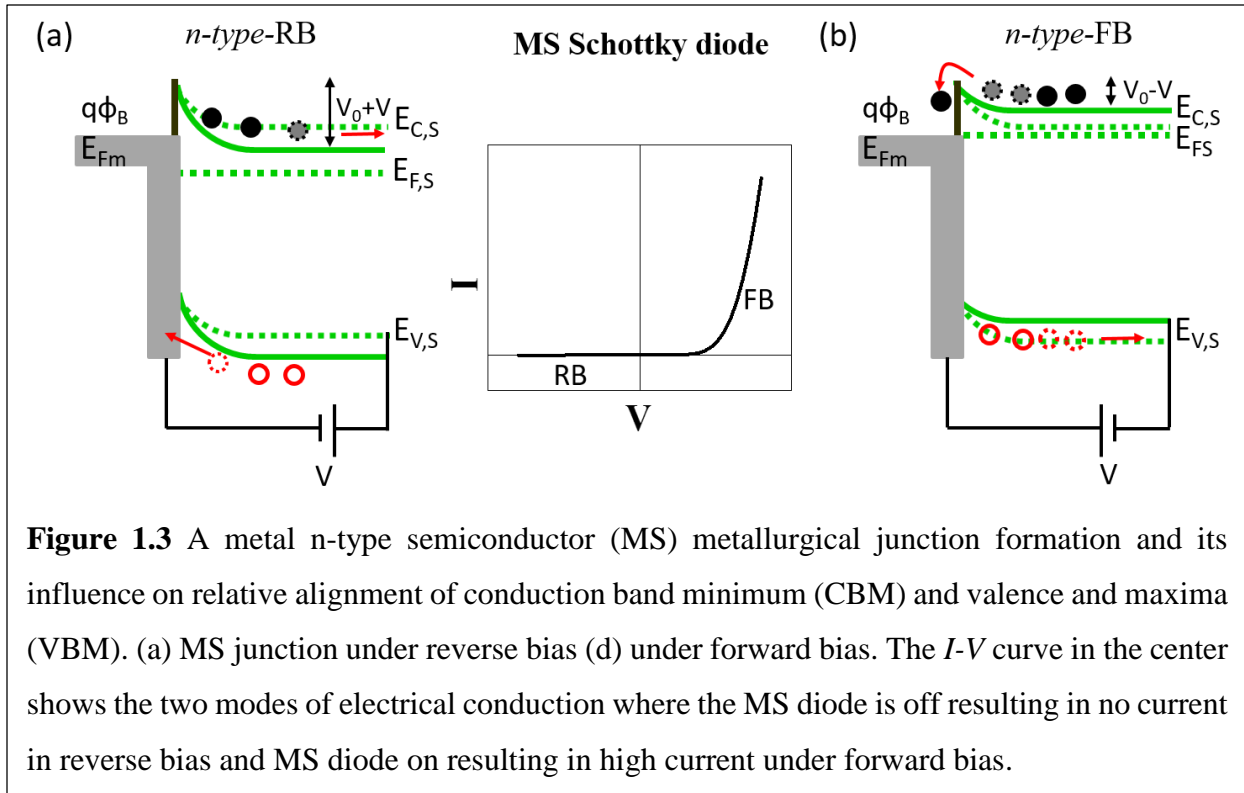
contact with the type of semiconductor. The present work is mainly focused on the Schottky contact devices hence any further discussion will be limited to Schottky barrier diodes. In order to understand the behavior of these devices it is imperative to have the idea about the junction formation. In particular, considering the case of *n-type* semiconductor with work function Φ_s smaller than the metal work function Φ_m (Figure 1.2 (a)) net electron transfer occurs between conduction band of semiconductor to metal side to realign the Fermi levels. As the process continues the electrostatic potential of semiconductor is raised in other words electron energy is lowered to achieve the equilibrium. Once equilibrium is established, no net charge transfer occurs across the interface and CBM and VBM bends upwards near the interface region.



The migration of electrons from semiconductor leaves behind the uncompensated donor ions creating a mobile charge free depletion region with equal and opposite polarity of charge layer formed due to accumulation of electrons at metal side. The equilibrium contact potential V_0 is the difference between the metal and semiconductor work function $\Phi_m - \Phi_s$ which prevents net flow of charge carriers across junction. The barrier for electron injection from metal to semiconductor side is $\Phi_m - \chi$, where $q\chi$ is the electron affinity measured from vacuum level to semiconductor conduction band edge. The equilibrium potential difference V_0 can be tuned by application of external bias or by inner piezopotential generated in wurtzite semiconductor under strain.⁷ When reverse bias voltage V is applied to the Schottky barrier, the barrier height is raised to V_0+V , the electron flow from semiconductor to metal becomes negligible (Figure 1.3 (a)) whereas a forward bias (Figure 1.3 (b)) reduces the barrier height for electron diffusion from semiconductor to metal side by $V_0 - V$ giving rise to forward current. In either case flow of electrons from metal to semiconductor is retarded by barrier height $\Phi_m - \chi$, the diode equation for this case can be described as:

$$I = I_0 \left(e^{\frac{qV}{kT}} - 1 \right) \quad 1.4$$

Above description of *n-type* semiconductor-metal Schottky barrier can also be used to describe the Schottky barrier formation for *p-type* semiconductor-metal junction with similar description of forwards and reverse bias and equation 1.4 can be used to describe the current. In both the cases the Schottky barrier is rectifying with higher current flowing in forwards direction and negligible current flowing in reverse direction and that in each case the forward current is due to injection of *majority carriers* from the semiconductor into the metal, therefore these devices are majority carrier devices.



1.2 Nanostructured photosensors

1.2.1 Quantum dot (0D) and thin film (2D) photodetector

Nanostructured materials are attractive for photodetection application because of their high surface to volume ratio and also providing an opportunity of device miniaturization in addition to other advantages arising from reduced dimensionality. In particular, nanostructures such as quantum dots⁸ and nanoparticles⁹ exhibit phenomena such as absorption of ultraviolet light, plasmonic enhancement of absorption,¹⁰ size-based spectral tuning, multiexciton generation, and charge carrier storage in surface and interface traps and can be integrated with conventional silicon electronics¹¹ and large area flexible substrates.¹² Figure 1.4 represents a schematics of few configurations of nanostructured photodetectors relying on photodiode (Figure 1.4 (a)) and photoconductor (Figure 1.4 (b)) mechanism of detection.

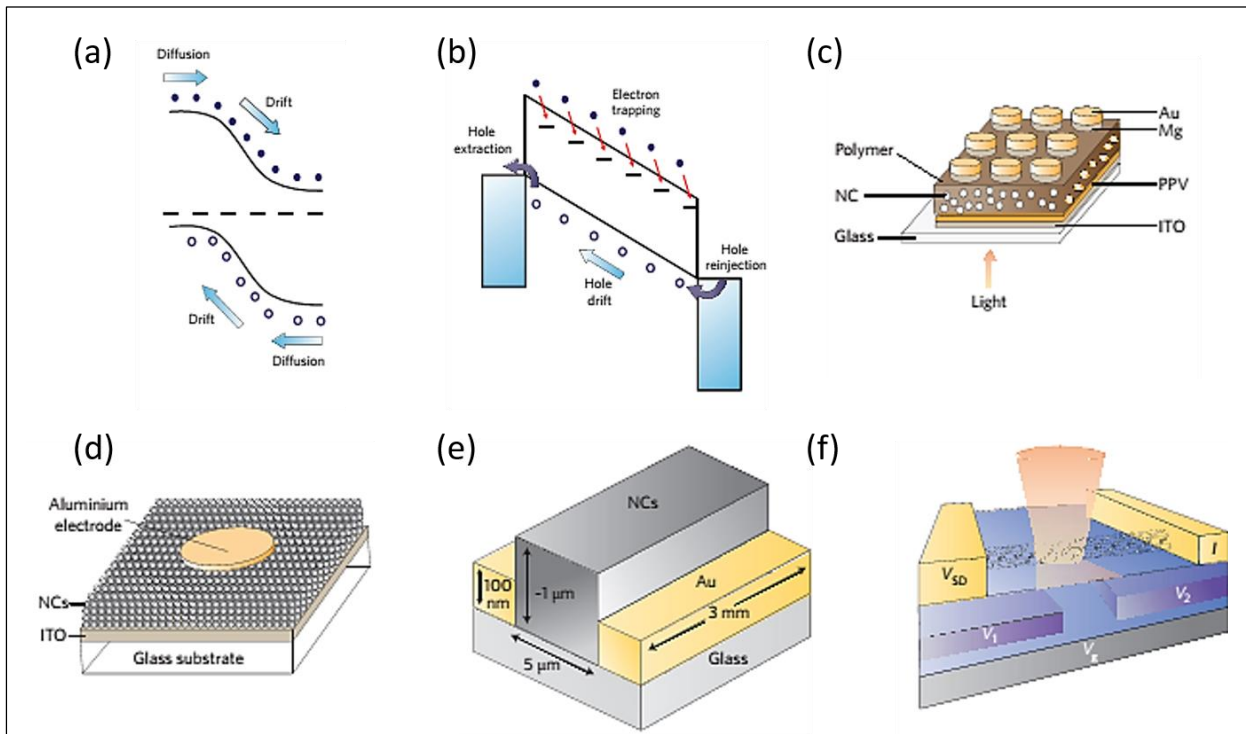


Figure 1.4 Schematics of charge separation mechanism, device structure and configurations of few nanostructured photodetectors, (a) Drift and diffusion of both electrons and holes are exploited in photodiodes. This spatial band diagram depicts the junction between a p-type (hole-rich, left side) and n-type (electron-rich, right side) semiconductor near equilibrium, (b) In a photoconductor, one type of carrier is trapped while the other circulates under the influence of an electric field (electrons are trapped in this depiction), (c) Bulk-heterojunction photodiodes made from a polymer–nanocrystal (NC) composite exploit charge separation across the interface between the polymer matrix and the nanoparticles, and rely on differences in work function between the top and bottom contacts, (d) photodiodes consist of a single phase of a quantum-dot thin film across which electrical contacts having different work functions. (e) lateral photoconductors employ coplanar electrodes coated with a continuous film of nanocrystals (f) The conductance of this lateral three-terminal photodetector can be modulated by electrical and/or optical fields (shown in red). The channel in this device is a carbon nanotube. The localized gates V_1 , V_2 and the global back gate V_g achieve selective electrostatic doping along the SWNT. V_{SD} is the source-drain voltage. (Reproduced with permission, © 2010 NPG)⁴

As seen in Figure 1.4 (a), a photodiode utilizes both types of photo excited charge carriers, namely electrons and holes contribution towards current leading to a quantum efficiency of unity. In order to increase the quantum efficiency of photodiodes alternative mechanism such as avalanche or carrier multiplication may be employed. However, photodiodes can have fast response times which is only limited by electron-hole recombination time that is of the order of microseconds or less making these devices useful for high speed application as required in fiber optical communication where more than 40 Gb/sec or higher data transmission rates are desirable. Figure 1.4 (b) illustrates a photoconductor which works on the principle of utilizing only one type of charge carrier either electrons as in *n-type* semiconductor or holes as in *p-type* semiconductor whereas keeping the other carrier type trapped in near surface defect states or in the bulk of the semiconductor thereby significantly reducing the recombination rate and prolonged carrier lifetime before it can finally recombine with its counterpart.⁴ These device types usually are characterized by high responsivity values ranging from 100-1000 AW⁻¹ though the tradeoff is reduced bandwidth. Figure 1.4 (c) shows a nano crystals embedded polymer thin film photodetector whereas¹³ Figure 1.4 (d) is a thin film of colloidal quantum dots deposited on a conducting ITO substrate by spin coating where an organic material was employed to provide the phase for carrier transport and quantum dots having type-II band alignment with polymer provided the sensitization.^{14,15} The thin film analogue of photodetector (Figure 1.4 (e)) was also fabricated by solution casting of nanocrystal between patterned gold electrodes to achieve superior photodetection compared to its epitaxial counterpart.¹⁶ In a quest to achieve high gain photodetectors where each incident photon can produce multiple electron-hole pairs electrostatically doped split gate field effect transistor device integrated on single walled carbon nanotube (Figure 1.4 (f)) was reported which was truly a one dimensional photodetector and

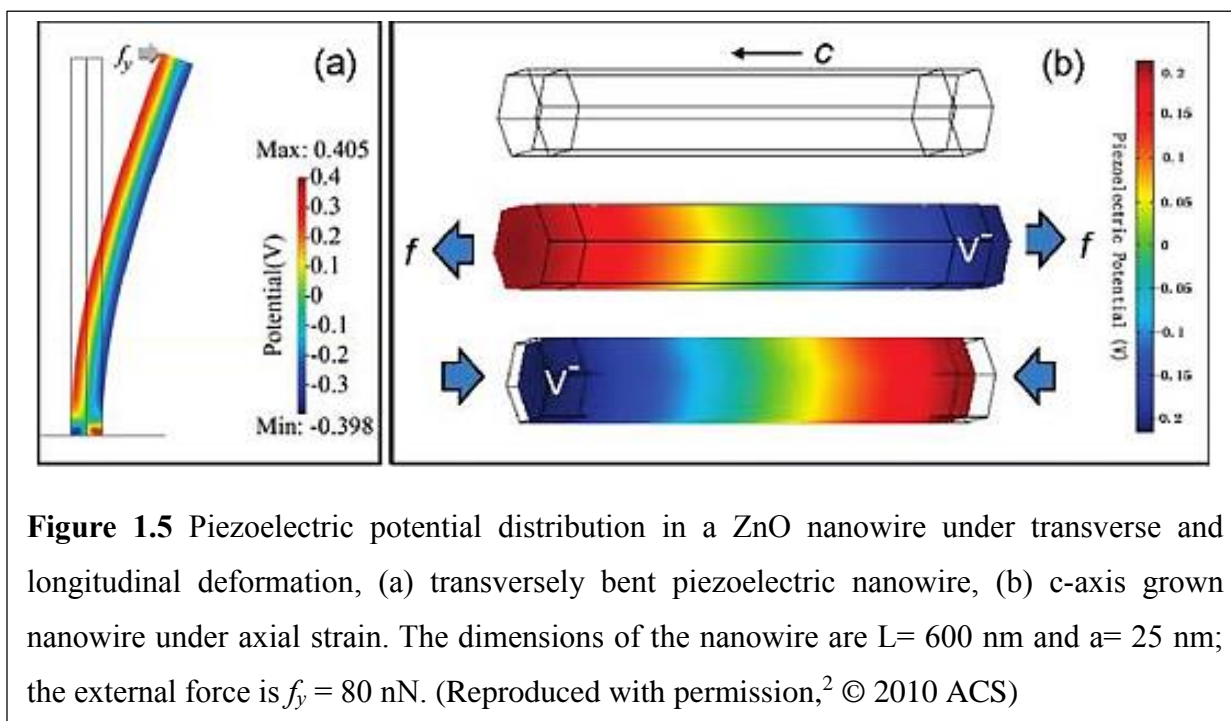
indicated the potential for nanowire based photodetectors can be advantageous for photodetection in near-infrared and visible and UV part of the spectrum.¹⁷⁻¹⁹

1.2.2 Nanowire (1D) photodetector

One dimensional nanostructures such as nanowire, nanorod, nanopillar and nanotubes have unique optical, mechanical, electrical and thermal properties which can be advantageous for photodetection applications.²⁰ The construction and integration of photodetectors or optical switches based on such nanostructures with tailored geometries have rapidly advanced in recent years.^{21,22} Especially, two main factors contributing to the high photosensitivity of such nanostructures should be recognized: 1) the large surface-to-volume ratio and the presence of deep level surface trap states in NWs greatly prolongs the photocarrier lifetime; 2) the reduced dimensionality of the active area in NW devices shortens the carrier transit time. Indeed, the combination of long lifetime and short transit time of charge carriers can result in substantial photoconductive gain.²³⁻²⁵ This nano-macro interface is fundamental to the integration of nanoscale building blocks in electrical or optoelectronic device applications.^{26,27} Of particular importance are earth abundant metal oxide nanowires^{28,29} such as ZnO,³⁰ SnO₂,³¹ Cu₂O,³² In₂O₃³³ and other binary semiconductors³⁴ such as CdSe,³⁵ GaN,³⁶ CdS³⁷ owing to their excellent optical and electrical properties which in form of nanowire provides unidirectional charge carrier transport. However, due to relatively easier synthesis and versatility to grow various shapes and morphology on practically any substrate, ZnO has gained tremendous attention of research for optoelectronic device development.^{38,39} In particular, owing to its wide band gap (3.2 eV) ZnO nanowire have found application in UV-visible blind photodetection with large photoresponse under low illumination intensities of $\sim 10 \mu\text{m}/\text{cm}^2$ translating to a photoconductive gain of $G > 10^8$ which was attributed to enhanced carrier lifetime through high density of surface trap states.²³

1.2.3 Piezo-phototronic photodetector

In view of intrinsic piezoelectric property arising from non-centrosymmetric⁴⁰ wurtzite crystal structure, the nanowire based device application of ZnO,⁴¹ GaN,^{42,43} CdS⁴⁴ and CdSe⁴⁵ etc. can be further tuned by application of external stress which results in piezo polarization charges under elastic deformation limits. The coupling of piezoelectric, semiconducting, electrical and optical properties can effectively tune/control the charge carrier generation, recombination, transport and/or separation across an interface/junction and is known as piezotronic/piezo-phototronic effect, a word coined in 2010 by Z. L. Wang group.²⁻⁴⁶ Figure 1.5 represents two basic modes of elastic deformation mechanism where Figure 1.5 (a) represents transverse bending with one end of nanowire fixed to the substrate and Figure 1.5 (b) is uniaxial compression/tensile mode of elastic deformation. It can be seen in Figure 1.5 (a) that the piezopotential distribution is radially asymmetric whereas it is axially asymmetric in case of compressional/tensile deformation in Figure 1.5 (b). The origin and asymmetry in piezopotential distribution is fundamental building block of piezotronic and piezo-phototronic effect.



The concept of piezo-phototronic effect has been successfully applied to enhance the device performance of many photodetectors based on one dimensional nanostructures.⁴⁷ For instance, the sensitivity of a single ZnO micro-/nanowire based UV photodetector was increased by more than 500% under nominal (-0.36%) compressional strain⁴⁸ and also in single CdSe nanowire based photodetector where the sensitivity of photodetection was found to highly depend on the applied strain.⁴⁹ However, the spatial confinement of charge carrier in a single conducting channel is disadvantageous for device performance due to increased recombination probability. To overcome this drawback, alternative approach of separating electron-hole pairs in different conducting channels is critical to inhibit recombination and increased device performance. In this regard, type-II core/shell nanowire heterostructure in which electrons and holes are separated and confined in spatially different conducting channels is considered as a viable approach.⁵⁰⁻⁵⁴ Based on this principle, a single ZnO/CdS core/shell micro-/nanowire piezo-phototronic photodetector was realized where the performance of the photodetector was enhanced by more than 10 time by application of piezo-phototronic effect.⁵⁵ These findings are intuitive and can also be applied to array of piezoelectric nanowires which exhibit excellent electrical properties due to multichannel charge transport *via* parallel connected nanowires in an array⁵⁶⁻⁵⁸ and also exhibit enhanced photo absorption due to geometrical features which enables multiple reflection and trapping of incident illumination.^{59,60} These features of three dimensional core/shell nanowire arrays have been successfully employed in realizing the UV/visible photodetector based on carbon fiber/ZnO/CdS double shell microwire⁶¹ and recently, in optical-fiber-nanowire hybrid structure⁶² suggesting that three dimensional core/shell nanowire arrays are a very promising candidate for piezo-phototronic device applications.

1.3 Nanostructured magneto sensors

The effect of external magnetic field in certain specific configurations such as the relative direction of current flowing through a conductor (semiconductor) and the direction of external magnetic field are of particular importance in view of Hall effect, which has strong effect in semiconductors and magnetoresistance, which is usually extremely small for many substances even under strong magnetic fields and is significant only in strong magnetic materials.⁶³ On semiconductors application of external magnetic field results in two distinct effects namely Hall effect and carrier deflection leading to magnetoconcentration assuming that the field has linear effects only.⁶⁴ Especially for semiconductor materials, in particular for InSb bilayer *p-n* channel external magnetic application has resulted in controlling the carrier generation and recombination rate.^{65,66} Strong magnetic field measurements performed on Si revealed high magnetoresistance^{67,68} and similar measurements on HgCdTe diode has resulted in observation magnetoconductance.⁶⁶ The basic physics of Lorentz force induced carrier deflection was also applied to investigate the effect of external magnetic field on a Germanium *p-n* junction photovoltaic device⁶⁹ and recently in developing a prototype magnetic field reconfigurable Boolean logic device based integrated on planar InSb *p-n* junction.⁷⁰ From these findings of magnetic field effect on semiconductors it is apparent that nanostructured semiconductors are also, in principle, prone to exhibit some of these characteristics such as magnetoresistance and magnetoconcentration which can modify the conductance leading to alter the device performance. In view of reduced dimensionality interesting effects can be anticipated to be observed which may pave way for new type of sensorics which may combine piezoelectric, semiconducting and optical/electrical properties of nonmagnetic semiconductors, however so far the scientific literature in this area is scarce.⁷¹

1.4 Overview of this dissertation

The thesis will mainly be divided in two sections based on slightly different but intricately connected theme of study. The first part, which includes Chapters 3 and 4, of the work presented in this thesis will demonstrates the novelty of piezo-phototronic devices based on nearly lattice matched or abruptly interfaced three dimensional type-II core/shell nanowire arrays. In second part, which is Chapter 5, effect of external magnetic field on piezotronic and piezo-phototronic effect will be investigated and findings will be discussed. Here follows a short abstract for each chapter.

Chapter 2 will describe the theoretical formulation of piezotronic, piezo-phototronic and piezo-magneto-phototronic effect which arises from the coupling of intrinsic semiconducting and piezoelectric property exhibited in non-centrosymmetric wurtzite semiconductor crystal. The investigation of external magnetic field effect of the performance of piezotronic and piezo-phototronic device reveals that deflection of charge carriers through Lorentz force plays a dominant role in modifying the conductance of nanowires in presence of surface defects.

In **Chapter 3**, a broad-band photodetector based on II-VI binary CdSe/ZnTe core/shell nanowire arrays will be demonstrated, where enhanced photo-detection by the piezo-phototronic effect will be discussed in detail. The photodetector performance under UV (385 nm), blue (465 nm) and green (520 nm) illumination infers a saturation free response with an intensity variation near two orders of magnitude that resulted a (%) responsivity change by four orders of magnitude. The significant increase in responsivity was attributed to: (1) the piezo-phototronic effect induced by a change in the Schottky barrier height at the Ag-ZnTe junction, and in the type-II band alignment at the CdSe-ZnTe interfaces, in conjugation with (2) a small lattice mismatch between the CdSe and ZnTe epitaxial layers, which lead to reduced charge carrier recombination.

In **Chapter 4**, a high-performance broad band UV/Visible photodetector fabricated on a fully wide bandgap ZnO/ZnS type-II heterojunction core/shell nanowire array will be discussed. The device can detect photons with energies significantly smaller (2.2 eV) than the band gap of ZnO (3.2eV) and ZnS (3.7 eV) which is mainly attributed to spatially indirect type-II transition facilitated by the abrupt interface between the ZnO core and ZnS shell. The performance of the device was further enhanced through the piezo-phototronic effect induced lowering of the barrier height to allow charge carrier transport across the ZnO/ZnS interface, resulting in three orders of relative responsivity change measured at three different excitation wavelengths (385 nm, 465 nm and 520 nm).

Chapter 5 will present the findings of the external magnetic field effect on ZnO nanowire array based piezotronic and piezo-phototronic device. The experimental observation of external magnetic field effect under compressional strain and optical illumination exhibits coupling of aforementioned three stimuli, where they act synergistically to alter the device performance. This is the first work of its kind whose findings anticipates novel sensorics applications and multiple functionalities in a single device.

References

1. S. M. Sze, S. M. S., Kwok K. Ng, *Physics of semiconductor devices*. John Wiley & Sons, Inc.: 2007.
2. Wang, Z. L., Piezotronic and Piezophototronic Effects. *The Journal of Physical Chemistry Letters* **2010**, *1* (9), 1388-1393.
3. Ben G. Streetman; Banerjee, S., *Solid State Electronic Devices*. 7 ed.; Pearson Education, Limited: 2005.
4. Konstantatos, G.; Sargent, E. H., Nanostructured materials for photon detection. *Nat Nano* **2010**, *5* (6), 391-400.
5. Simon M. Sze, K. K. N., *Physics of Semiconductor Devices, 3rd Edition*. 3 ed.; Wiley: 2006; p 832 pages.
6. Saleh, B. E. A.; Teich, M. C., *Fundamentals of Photonics*. Wiley: 2007.
7. Wang, Z. L., *Piezotronics and Piezo-Phototronics*. Springer: 2013; p 248.
8. Murray, C. B.; Norris, D. J.; Bawendi, M. G., Synthesis and characterization of nearly monodisperse CdE (E = sulfur, selenium, tellurium) semiconductor nanocrystallites. *Journal of the American Chemical Society* **1993**, *115* (19), 8706-8715.
9. Sun, Y.; Xia, Y., Shape-Controlled Synthesis of Gold and Silver Nanoparticles. *Science* **2002**, *298* (5601), 2176-2179.
10. Kelly, K. L.; Coronado, E.; Zhao, L. L.; Schatz, G. C., The Optical Properties of Metal Nanoparticles: The Influence of Size, Shape, and Dielectric Environment. *The Journal of Physical Chemistry B* **2003**, *107* (3), 668-677.
11. Kanno, T.; Saga, M.; Matsumoto, S.; Uchida, M.; Tsukamoto, N.; Tanaka, A.; Itoh, S.; Nakazato, A.; Endoh, T.; Tohyama, S.; Yamamoto, Y.; Murashima, S.; Fujimoto, N.; Teranishi,

N. In *Uncooled infrared focal plane array having 128 x 128 thermopile detector elements*, 1994; pp 450-459.

12. Nausieda, I.; Ryu, K.; Kymissis, I.; Akinwande, A. I.; Bulovic, V.; Sodini, C. G., An Organic Active-Matrix Imager. *Electron Devices, IEEE Transactions on* **2008**, *55* (2), 527-532.

13. Clark, S. W.; Harbold, J. M.; Wise, F. W., Resonant Energy Transfer in PbS Quantum Dots. *The Journal of Physical Chemistry C* **2007**, *111* (20), 7302-7305.

14. Greenham, N. C.; Peng, X.; Alivisatos, A. P., Charge separation and transport in conjugated-polymer/semiconductor-nanocrystal composites studied by photoluminescence quenching and photoconductivity. *Physical Review B* **1996**, *54* (24), 17628-17637.

15. Greenham, N. C.; Peng, X.; Alivisatos, A. P., Charge separation and transport in conjugated polymer/cadmium selenide nanocrystal composites studied by photoluminescence quenching and photoconductivity. *Synthetic Metals* **1997**, *84* (1-3), 545-546.

16. Konstantatos, G.; Clifford, J.; Levina, L.; Sargent, E. H., Sensitive solution-processed visible-wavelength photodetectors. *Nat Photon* **2007**, *1* (9), 531-534.

17. Gabor, N. M.; Zhong, Z.; Bosnick, K.; Park, J.; McEuen, P. L., Extremely Efficient Multiple Electron-Hole Pair Generation in Carbon Nanotube Photodiodes. *Science* **2009**, *325* (5946), 1367-1371.

18. Lee, J. U.; Gipp, P. P.; Heller, C. M., Carbon nanotube p-n junction diodes. *Applied Physics Letters* **2004**, *85* (1), 145-147.

19. Hayden, O.; Agarwal, R.; Lieber, C. M., Nanoscale avalanche photodiodes for highly sensitive and spatially resolved photon detection. *Nat Mater* **2006**, *5* (5), 352-356.

20. Vj, L.; Oh, J.; Nayak, A. P.; Katzenmeyer, A. M.; Gilchrist, K. H.; Grego, S.; Kobayashi, N. P.; Shih-Yuan, W.; Talin, A. A.; Dhar, N. K.; Islam, M. S., A Perspective on Nanowire Photodetectors: Current Status, Future Challenges, and Opportunities. *Selected Topics in Quantum Electronics, IEEE Journal of* **2011**, *17* (4), 1002-1032.

21. Yang, P.; Yan, H.; Mao, S.; Russo, R.; Johnson, J.; Saykally, R.; Morris, N.; Pham, J.; He, R.; Choi, H. J., Controlled Growth of ZnO Nanowires and Their Optical Properties. *Advanced Functional Materials* **2002**, *12* (5), 323-331.
22. Lieber, C. M.; Wang, Z. L., Functional Nanowires. *MRS Bulletin* **2007**, *32* (02), 99-108.
23. Soci, C.; Zhang, A.; Xiang, B.; Dayeh, S. A.; Aplin, D. P. R.; Park, J.; Bao, X. Y.; Lo, Y. H.; Wang, D., ZnO Nanowire UV Photodetectors with High Internal Gain. *Nano Letters* **2007**, *7* (4), 1003-1009.
24. Grimmeiss, H. G., Photoelectronic properties of semiconductors. By Richard H. Bube, Cambridge University Press, Cambridge 1992, 318 pp., paperback, £ 17.95, ISBN 0-521-40681-1. *Advanced Materials* **1993**, *5* (1), 65-66.
25. McGlynn, S. P., Concepts in Photoconductivity and Allied Problems. *Journal of the American Chemical Society* **1964**, *86* (24), 5707-5707.
26. Lu, J. G.; Chang, P.; Fan, Z., Quasi-one-dimensional metal oxide materials—Synthesis, properties and applications. *Materials Science and Engineering: R: Reports* **2006**, *52* (1–3), 49-91.
27. Yan, R.; Gargas, D.; Yang, P., Nanowire photonics. *Nat Photon* **2009**, *3* (10), 569-576.
28. Zhai, T.; Fang, X.; Liao, M.; Xu, X.; Zeng, H.; Yoshio, B.; Golberg, D., A Comprehensive Review of One-Dimensional Metal-Oxide Nanostructure Photodetectors. *Sensors (Basel, Switzerland)* **2009**, *9* (8), 6504-6529.
29. Yu, J. S.; Ko, Y. H.; Nagaraju, G. In *Low-dimensional II-VI oxide-based semiconductor nanostructure photodetectors for light sensing*, 2015; pp 93702X-93702X-8.
30. Law, J. B. K.; Thong, J. T. L., Simple fabrication of a ZnO nanowire photodetector with a fast photoresponse time. *Applied Physics Letters* **2006**, *88* (13), 133114.
31. Lu, M.-L.; Weng, T.-M.; Chen, J.-Y.; Chen, Y.-F., Ultrahigh-gain single SnO₂ nanowire photodetectors made with ferromagnetic nickel electrodes. *NPG Asia Mater* **2012**, *4*, e26.

32. Jia, R.; Lin, G.; Zhao, D.; Zhang, Q.; Lin, X.; Gao, N.; Liu, D., Sandwich-structured Cu₂O photodetectors enhanced by localized surface plasmon resonances. *Applied Surface Science* **2015**, *332*, 340-345.
33. Zhang, D.; Li, C.; Han, S.; Liu, X.; Tang, T.; Jin, W.; Zhou, C., Ultraviolet photodetection properties of indium oxide nanowires. *Appl Phys A* **2003**, *77* (1), 163-166.
34. Xia, Y.; Yang, P.; Sun, Y.; Wu, Y.; Mayers, B.; Gates, B.; Yin, Y.; Kim, F.; Yan, H., One-Dimensional Nanostructures: Synthesis, Characterization, and Applications. *Advanced Materials* **2003**, *15* (5), 353-389.
35. Singh, A.; Li, X.; Protasenko, V.; Galantai, G.; Kuno, M.; Xing, H.; Jena, D., Polarization-Sensitive Nanowire Photodetectors Based on Solution-Synthesized CdSe Quantum-Wire Solids. *Nano Letters* **2007**, *7* (10), 2999-3006.
36. Wu, H.; Sun, Y.; Lin, D.; Zhang, R.; Zhang, C.; Pan, W., GaN Nanofibers based on Electrospinning: Facile Synthesis, Controlled Assembly, Precise Doping, and Application as High Performance UV Photodetector. *Advanced Materials* **2009**, *21* (2), 227-231.
37. Jie, J. S.; Zhang, W. J.; Jiang, Y.; Meng, X. M.; Li, Y. Q.; Lee, S. T., Photoconductive Characteristics of Single-Crystal CdS Nanoribbons. *Nano Letters* **2006**, *6* (9), 1887-1892.
38. Jagadish, C.; Pearson, S. J., *Zinc Oxide Bulk, Thin Films and Nanostructures: Processing, Properties, and Applications*. Elsevier Science: 2011.
39. Strzhemechny, Y., Recent Advances in the Design of Photodetectors Based on Thin-Film and Nanostructured ZnO. In *Nanoscale Sensors*, Li, S.; Wu, J.; Wang, Z. M.; Jiang, Y., Eds. Springer International Publishing: 2013; Vol. 19, pp 153-188.
40. Halasyamani, P. S.; Poepelmeier, K. R., Noncentrosymmetric Oxides. *Chemistry of Materials* **1998**, *10* (10), 2753-2769.
41. Wang, Z. L.; Song, J., Piezoelectric Nanogenerators Based on Zinc Oxide Nanowire Arrays. *Science* **2006**, *312* (5771), 242-246.

42. Huang, C.-T.; Song, J.; Lee, W.-F.; Ding, Y.; Gao, Z.; Hao, Y.; Chen, L.-J.; Wang, Z. L., GaN Nanowire Arrays for High-Output Nanogenerators. *Journal of the American Chemical Society* **2010**, *132* (13), 4766-4771.
43. Minary-Jolandan, M.; Bernal, R. A.; Kuljanishvili, I.; Parpoil, V.; Espinosa, H. D., Individual GaN Nanowires Exhibit Strong Piezoelectricity in 3D. *Nano Letters* **2011**, *12* (2), 970-976.
44. Lin, Y.-F.; Song, J.; Ding, Y.; Lu, S.-Y.; Wang, Z. L., Piezoelectric nanogenerator using CdS nanowires. *Applied Physics Letters* **2008**, *92* (2), -.
45. Zhou, Y. S.; Wang, K.; Han, W.; Rai, S. C.; Zhang, Y.; Ding, Y.; Pan, C.; Zhang, F.; Zhou, W.; Wang, Z. L., Vertically Aligned CdSe Nanowire Arrays for Energy Harvesting and Piezotronic Devices. *ACS Nano* **2012**, *6* (7), 6478-6482.
46. Zhang, Y.; Liu, Y.; Wang, Z. L., Fundamental Theory of Piezotronics. *Advanced Materials* **2011**, *23* (27), 3004-3013.
47. Wang, Z. L., Piezopotential gated nanowire devices: Piezotronics and piezo-phototronics. *Nano Today* **2010**, *5* (6), 540-552.
48. Yang, Q.; Guo, X.; Wang, W.; Zhang, Y.; Xu, S.; Lien, D. H.; Wang, Z. L., Enhancing Sensitivity of a Single ZnO Micro-/Nanowire Photodetector by Piezo-phototronic Effect. *ACS Nano* **2010**, *4* (10), 6285-6291.
49. Dong, L.; Niu, S.; Pan, C.; Yu, R.; Zhang, Y.; Wang, Z. L., Piezo-Phototronic Effect of CdSe Nanowires. *Advanced Materials* **2012**, *24* (40), 5470-5475.
50. Zhang, Y.; Lin-Wang; Mascarenhas, A., "Quantum Coaxial Cables" for Solar Energy Harvesting. *Nano Letters* **2007**, *7* (5), 1264-1269.
51. Wang, K.; Chen, J.; Zhou, W.; Zhang, Y.; Yan, Y.; Pern, J.; Mascarenhas, A., Direct Growth of Highly Mismatched Type II ZnO/ZnSe Core/Shell Nanowire Arrays on Transparent Conducting Oxide Substrates for Solar Cell Applications. *Advanced Materials* **2008**, *20* (17), 3248-3253.

52. Schrier, J.; Demchenko, D. O.; Wang; Alivisatos, A. P., Optical Properties of ZnO/ZnS and ZnO/ZnTe Heterostructures for Photovoltaic Applications. *Nano Letters* **2007**, *7* (8), 2377-2382.
53. Wang, K.; Chen, J. J.; Zeng, Z. M.; Tarr, J.; Zhou, W. L.; Zhang, Y.; Yan, Y. F.; Jiang, C. S.; Pern, J.; Mascarenhas, A., Synthesis and photovoltaic effect of vertically aligned ZnO/ZnS core/shell nanowire arrays. *Applied Physics Letters* **2010**, *96* (12), 123105.
54. Wang, K.; Rai, S. C.; Marmon, J.; Chen, J.; Yao, K.; Wozny, S.; Cao, B.; Yan, Y.; Zhang, Y.; Zhou, W., Nearly lattice matched all wurtzite CdSe/ZnTe type II core-shell nanowires with epitaxial interfaces for photovoltaics. *Nanoscale* **2014**, *6* (7), 3679-3685.
55. Zhang, F.; Ding, Y.; Zhang, Y.; Zhang, X.; Wang, Z. L., Piezo-phototronic Effect Enhanced Visible and Ultraviolet Photodetection Using a ZnO–CdS Core–Shell Micro/nanowire. *ACS Nano* **2012**, *6* (10), 9229-9236.
56. Mor, G. K.; Shankar, K.; Paulose, M.; Varghese, O. K.; Grimes, C. A., Use of Highly-Ordered TiO₂ Nanotube Arrays in Dye-Sensitized Solar Cells. *Nano Letters* **2005**, *6* (2), 215-218.
57. Tang, Y. B.; Chen, Z. H.; Song, H. S.; Lee, C. S.; Cong, H. T.; Cheng, H. M.; Zhang, W. J.; Bello, I.; Lee, S. T., Vertically Aligned p-Type Single-Crystalline GaN Nanorod Arrays on n-Type Si for Heterojunction Photovoltaic Cells. *Nano Letters* **2008**, *8* (12), 4191-4195.
58. Zhang, L.; Shi, E.; Li, Z.; Li, P.; Jia, Y.; Ji, C.; Wei, J.; Wang, K.; Zhu, H.; Wu, D.; Cao, A., Wire-supported CdSe nanowire array photoelectrochemical solar cells. *Physical Chemistry Chemical Physics* **2012**, *14* (10), 3583-3588.
59. Wallentin, J.; Anttu, N.; Asoli, D.; Huffman, M.; Åberg, I.; Magnusson, M. H.; Siefert, G.; Fuss-Kailuweit, P.; Dimroth, F.; Witzigmann, B.; Xu, H. Q.; Samuelson, L.; Deppert, K.; Borgström, M. T., InP Nanowire Array Solar Cells Achieving 13.8% Efficiency by Exceeding the Ray Optics Limit. *Science* **2013**, *339* (6123), 1057-1060.
60. Martinson, A. B. F.; Elam, J. W.; Hupp, J. T.; Pellin, M. J., ZnO Nanotube Based Dye-Sensitized Solar Cells. *Nano Letters* **2007**, *7* (8), 2183-2187.

61. Zhang, F.; Niu, S.; Guo, W.; Zhu, G.; Liu, Y.; Zhang, X.; Wang, Z. L., Piezo-phototronic Effect Enhanced Visible/UV Photodetector of a Carbon-Fiber/ZnO-CdS Double-Shell Microwire. *ACS Nano* **2013**, 7 (5), 4537-4544.
62. Wang, Z.; Yu, R.; Pan, C.; Liu, Y.; Ding, Y.; Wang, Z. L., Piezo-Phototronic UV/Visible Photosensing with Optical-Fiber–Nanowire Hybridized Structures. *Advanced Materials* **2015**, n/a-n/a.
63. Cullity, B. D.; Graham, C. D., *Introduction to Magnetic Materials*. Wiley: 2011.
64. Newnham, R. E., *Properties of Materials : Anisotropy, Symmetry, Structure: Anisotropy, Symmetry, Structure*. OUP Oxford: 2004.
65. Lee, J.; Joo, S.; Kim, T.; Kim, K. H.; Rhie, K.; Hong, J.; Shin, K.-H., An electrical switching device controlled by a magnetic field-dependent impact ionization process. *Applied Physics Letters* **2010**, 97 (25), 253505.
66. Jinki Hong, T. K., Sungjung Joo, Jin Dong Song, Suk Hee Han, Kyung-Ho Shin, Joonyeon Chang, Magnetic field dependent impact ionization in InSb. *arXiv:1206.1094* **2012**.
67. Delmo, M. P.; Yamamoto, S.; Kasai, S.; Ono, T.; Kobayashi, K., Large positive magnetoresistive effect in silicon induced by the space-charge effect. *Nature* **2009**, 457 (7233), 1112-1115.
68. Wan, C.; Zhang, X.; Gao, X.; Wang, J.; Tan, X., Geometrical enhancement of low-field magnetoresistance in silicon. *Nature* **2011**, 477 (7364), 304-307.
69. Dunstan, W., Variation of Photovoltaic Response with Magnetic Field for a Germanium p-n Junction. *Proceedings of the Physical Society* **1961**, 77 (2), 459.
70. Joo, S.; Kim, T.; Shin, S. H.; Lim, J. Y.; Hong, J.; Song, J. D.; Chang, J.; Lee, H.-W.; Rhie, K.; Han, S. H.; Shin, K.-H.; Johnson, M., Magnetic-field-controlled reconfigurable semiconductor logic. *Nature* **2013**, 494 (7435), 72-76.

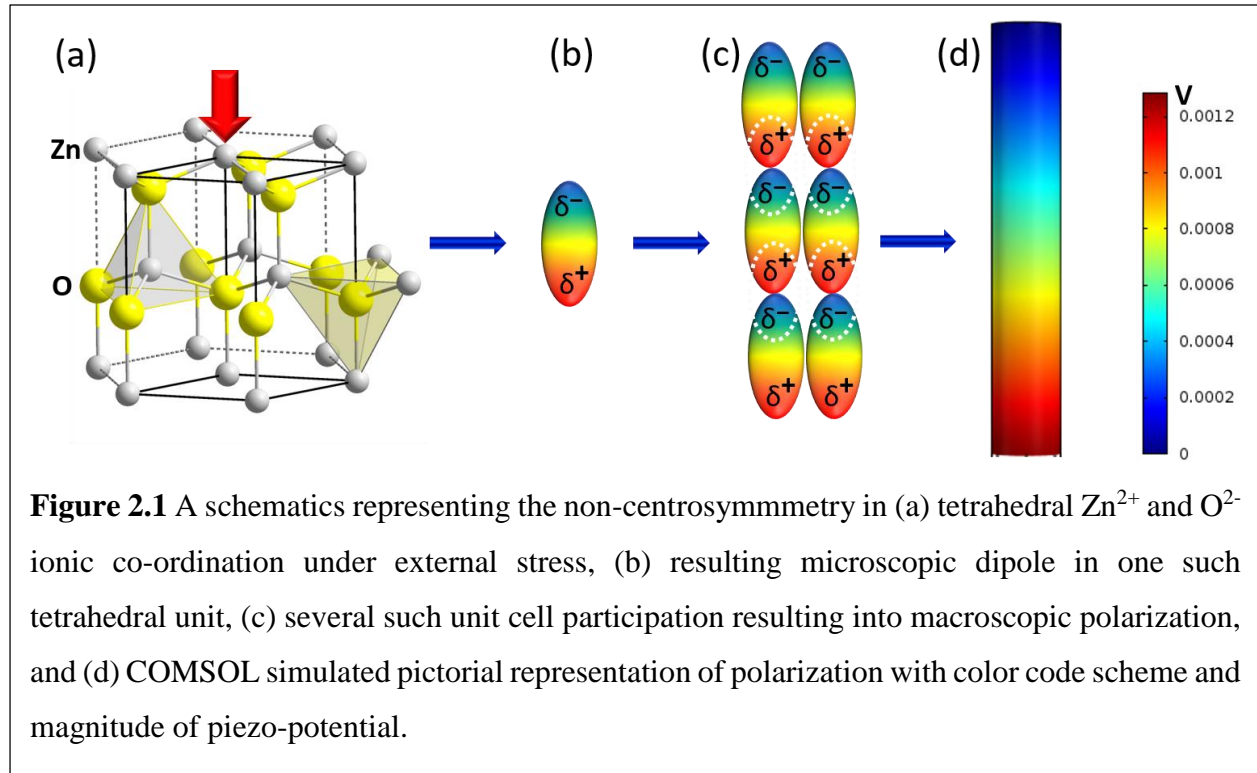
71. Xue, F.; Zhang, L.; Feng, X.; Hu, G.; Fan, F.; Wen, X.; Zheng, L.; Wang, Z., Influence of external electric field on piezotronic effect in ZnO nanowires. *Nano Res.* **2015**, *8* (7), 2390-2399.

Chapter 2 Theoretical Framework

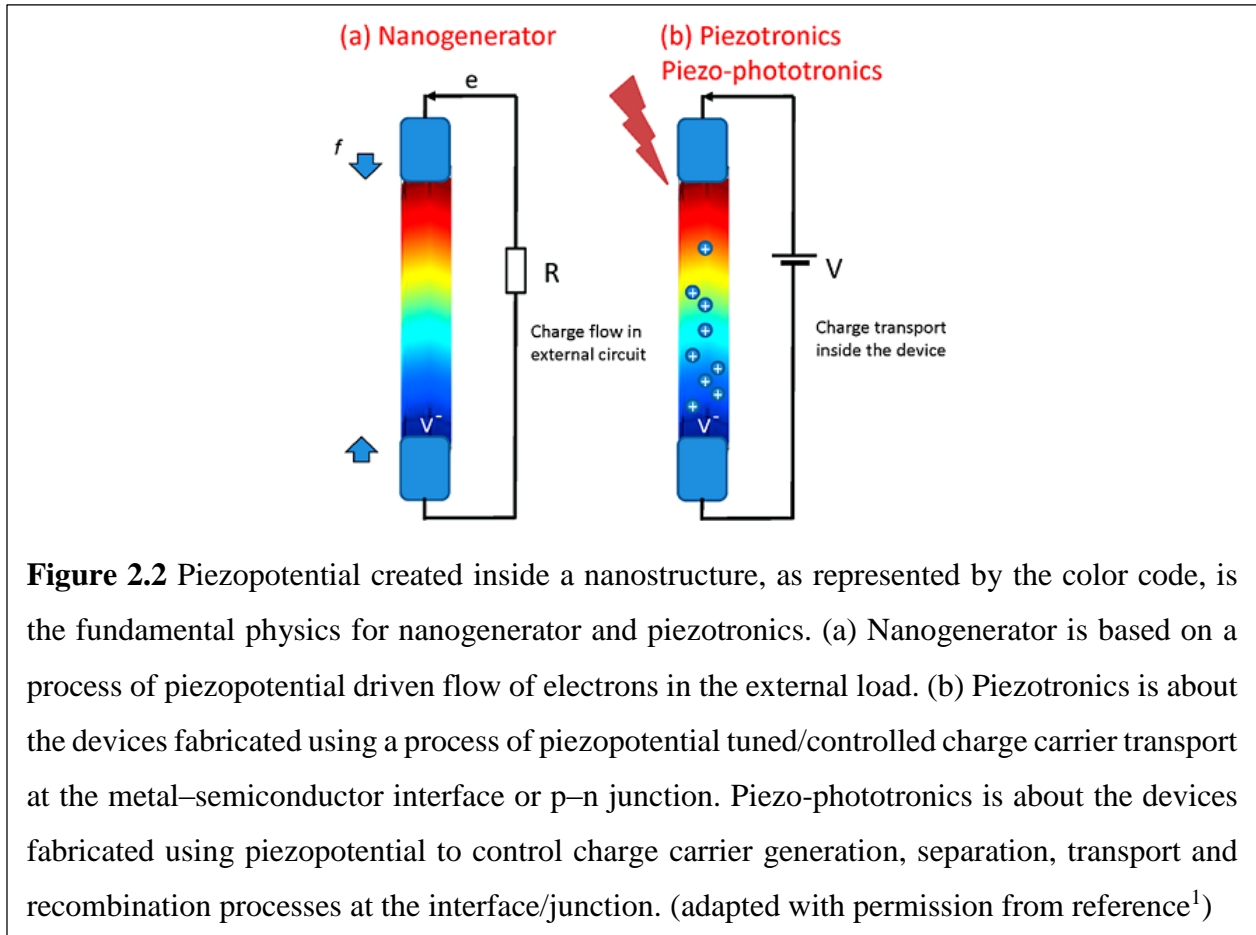
2.1 Piezoelectric nanostructures

Discovery of piezoelectric properties dates back to over more than a century, however, until recently there has been relatively less use of nanostructured piezoelectric materials in devices. The very first study of piezoelectricity in nanostructured material was demonstrated in ZnO nanowires and mechanical to electrical energy conversion was successfully achieved by coupling of semiconducting and piezoelectric properties and the device was named as nanogenerator with a vision to power up micro/nano devices for biomedical applications.² Since then the research has been focused on improving the power conversion efficiency of ZnO nanowires by utilizing arrays where multiple nanowires in parallel connection may deliver higher current and hence higher power ratings.³ Since piezoelectric property arises due to lack of center of symmetry in crystal unit cell which is responsible for ZnO piezoelectricity it can be extended to any semiconductor from wurtzite family. Recently, the nanogenerators based on GaN,⁴ CdSe,⁵ CdS,⁶ and InN⁷ has been successfully demonstrated proving that the principle of nanogenerator is extendable to several other semiconductor compounds. In particular, ZnO has a hexagonal structure with anisotropy along two mutually orthogonal directions, specifically along c- and perpendicular to c-axis. Figure 2.1 displays the microscopic origin of polarization charges in non-centrosymmetric hexagonal structure. As can be seen that tetrahedral Zn²⁺ and O²⁻ ionic co-ordination, Figure 2.1 (a), in a particular unit cell is the underlying mechanism that gives rise to microscopic dipoles, Figure 2.1 (b), under external stress. These microscopic dipoles then constructively adds up giving rise to

macroscopic dipole resulting in localization of immobile piezo-charges at nanowire ends which creates the piezo-potential and responsible for potential drop along c-axis of nanowire.



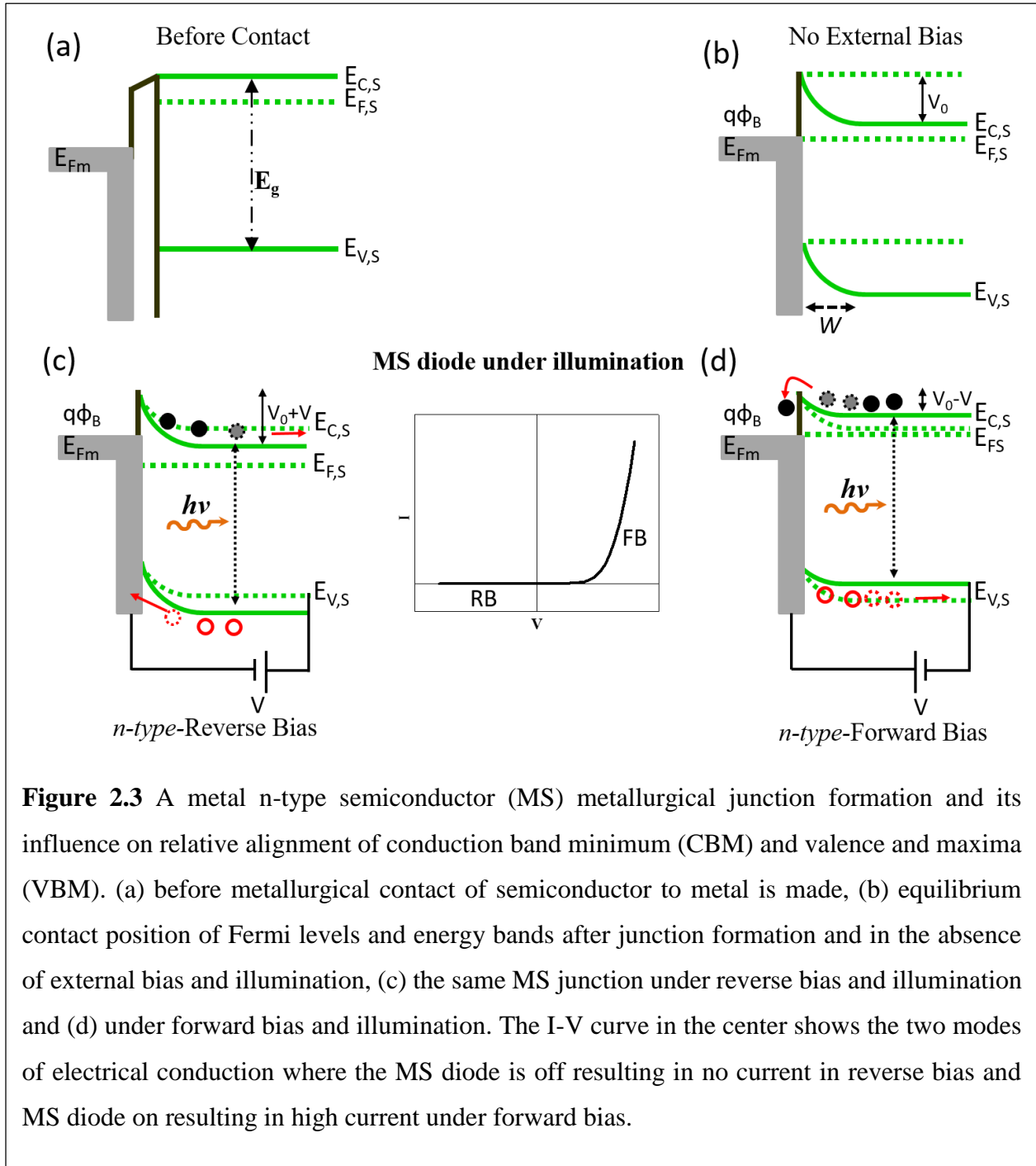
Under elastic structural deformation limit, the piezopotential created at nanowires ends can drive the flow of electrons through external circuit giving rise to mechanical to electrical energy nanogenerator phenomena. The distribution of piezopotential in a c-axis ZnO nanowire has been theoretically calculated using the Lippman theory⁸⁻¹⁰ in a dopant free ZnO nanowire. For a ZnO nanowire with a length of 1200 nm and a hexagonal side length of 100 nm, a tensile force of 85 nN creates a potential drop of approximately 0.4 V between the two ends, with the +c-side positive (Figure 2.2 (a)). When the applied force changes to a compressive strain, the piezoelectric potential reverses with the potential difference remaining 0.4 V but with the -c-axis side at a higher potential. The nanowire when connected to external bias under illumination can give rise to enhanced photo-current under piezopotential which can also act as gate filed for piezotronic transistor (Figure 2.2 (b)).



2.2 Coupling of piezoelectric and semiconducting properties

A very simple field effect transistor (FET) built on a semiconductor nanowire with conducting end electrodes can be assumed with the ends functioning as source and drain electrode and the gate voltage can be applied either from the top with a gate electrode or from the bottom substrate. By applying a source to drain voltage, V_{DS} , the charge carrier transport process in the semiconductor FET is tuned/gated in the presence of an externally applied gate voltage V_G . Alternatively, the gate voltage V_G can be replaced by the inner piezopotential generated under elastic mechanical deformation to tune/control the charge carrier transport across the channel.¹¹ This type of transistor is called as piezotronic transistor bearing the name from inner piezopotential

acting as gate field, in other words the charge transport across the channel can be controlled/tuned by applying stress to the device which gives rise to several interesting phenomena.

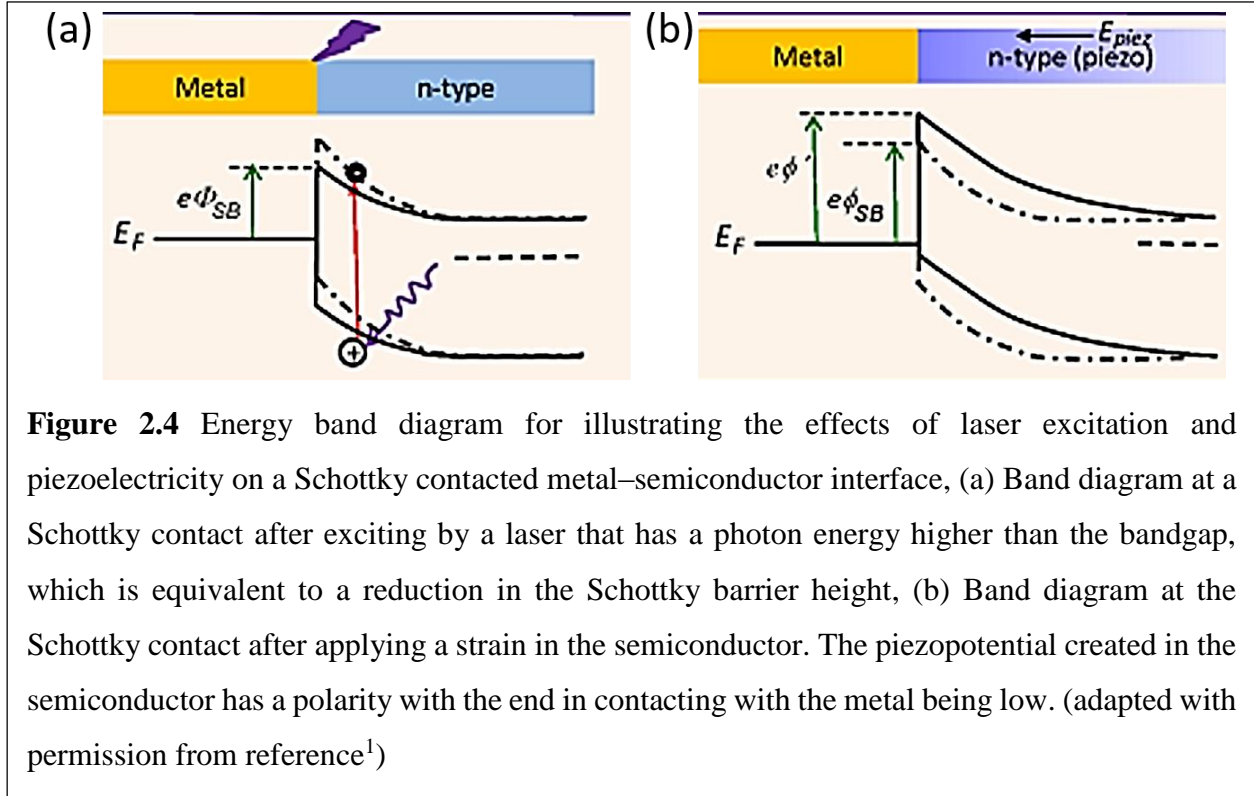


2.2.1 Piezotronic effect

Figure 2.3 displays a typical metal-semiconductor (MS) junction for an *n-type* semiconducting material where the work function (ϕ_m) of the metal is larger than the semiconductor work function (ϕ_s), as in Figure 2.3 (a). When the metal is brought in contact with semiconductor, owing to the semiconductor Fermi level, which was initially higher than metal, the charge transfer occurs until the Fermi level aligns at equilibrium (Figure 2.3 (b)).¹² The Fermi level alignment at equilibrium results in raising the electrostatic potential of the semiconductor (i.e. lowering of electron energies) relative to the metal. In *n-type* semiconductor a depletion region W is formed (Figure 2.3 (b)) near the junction. The positive charge due to uncompensated donor ions within W is equal in magnitude and opposite in sign at metal side, however this region is negligibly thin. The equilibrium contact potential V_0 developed at the junction prevents further net diffusion of electrons from semiconductor conduction band to metal. The current through the junction can only pass in forward direction i.e. when the external bias is applied with positive polarity on metal side. The equilibrium potential difference can be modified by application of external bias (Figure 2.3 (c-d)) or by internal piezopotential generated under elastic deformation, termed as piezotronic effect as mentioned earlier. In a nutshell, *piezotronic effect* is to use piezopotential to tune/control the charge transport across an interface/junction.¹³

As seen in figure 2.4 (a), the barrier height on metal side prevents net diffusion of charge carriers which decreases under illumination as a result of newly generated electron-hole pairs in addition to increasing the conductance. Once the strain is created in *n-type* semiconductor, which is also piezoelectric, a negative piezopotential at the junction effectively increases the barrier height whereas a positive piezopotential decreases the barrier height. The strain, tensile or compressive, dependent polarity of piezopotential can then be carefully chosen so as to

tune/control the barrier height in a favorable manner. The same principal and mechanism can be extended to p - n junction based devices as well.



A piezotronic transistor involves a piezoelectric semiconductor, hence electrostatic equations, current density equations, and continuity equations are required to describe the static and dynamic charge carrier transport.¹⁴ Additionally, piezoelectric equations are needed to describe the behavior of piezoelectric materials under dynamic stress conditions.¹⁵ The basic electrostatic behavior can be described by Poisson equation:

$$\nabla^2 \psi_i = \frac{\rho(r)}{\epsilon} \quad (2.1)$$

where, ψ_i is the electric potential distribution and $\rho(\mathbf{r})$ is the charge density distribution and ε is the permittivity of the material. The current–density equations that correlate the local fields, charge densities and local currents are:

$$\begin{aligned}\mathbf{J}_n &= q\mu_n n \mathbf{E} + q\mathbf{D}_n \nabla n, \\ \mathbf{J}_p &= q\mu_p p \mathbf{E} - q\mathbf{D}_p \nabla p, \\ \mathbf{J}_{cond} &= \mathbf{J}_n + \mathbf{J}_p\end{aligned}\tag{2.2}$$

Where, \mathbf{J}_n and \mathbf{J}_p are the electron and hole current densities, q is the absolute value of unit electronic charge, μ_n and μ_p are electron and hole mobilities, n and p are concentrations of free electrons and free holes, \mathbf{D}_n and \mathbf{D}_p are diffusion coefficients for electrons and holes, respectively, \mathbf{E} is the electric field, and \mathbf{J}_{cond} is the total current density.

The charge transport under external field is described by continuity equations:¹⁴

$$\begin{aligned}\frac{\partial n}{\partial t} &= G_n - U_n + \frac{1}{q} \nabla \cdot \mathbf{J}_n \\ \frac{\partial p}{\partial t} &= G_p - U_p - \frac{1}{q} \nabla \cdot \mathbf{J}_n\end{aligned}\tag{2.3}$$

where, G_n and G_p are the electron and hole generation rates, U_n and U_p are the recombination rates, respectively.

The piezoelectric behavior of the material is described by a polarization vector \mathbf{P} .

$$(\mathbf{P})_i = (e)_{ijk} (\mathbf{S})_{jk}\tag{2.4}$$

Where, \mathbf{S}_{jk} is a uniform mechanical strain and $(e)_{ijk}$ is a third order piezoelectric tensor. According to conventional theory of piezoelectric and elasticity, the constitutive equation can be written as

$$\boldsymbol{\sigma} = \mathbf{c}_E \mathbf{S} - \mathbf{e}^T \mathbf{E}$$

$$\mathbf{D} = \mathbf{eS} + \mathbf{kE} \quad (2.5)$$

where $\boldsymbol{\sigma}$ is the stress tensor, \mathbf{E} is the electric field, \mathbf{D} is the electric displacement, \mathbf{eE} is the elasticity tensor, and \mathbf{k} is the dielectric tensor. These equations can be applied to obtain analytical solutions and to visualize simplified charge distribution in metal-semiconductor contact in the presence of Schottky barrier as shown in Figure 2.5.

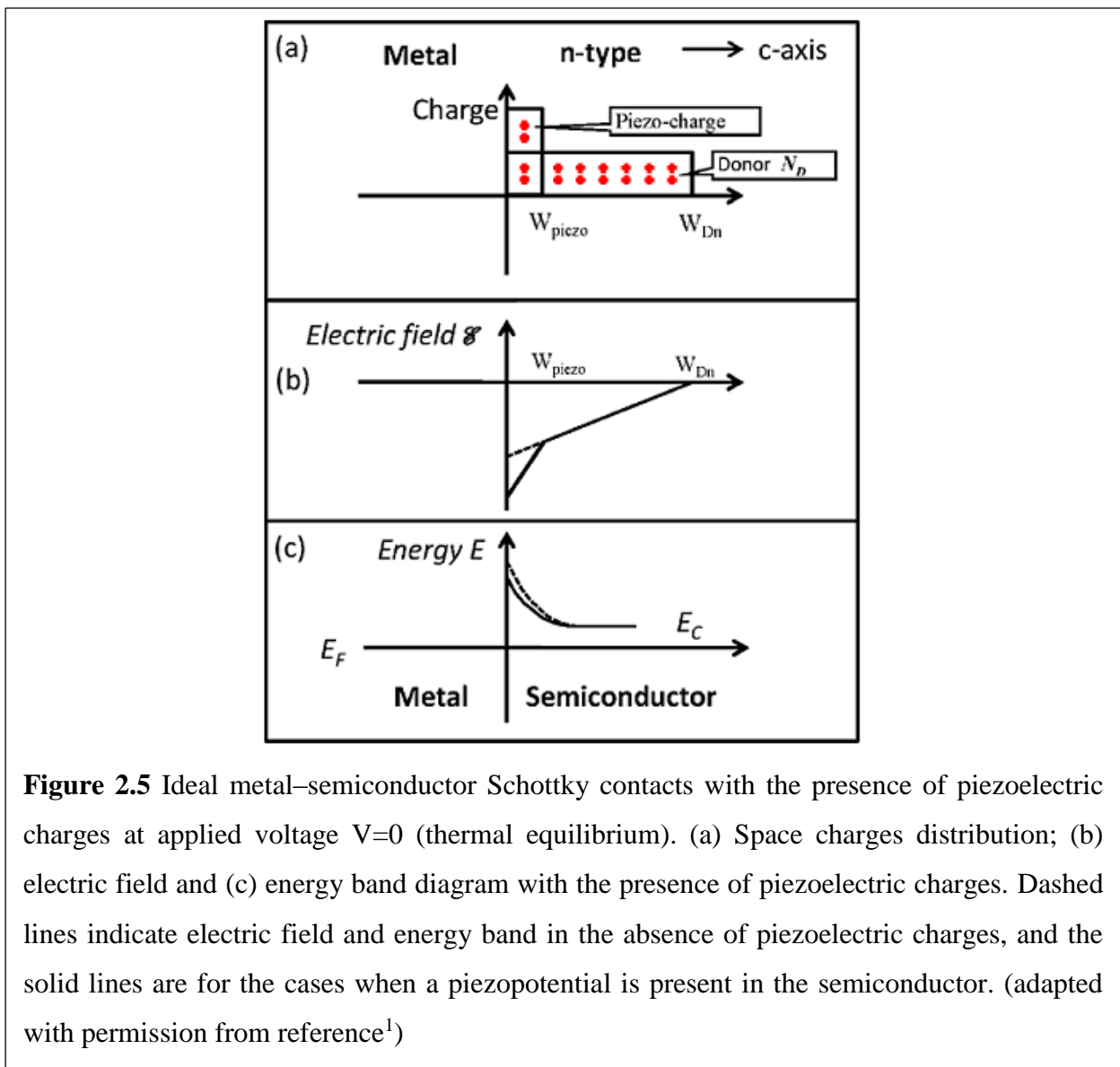


Figure 2.5 Ideal metal–semiconductor Schottky contacts with the presence of piezoelectric charges at applied voltage $V=0$ (thermal equilibrium). (a) Space charges distribution; (b) electric field and (c) energy band diagram with the presence of piezoelectric charges. Dashed lines indicate electric field and energy band in the absence of piezoelectric charges, and the solid lines are for the cases when a piezopotential is present in the semiconductor. (adapted with permission from reference¹)

The charge distribution at metal-semiconductor (M-S) interface is shown in Figure 2.5 (a), assuming that semiconductor is *n-type*. Under external strain the immobile piezo charges at semiconductor side of M-S interface modifies the Schottky barrier height and the depletion changes accordingly. Additionally, the piezopotential provides advantage in tuning the barrier height and depletion width by various magnitudes through changing the amount of strain applied on device. The carrier transport across M-S junction is dominated by majority carriers. The current density equation 2.2 can be written as¹

$$J = J_n = q\mu_n nE + aD_n \frac{dn}{dx} \quad (2.6)$$

where,

$$E = \frac{d\psi_i}{dx} = \frac{dE_c}{dx}$$

The solutions under forward bias, according to diffusion theory, can be obtained as¹

$$J_n \approx J_D \exp\left(-\frac{q\phi_{Bn}}{kT}\right) \left[\exp\left(\frac{qV}{kT}\right) - 1\right] \quad (2.7)$$

where,

$$J_D = \frac{q^2 D_n N_C}{kT} \sqrt{\frac{2qN_D(\psi_{bi} - V)}{\epsilon}} \exp\left(\frac{q\phi_{Bn}}{kT}\right)$$

J_D is the saturation current density. We can define J_{D0} as saturation current density in the absence of piezoelectric charges

$$J_{D0} = \frac{q^2 D_n N_C}{kT} \sqrt{\frac{2qN_D(\psi_{bi0} - V)}{\epsilon}} \exp\left(\frac{q\phi_{Bn0}}{kT}\right) \quad (2.8)$$

where, ψ_{bi0} and ϕ_{Bn0} are built-in potential and Schottky-barrier height in the absence of piezoelectric charges. In our case, the effect of piezoelectric charge can be considered as a perturbation to the conduction-band edge E_C . The change in effective Schottky barrier height:

$$\phi_{Bn} = \phi_{Bn0} - \frac{q^2 \rho_{piezo} W_{piezo}^2}{2\epsilon} \quad (2.9)$$

and current density,

$$J_n \approx J_D \exp\left(\frac{q^2 \rho_{piezo} W_{piezo}^2}{2\epsilon kT}\right) \left[\exp\left(\frac{qV}{kT}\right) - 1\right] \quad (2.10)$$

This means that the current transported across the M–S interface is an exponential function of the local piezo-charges, the sign of which depends on the strain. Therefore, the current to be transported can be effectively tuned or controlled by not only the magnitude of the strain, but also by the sign of the strain (tensile vs. compressive). This is the mechanism of the piezotronic transistor for M–S case.¹

2.2.2 Piezo-phototronic effect

In wurtzite semiconductors, such as ZnO, CdSe, GaN, InN and CdS, application of external stress result into a piezoelectric potential (piezopotential). The appearance of inner piezopotential can be effectively used as a “gate” voltage to tune/control the charge carrier generation, transport, and/or recombination processes at the vicinity of a M-S/p–n junction, and is known as piezo-phototronic effect.¹ The presence of piezoelectric polarization charges at the interface/junction can significantly affect the performance of light emitting diode (LED), photodetector and solar cells. The equations governing the semiconductor and piezoelectric behavior described earlier through equations 2.1 to 2.5 can also be applied as basic governing equations to describe piezo-phototronic effect. This effect can further be elaborated considering a simple metal-*n*-type-semiconductor-metal piezo-phototronic photodetector. The thermionic emission theory can be adapted for the

charge carrier transport,¹² assuming that the measurement of photon-induced current is an indication of photon intensity, which can be estimated theoretically by appropriate current density equation under forward bias:

$$J_F = A^*T^2 e^{-\frac{q}{kT}\phi_n} \left(e^{\frac{q}{kT}V} - 1 \right) \quad (2.11)$$

where, A^* is the Richardson constant, T is temperature, ϕ_n is the effective Schottky barrier height, and V is the applied voltage across the contact. For a reversely biased metal-*n-type* semiconductor junction, however the thermionic emission theory could not be accurately applied as it neglects the tunneling effects.¹⁶ In the particular case of reversely biased Schottky contact the thermionic field emission theory should be used to calculate the photocurrent density as an indicator of photon intensity.¹⁷

$$J_R = J_{sv} e^{-\frac{q}{E_0}\phi_n} e^{V_R \left(\frac{q}{kT} - \frac{q}{E_0} \right)} \quad (2.12)$$

where, J_{sv} is the slowly varying term regarding applied voltage and Schottky barrier change, V_R is the reverse voltage, q is electron charge, k the Boltzmann constant, and E_0 is a tunneling parameter of the same order of but larger than kT . Usually E_0 is larger than kT , and is constant regarding barrier height and applied voltage, so it is reasonable to assume that $E_0 = akT$, with $a > 1$, so (2.12) now becomes,¹

$$J_R = J_{sv} e^{-\frac{q}{akT}\phi_n} e^{V_R \frac{q}{kT} \left(1 - \frac{1}{a} \right)} \quad (2.13)$$

As we know that photons ($h\nu$) with energy greater than the band gap (E_g) of optical absorber will produce electron-hole pairs and under steady state illumination condition, the excess charge carrier concentration is constant which can be written as

$$\Delta n = \Delta p = \tau_n G_L(I) \quad (2.14)$$

where, n is the excess electron concentration and p the excess hole concentration under light illumination, τ_n is the carrier lifetime, and $G_L(I)$ is the rate of photon generation, which is a function of light intensity.¹⁸ In the absence of external bias and under equilibrium, the Fermi level of metal was aligned to Fermi level of semiconductor which is no more a valid case under photoexcitation as the excess charge carriers generated by photoexcitation results in splitting of previously aligned Fermi levels into two quasi Fermi levels for electrons and holes accordingly.¹⁹ As long as the photoexcitation is steady these quasi levels are preserved and can be described for electrons (E_{Fn}) and holes (E_{Fp}) as follows:

$$E_{Fn} = E_F + kT \ln \left(\frac{n_0 + \Delta n}{n_0} \right) \quad (2.15)$$

$$E_{Fp} = E_F - kT \ln \left(\frac{p_0 + \Delta p}{p_0} \right) \quad (2.16)$$

A slight modification in equation 2.9 provides a way to quantify the change in magnitude of Schottky barrier height by piezo charges and is written as:

$$\Delta \phi_{piezo} = - \frac{1}{2\epsilon} \rho_{piezo} W_{piezo}^2 \quad (2.17)$$

where, ρ_{piezo} is the density of the strain-induced piezo-charges at nanowire side of the metal–semiconductor junction, and W_{piezo} is the width of the piezo-polar charge distribution adjacent to the interface.¹

As mentioned in section 2.2.1, polarization charges produced as a result of elastic deformation are immobile and mostly remain localized at the ends of the nanowire-metal interface, shown in Figure 2.6 (a). It should be noted that the entire description of the piezo theory considers

wurtzite semiconductors as a prerequisite and some of these nanowire single crystals, such as ZnO, CdSe and GaN, preferentially grow along c-axis, the axis along which stress is applied.

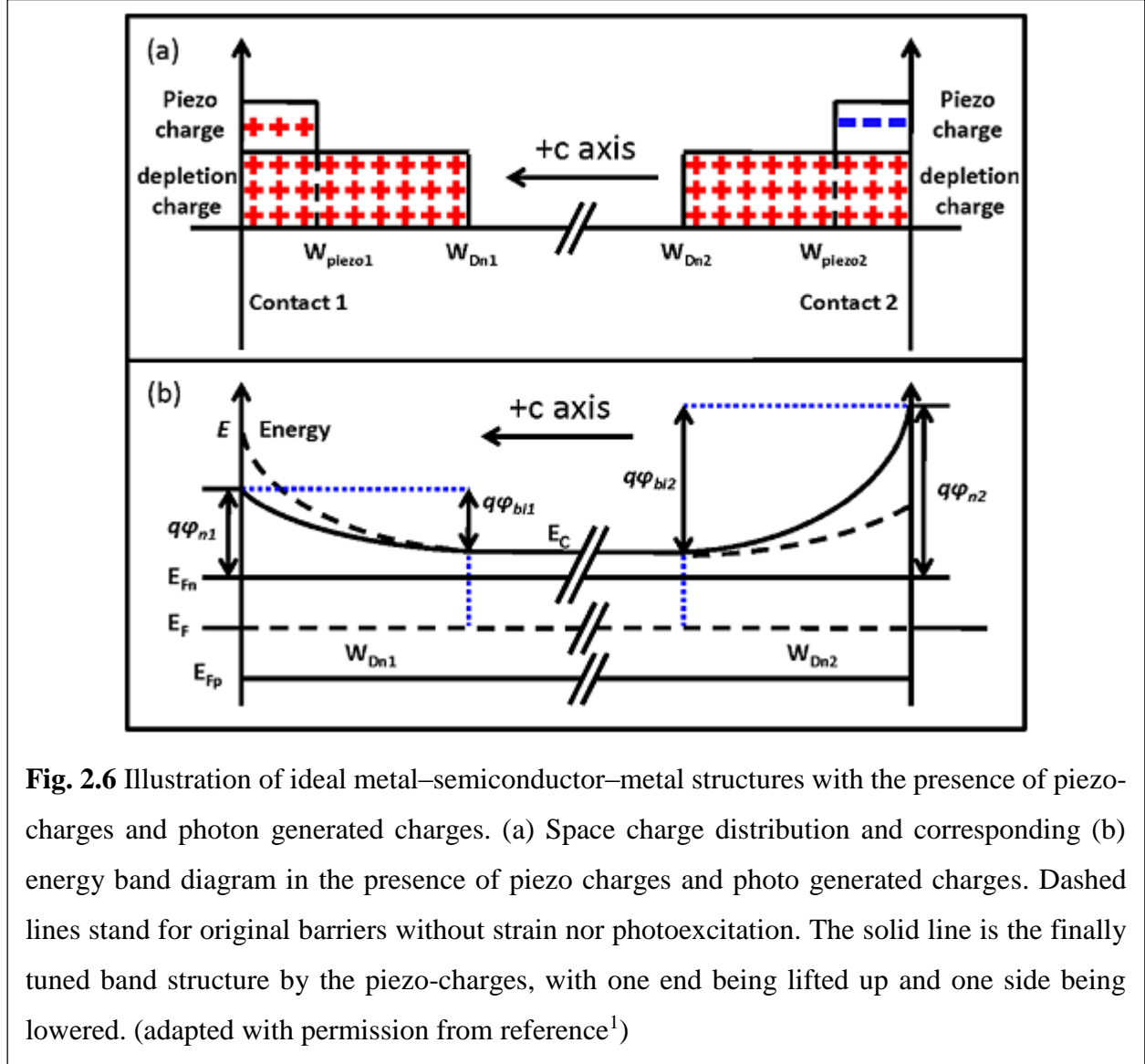


Fig. 2.6 Illustration of ideal metal–semiconductor–metal structures with the presence of piezo-charges and photon generated charges. (a) Space charge distribution and corresponding (b) energy band diagram in the presence of piezo charges and photo generated charges. Dashed lines stand for original barriers without strain nor photoexcitation. The solid line is the finally tuned band structure by the piezo-charges, with one end being lifted up and one side being lowered. (adapted with permission from reference¹)

The piezo-polarization along this direction can be described as:

$$P = e_{33}s_{33} = \rho_{piezo1}W_{piezo1} = -\rho_{piezo2}W_{piezo2} \quad (2.18)$$

where, e_{33} is piezoelectric constant, and s_{33} denotes the strain along the c- axis, ρ_{piezo1} is the density of the strain-induced piezo-charges at contact 1, and ρ_{piezo2} is the density of the strain-induced

piezo-charges at contact 2. The change in Schottky barrier height resulting from photoexcitation under steady state and piezo polarization charges can be combined together for quantification purposes:

$$\Delta\varphi_n = -\frac{1}{2\epsilon}\rho_{piezo}W_{piezo}^2 - \frac{kT}{q}\ln\left(\frac{n_0+\Delta n}{n_0}\right) \quad (2.19)$$

giving rise to modified barrier height,

$$\varphi_n = \varphi_{n0} + \Delta\varphi_n \quad (2.20)$$

where, φ_{n0} is the magnitude of Schottky barrier height prior to strain or steady state photoexcitation. The total electron only current density across a forward biased Schottky contact is:

$$J_n = J_{n0}\left(\frac{n_0+\Delta n}{n_0}\right)\exp\left(\frac{q}{kT}\frac{1}{2\epsilon}\rho_{piezo}W_{piezo}^2\right) \quad (2.21)$$

where, J_{n0} is the current density in the absence of photoexcitation or external strain, and

$$J_{n0} = A^*T^2e^{-\frac{q}{kT}\varphi_{n0}}\left(e^{\frac{q}{kT}V} - 1\right)$$

It should also be noted that the sign of polarization charges depend on the direction of strain (compressive or tensile), appearance of piezo charges can enhance or inhibit the photo excited charge carrier generation and their transport across junction.

2.3 Coupling of piezoelectric-semiconducting and magnetic properties

The coupling of piezoelectric and semiconducting materials electrical and optical properties have been extensively studied in the past decade that resulted in the novel physics of piezotronics and piezo-phototronics. Many useful device concepts such as piezotronic transistor,²⁰⁻²² photodetectors,²³⁻²⁷ solar cells^{28,29} etc. have been successfully demonstrated which opens up new

directions of exploring functional devices based on combination of intrinsic properties or external effects such as strain, electric field or magnetic field.

For instance, a recent study investigates the effect of high strength external electric field on the performance of single ZnO nanowire based piezotronic device.³⁰ Findings of this study suggests that piezotronic effect which arises from the coupling of intrinsic piezoelectric and semiconducting properties experiences dramatic changes under external electric field and the carrier transport across Schottky contact can be significantly altered by changing electric field strength. In a similar way, it can be anticipated that external magnetic field should also have similar effects on carrier transport across Schottky contacted metal-semiconductor device though the effect may not be as significant. The effect of external magnetic field has been, to some extent, studied in magnetotransistor theoretically by modelling of magnetic field induced conductivity modulation under constant direction of magnetic field.³¹ It was found that the electron and hole distribution changes under the action of Lorentz force resulting in electron and hole concentration to either grow or drop, especially near junction region, depending on sensitivity and affecting the recombination rates accordingly. The effect of a magnetic field on the carrier flow along the region of the bulk charge at the junction induces the Lorentz force deflecting the carriers either toward or away from the junction. The Lorentz force and the force of the bulk charge electric field can be added or subtracted, which leads to redistribution of the concentrations of carriers on the bulk charge area boundary. The magneto concentration effect of modulation of charge carriers in the region of the metal-semiconductor junction determines the current variation along with other sensitivity mechanisms. Apart from the governing effect of carrier deflection under the action of the Lorentz force, the sensitivity of the device is affected by the variations in the distribution of

the injected carriers near the emitter in the high density current region³² and the corresponding variation in bulk recombination. When a current with density \mathbf{J} flows along the M-S junction:

$$\mathbf{F}_L = \mathbf{J} \times \mathbf{B} \quad (2.22)$$

the Lorentz force \mathbf{F}_L occurs in the magnetic field with magnetic flux density \mathbf{B} and affects the charge carrier flow perpendicular to the junction. The modulation magnitude is dependent on current density I_C , channel length L_C and width W_C .

$$J_C = \frac{I_C}{(L_C \times W_C)} \quad (2.23)$$

Under thermal equilibrium the electric field in the area sufficiently distant from the junction regions is negligible,³³ therefore the total charge per square unit in the proximity of the junctions is equal in magnitude and opposite in polarity. Considering a metal-*n-type* semiconductor junction, the majority carriers being electrons it can be approximated that Lorentz force predominantly deflects electrons, the current density from majority carrier electrons in the magnetic field can be described as:

$$J_n = q\mu_n \left(nE + \frac{kT}{q} \frac{dn}{dx} \right) + J_n \perp \theta_n \quad (2.24)$$

where, $J_n \perp$ is component perpendicular to the magnetic field and θ_n is determined by mobility, concentration and the Hall constant, which can be described as

$$\tan \theta_n = q\mu_n n R_h(B) n \quad (2.25)$$

Limiting the consideration only by the drift current component:

$$E_n = J_n \perp R_h(B) n \quad (2.26)$$

and,

$$x_n(H) = x_n(0) - J_n R_h(B) n \frac{\varepsilon}{q N_D} \quad (2.27)$$

$$|E_M| = q N_D \frac{x_n - x_p[H]}{\varepsilon} \quad (2.28)$$

where, E_M is the maximum electric field value attained at $x=0$ due to deflection of charge carrier near junction region, x_n , x_p is the thickness of the bulk charge across semiconductor-metal side, respectively. For the particular case of metal-n-type semiconductor junction it is reasonable to assume that minority holes do not contribute to current significantly and can safely be neglected. Thus, in a magnetic field the conductive layers are formed close to the junction's bulk charge and the contact potential difference of the junction changes. Altogether, this leads to a change in the current flowing from across the interface.

2.4 Conclusion

The theoretical framework described in this chapter focusses on three major aspects namely, piezotronic, piezo-phototronic and piezo-magneto-phototronic fundamentals and are highlighted through basic mathematical formulations considering the semiconducting and piezoelectric properties inherently exhibited by wurtzite crystal structure. The mathematical formulation also clearly describes the coupling mechanism of semiconducting and piezoelectric property leading to observation of piezotronic and piezo-phototronic effect which is responsible for achieving enhanced device performance. The effect of external magnetic field on dynamic state of charge carrier transport and coupling of Lorentz force with piezotronic and piezo-phototronic effect opens up new research direction for realizing multiple functionalities from a single device. However, the field of piezo-photo-magnetotronic is still in infancy and continued research efforts are expected to understand the basic mechanism thoroughly and to enrich the viable device applications beyond proof of concept demonstrations achieved from our group.

References

1. Wang, Z. L., *Piezotronics and Piezo-Phototronics*. Springer: 2013; p 248.
2. Wang, Z. L.; Song, J., Piezoelectric Nanogenerators Based on Zinc Oxide Nanowire Arrays. *Science* **2006**, *312* (5771), 242-246.
3. Wang, X.; Song, J.; Liu, J.; Wang, Z. L., Direct-Current Nanogenerator Driven by Ultrasonic Waves. *Science* **2007**, *316* (5821), 102-105.
4. Huang, C.-T.; Song, J.; Lee, W.-F.; Ding, Y.; Gao, Z.; Hao, Y.; Chen, L.-J.; Wang, Z. L., GaN Nanowire Arrays for High-Output Nanogenerators. *Journal of the American Chemical Society* **2010**, *132* (13), 4766-4771.
5. Zhou, Y. S.; Wang, K.; Han, W.; Rai, S. C.; Zhang, Y.; Ding, Y.; Pan, C.; Zhang, F.; Zhou, W.; Wang, Z. L., Vertically Aligned CdSe Nanowire Arrays for Energy Harvesting and Piezotronic Devices. *ACS Nano* **2012**, *6* (7), 6478-6482.
6. Lin, Y.-F.; Song, J.; Ding, Y.; Lu, S.-Y.; Wang, Z. L., Piezoelectric nanogenerator using CdS nanowires. *Applied Physics Letters* **2008**, *92* (2), -.
7. Huang, C.-T.; Song, J.; Tsai, C.-M.; Lee, W.-F.; Lien, D.-H.; Gao, Z.; Hao, Y.; Chen, L.-J.; Wang, Z. L., Single-InN-Nanowire Nanogenerator with Upto 1 V Output Voltage. *Advanced Materials* **2010**, *22* (36), 4008-4013.
8. Gao, Y.; Wang, Z. L., Electrostatic Potential in a Bent Piezoelectric Nanowire. The Fundamental Theory of Nanogenerator and Nanopiezotronics. *Nano Letters* **2007**, *7* (8), 2499-2505.
9. Gao, Z.; Zhou, J.; Gu, Y.; Fei, P.; Hao, Y.; Bao, G.; Wang, Z. L., Effects of piezoelectric potential on the transport characteristics of metal-ZnO nanowire-metal field effect transistor. *Journal of Applied Physics* **2009**, *105* (11), 113707.
10. Sun, C.; Shi, J.; Wang, X., Fundamental study of mechanical energy harvesting using piezoelectric nanostructures. *Journal of Applied Physics* **2010**, *108* (3), 034309.

11. Wang, Z. L., Nanopiezotronics. *Advanced Materials* **2007**, *19* (6), 889-892.
12. Ben G. Streetman; Banerjee, S., *Solid State Electronic Devices*. 7 ed.; Pearson Education, Limited: 2005.
13. Wang, Z. L., Piezopotential gated nanowire devices: Piezotronics and piezo-phototronics. *Nano Today* **2010**, *5* (6), 540-552.
14. S. M. Sze, S. M. S., Kwok K. Ng, *Physics of semiconductor devices*. John Wiley & Sons, Inc.: 2007.
15. Ikeda, T., *Fundamentals of piezoelectricity*. Oxford university press: New York, 1990.
16. Rhoderick, E. H.; Williams, R. H., *Metal-semiconductor contacts*. Clarendon Press: 1988.
17. Neamen, D. A., *An introduction to Semiconductor devices*. McGraw-Hill: 2006.
18. Neamen, D. A., *Semiconductor physics and devices: basic principles*. McGraw-Hill: 2003.
19. Halkias, M., *Integrated Electronics*. Tata McGraw-Hill Publishing Company: 2001.
20. Wang, Z., Piezotronic Transistors. In *Piezotronics and Piezo-Phototronics*, Springer Berlin Heidelberg: 2012; pp 73-95.
21. Han, W.; Zhou, Y.; Zhang, Y.; Chen, C.-Y.; Lin, L.; Wang, X.; Wang, S.; Wang, Z. L., Strain-Gated Piezotronic Transistors Based on Vertical Zinc Oxide Nanowires. *ACS Nano* **2012**, *6* (5), 3760-3766.
22. Yu, R.; Wang, X.; Peng, W.; Wu, W.; Ding, Y.; Li, S.; Wang, Z. L., Piezotronic Effect in Strain-Gated Transistor of a-Axis GaN Nanobelt. *ACS Nano* **2015**.
23. Yang, Q.; Guo, X.; Wang, W.; Zhang, Y.; Xu, S.; Lien, D. H.; Wang, Z. L., Enhancing Sensitivity of a Single ZnO Micro-/Nanowire Photodetector by Piezo-phototronic Effect. *ACS Nano* **2010**, *4* (10), 6285-6291.

24. Zhang, Z.; Liao, Q.; Yu, Y.; Wang, X.; Zhang, Y., Enhanced photoresponse of ZnO nanorods-based self-powered photodetector by piezotronic interface engineering. *Nano Energy* **2014**, *9* (0), 237-244.
25. Wang, Z.; Yu, R.; Pan, C.; Liu, Y.; Ding, Y.; Wang, Z. L., Piezo-Phototronic UV/Visible Photosensing with Optical-Fiber–Nanowire Hybridized Structures. *Advanced Materials* **2015**, n/a-n/a.
26. Zhang, F.; Ding, Y.; Zhang, Y.; Zhang, X.; Wang, Z. L., Piezo-phototronic Effect Enhanced Visible and Ultraviolet Photodetection Using a ZnO–CdS Core–Shell Micro/nanowire. *ACS Nano* **2012**, *6* (10), 9229-9236.
27. Zhang, F.; Niu, S.; Guo, W.; Zhu, G.; Liu, Y.; Zhang, X.; Wang, Z. L., Piezo-phototronic Effect Enhanced Visible/UV Photodetector of a Carbon-Fiber/ZnO–CdS Double-Shell Microwire. *ACS Nano* **2013**, *7* (5), 4537-4544.
28. Boxberg, F.; Søndergaard, N.; Xu, H. Q., Photovoltaics with Piezoelectric Core–Shell Nanowires. *Nano Letters* **2010**, *10* (4), 1108-1112.
29. Pan, C.; Niu, S.; Ding, Y.; Dong, L.; Yu, R.; Liu, Y.; Zhu, G.; Wang, Z. L., Enhanced Cu₂S/CdS Coaxial Nanowire Solar Cells by Piezo-Phototronic Effect. *Nano Letters* **2012**, *12* (6), 3302-3307.
30. Xue, F.; Zhang, L.; Feng, X.; Hu, G.; Fan, F.; Wen, X.; Zheng, L.; Wang, Z., Influence of external electric field on piezotronic effect in ZnO nanowires. *Nano Res.* **2015**, *8* (7), 2390-2399.
31. Kozlov, A. V.; Cheremisinov, A. A.; Polomoshnov, S. A.; Tikhonov, R. D.; Shamanaev, S. V. In *Model of effect of pn-junction magnetic field modulation*, Micro/Nanotechnologies and Electron Devices (EDM), 2011 International Conference and Seminar of Young Specialists on, June 30 2011-July 4 2011; 2011; pp 137-139.
32. Tikhonov, R. D., Magnetoconcentration effect on a base pn junction of a bipolar magnetotransistor. *Russ Microelectron* **2010**, *39* (5), 340-351.
33. Ashcroft, N. W.; Mermin, N. D., *Solid State Physics*. Holt, Rinehart and Winston: 1976.

Chapter 3 CdSe/ZnTe core/shell nanowire array piezo-phototronic photodetector

3.1 Introduction

One dimensional nanostructures of non-centrosymmetric semiconducting crystals have been investigated for their potential applications in mechanical to electrical energy harvesters to power micro/nano systems.¹ A mechanical deformation in non-centrosymmetric piezoelectric crystals produces piezopotential² that could drive the flow of electron through external circuit converting mechanical energy into electrical energy. The conversion of mechanical into electrical energy was first demonstrated for ZnO nanowire array by scanning AFM tip over individual nanowires.³ Subsequently, the energy conversion was also achieved from 3D ZnO nanowire array by using Pt coated zigzag Silicon electrode⁴ mimicking AFM tip to have more nanowires in parallel contact to achieve higher currents and hence improved power output, which makes it even more suitable for practical applications. Recent studies have also shown that semiconducting, optical and piezoelectric properties can be combined together resulting into observation of novel phenomena that could influence the charge carrier generation, separation, recombination and transport and is termed as piezotronic⁵ and piezo-phototronic effect.⁶ One dimensional nanostructures are especially attractive for piezo-phototronic device application in view of their large surface area and excellent unidirectional charge carrier transport and proof of concept has been demonstrated in fabricating a single ZnO micro-/nanowire based UV photodetector with enhanced photosensing performance⁷, and also in tuning and improving the performance of light emitting devices.^{8,9} It has been found that inner piezopotential appearing as a result of elastic structural deformation creates polarization charges¹⁰ which can tune the metal-semiconductor-

metal (M-S-M) junction properties by lowering (positive polarity) or raising (negative polarity) the valence (VBM) and conduction band (CBM) edge and hence the charge carrier transport across the junction. From the same principle, it is anticipated that energy conversion and piezo-phototronic effect can be realized in core/shell systems composed of non-centrosymmetric materials as well, that could open up new avenues for potential technological applications.

Particularly in type-II core/shell nanowires, the carrier lifetime can be dramatically increased through separation of electrons and holes in different conducting channels provided by the core/shell nanowire geometry.^{11,12} Additionally, in core/shell nanowires photo-absorption and carrier transport takes place in an orthogonal direction, thereby reducing recombination and scattering losses and, as a result, improving quantum efficiency.¹³⁻¹⁶ This strategy was effectively employed to enhance the broad-band photodetection response in a single ZnO/CdS core/shell nanowire device.¹⁷ Regarding the core/shell architecture, three dimensional (3D) core/shell nanowire arrays provides additional advantages over single nanowire-based devices owing to their unique features, such as a large surface area, excellent multichannel charge transport, and enhanced light absorption through light trapping and scattering^{18,19} and the same was used to realize a 3D ZnO/CdS core/shell, micro-/nanowire-based, UV/visible photodetector.²⁰ Based on these findings it can be envisaged that piezo-electric field created in wurtzite nanowire core in core/shell nanowires can be effectively used to enhance the photosensing response. Notably, a high quality interface between core and shell is crucial to inhibit interfacial recombination in addition to optimal charge carrier separation that could result into higher quantum efficiency.

*This chapter is adapted from: Rai S. C., Wang K., Chen J., Marmon J. K., Bhatt M., Wozny S., Zhang Y., Zhou W. (2015). Enhanced Broad Band Photodetection through Piezo-Phototronic Effect in CdSe/ZnTe Core/Shell Nanowire Array. *Adv. Electron. Mater.*, doi: 10.1002/aelm.201400050.

CdSe and ZnTe are important II-VI semiconductor material²¹ having application in variety of optoelectronic devices such as photodetectors,^{22,23} solar cells,²⁴ transistors²⁵⁻²⁸ and field-emitters²⁹ etc. Apparently, CdSe and ZnTe are excellent candidates for heteroepitaxial junction formation in view of their small lattice mismatch, similar thermal expansion coefficient and type-II band alignment.³⁰ The type-II alignment gives rise to an effective band gap of 1.1 eV as required for maximal absorption of the solar spectrum. More interestingly, it was found that ZnTe shell grows epitaxially on CdSe core, implying that the wurtzite core induces the crystallization of ZnTe in the wurtzite form which, so far, is known to crystallize in zinc blend structure at room temperature. Recent reports have also shown nanogenerators based on array of CdSe nanowires³¹ along with observation of piezo-phototronic effect in single CdSe nanowire³² which makes it an ideal candidate as core material in core-shell nanowire systems to investigate the piezo-phototronic effect in CdSe/ZnTe core-shell photodetectors. It is reasonable to believe that a 3D architecture of CdSe/ZnTe core-shell nanowire array could boost the overall efficiency of the photodetector by improving absorption/trapping of sunlight more efficiently and by efficient charge transport across epitaxial interface.

3.2 Experimental

Synthesis of CdSe/ZnTe core/shell nanowire array was done *via* a two-step process. Firstly, CdSe nanowire array was grown on muscovite mica (Pelco[®] Mica Sheets, grade V5) substrate by chemical vapor deposition. Secondly, as grown CdSe nanowire array on mica substrate was transferred into a home built pulsed laser deposition system. Figure 3.1 represents the detailed schematics of the two step synthetic process involving CDV and PLD.

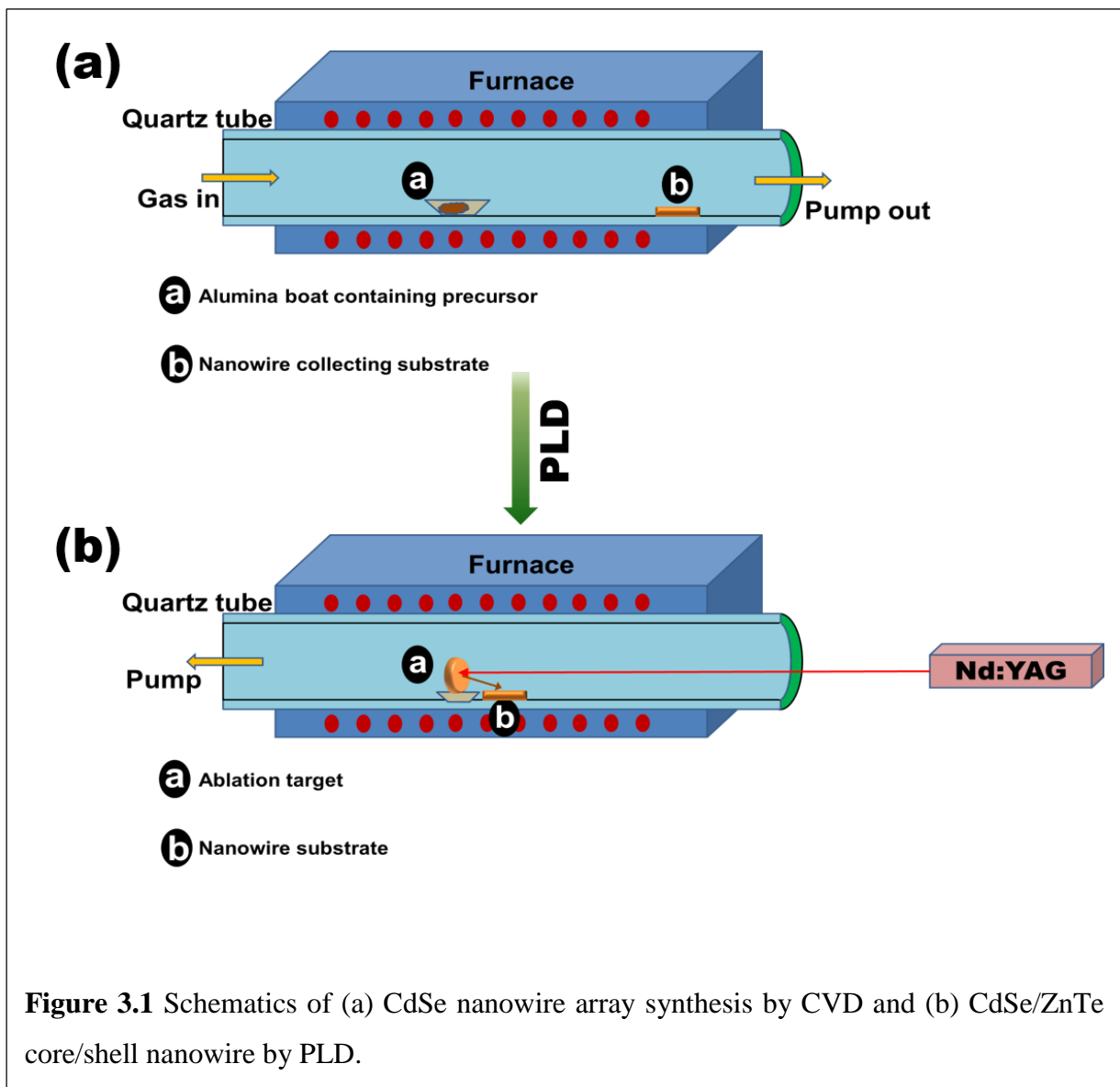
3.2.1 CVD growth of CdSe nanowire array on mica

CdSe target was prepared by cold pressing the CdSe powder to obtain target which was used for deposition of textured CdSe seed layer. Freshly cleaved muscovite mica substrate was then loaded into electron beam evaporation system (K. J. Lesker, PVD75) and a 50-100 nm thin film of CdSe was grown at a substrate temperature of 380 °C followed by spontaneous cooling to room temperature. The as deposited substrate was then coated with a 3 nm gold (Au) layer by DC sputtering (Cressington coating system, 308R), which serves as a catalyst for the nanowire array growth *via* vapor-liquid-solid (VLS) growth mechanism. The substrate was transferred in a 1 inch split zone tube furnace (Lindberg Blue M) consisting of 0.1 gram of CdSe powder loaded into alumina crucible and positioned in the center of the furnace as seen in Figure 3.1 (a). The tube was pumped down to 30 mTorr and purged by Ar/H₂ mixture several times before it was backfilled to atmospheric pressure by Ar/H₂ mixture. The temperature was ramped up to 750 °C @ 40 °C/minute and reaction was carried out for a total of 1 hour during which Ar/H₂ ambient was consistently maintained by 200 standard cubic centimeters per minute (sccm) Ar/H₂ flow. It should be noted that the textured CdSe film on muscovite mica substrate is crucial to achieve quasi aligned nanowire array growth in conjunction with the gold (Au) catalyst which controls the diameter of the individual nanowire in the array.³³ The nanowire array was deposited on substrate in downstream low temperature region and was taken out at room temperature after spontaneous cooling was complete.

3.2.2 CdSe/ZnTe core/shell nanowire array by PLD

In order to synthesize CdSe/ZnTe core-shell nanowires, the muscovite mica substrate with as-grown CdSe nanowire array was transferred into a home built pulsed laser deposition system depicted in Figure 3.1 (b). Cold pressed pellet of ZnTe powder (99.95%, Alfa Aesar) was used as

the deposition source. The distance between the ZnTe target and mica substrate was measured as 25 mm. The quartz chamber was pumped down to 30 mTorr and the temperature was ramped up to 350 °C @ 20 °C/minute. Nd:YAG laser (LOTIS-TII, LS2147) with fundamental harmonic of 1064 nm was used to ablate the target at an energy flux of 360 mJ/cm² with a frequency of 5 Hz. The ablation was performed for 10-15 min, and the final product was collected for structural and optical characterization and device fabrication.



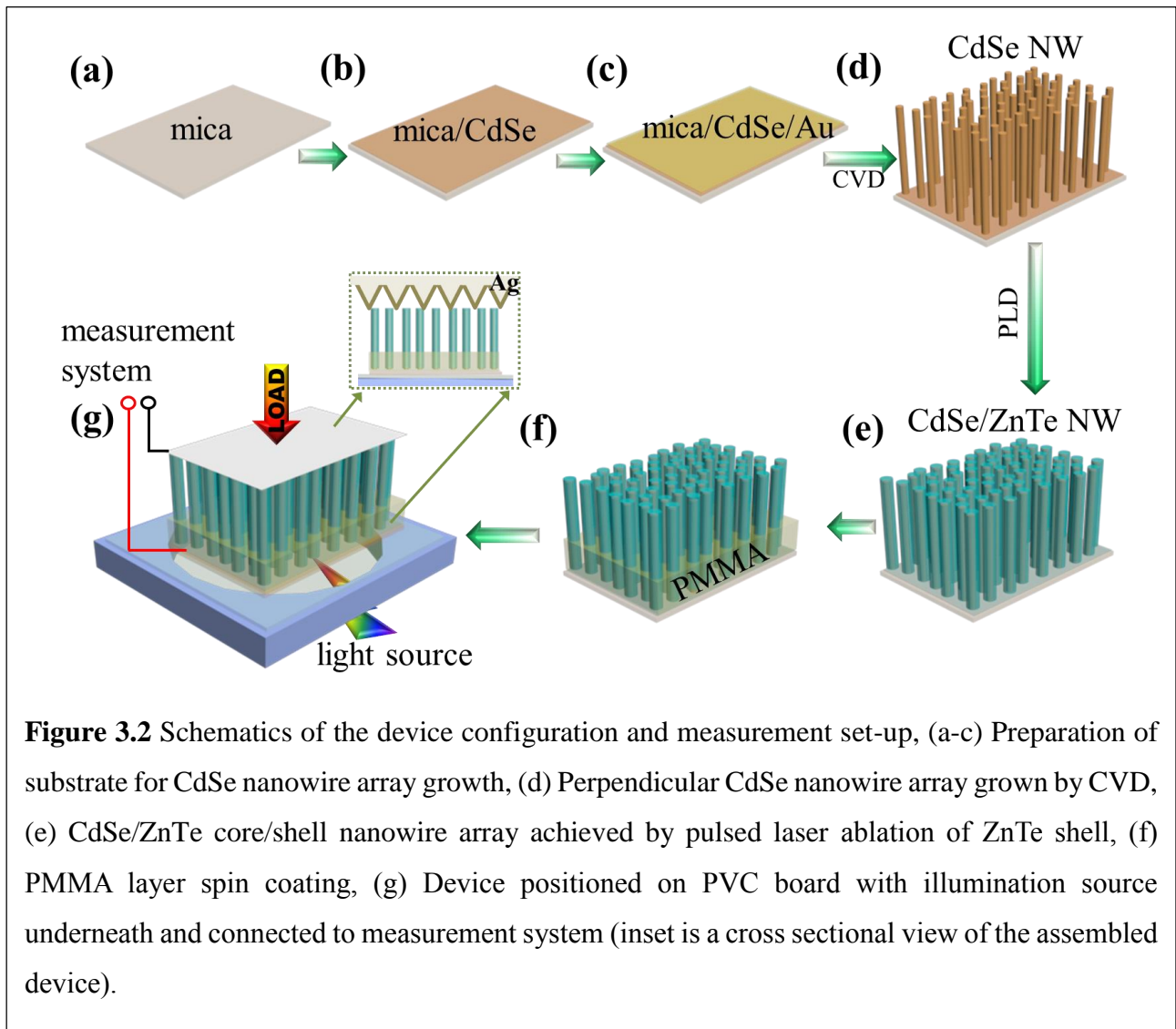
3.2.3 Materials characterization

Structural characterization of CdSe and CdSe/ZnTe core/shell nanowire array was performed by Carl Zeiss 1530 variable pressure (VP) field-emission scanning electron microscope (FESEM) operated at 10 kV, and an FEI Tecnai F20-UT high-resolution transmission electron microscope (FETEM) equipped with a nanoprobe energy-dispersive X-ray spectroscope (EDS).

3.2.4 Device fabrication and measurements

A photodetector was fabricated by positioning a silver (Ag) coated polyester grating on top of an as-synthesized CdSe/ZnTe core/shell nanowire array on mica substrate to achieve optimal bending of the perpendicular core/shell nanowires.⁴ A detailed schematic of device integration and the measurement configuration is shown in Figure 3.2. Briefly, as-synthesized CdSe/ZnTe core/shell nanowires array was coated by a thin layer of PMMA (~2 μm) to avoid a possible short circuit and to provide structural integrity. A thin polyester sheet with a parallel lined grating containing 12700 lines/inch (Edmund Optics) (see the inset of Figure 3.2) was sputter coated with a 100 nm thin Ag layer that functions as a top electrode. The pitch and trough of the grating, 1 μm and 0.6 μm , respectively is enough to accommodate nanowires to promote bending when compressional load is applied. Cu leads with silver paste were connected to bottom textured CdSe film and top electrode for carrying electrical measurements. A typical device photograph is shown in Figure 3.3 (a) with dimensional details displaying a typical device area of ~15 mm². In order to investigate the broad band optical absorption behavior of the photodetector, we performed wide range (300-800 nm) UV-Vis absorption measurements, presented in Figure 3.3 (b) in addition to the discrete wavelength measurements performed at three different excitation sources (UV, Blue, Green). Specifically, UV/Visible absorption spectrum (Figure 3.3 (b)) was collected on bare muscovite mica substrate, mica/CdSe film and mica/CdSe film/CdSe/ZnTe core/shell nanowire

array. No absorption was observed for bare mica between 350-800 nm wavelengths, and the absorption for mica/CdSe film is significantly lower than that of core/shell nanowire array, which confirms that absorption predominantly takes place in the core/shell nanowire array. The electrical measurements were carried out using low noise current pre-amplifier (SR-570), and a source meter (Keithley 2401) coupled with computer interface.



3.3 Results and Discussion

3.3.1 Structure characterization

Figure 3.4 (a) shows a typical low magnification FESEM image of a CdSe nanowire array grown on muscovite mica substrate by chemical vapor deposition (CVD) method. The nanowires are well aligned and are oriented perpendicular to the substrate resulting from the bottom textured CdSe seed layer. They have a length around 5 μm and a diameter around 200 nm . Gold (Au) nanocatalysts are visible at each nanowire end, thereby implying the characteristic vapor-liquid-solid (VLS) growth mechanism.

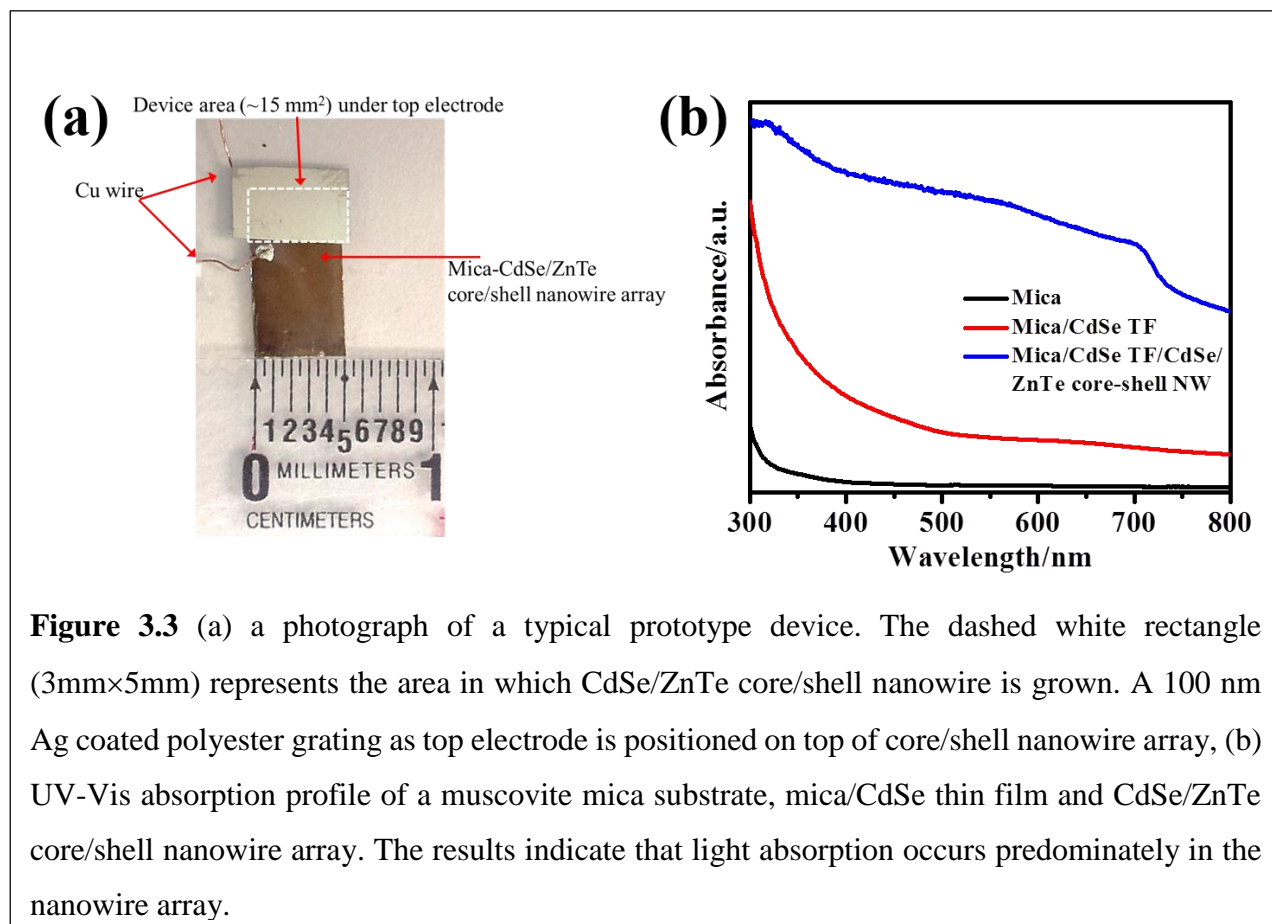
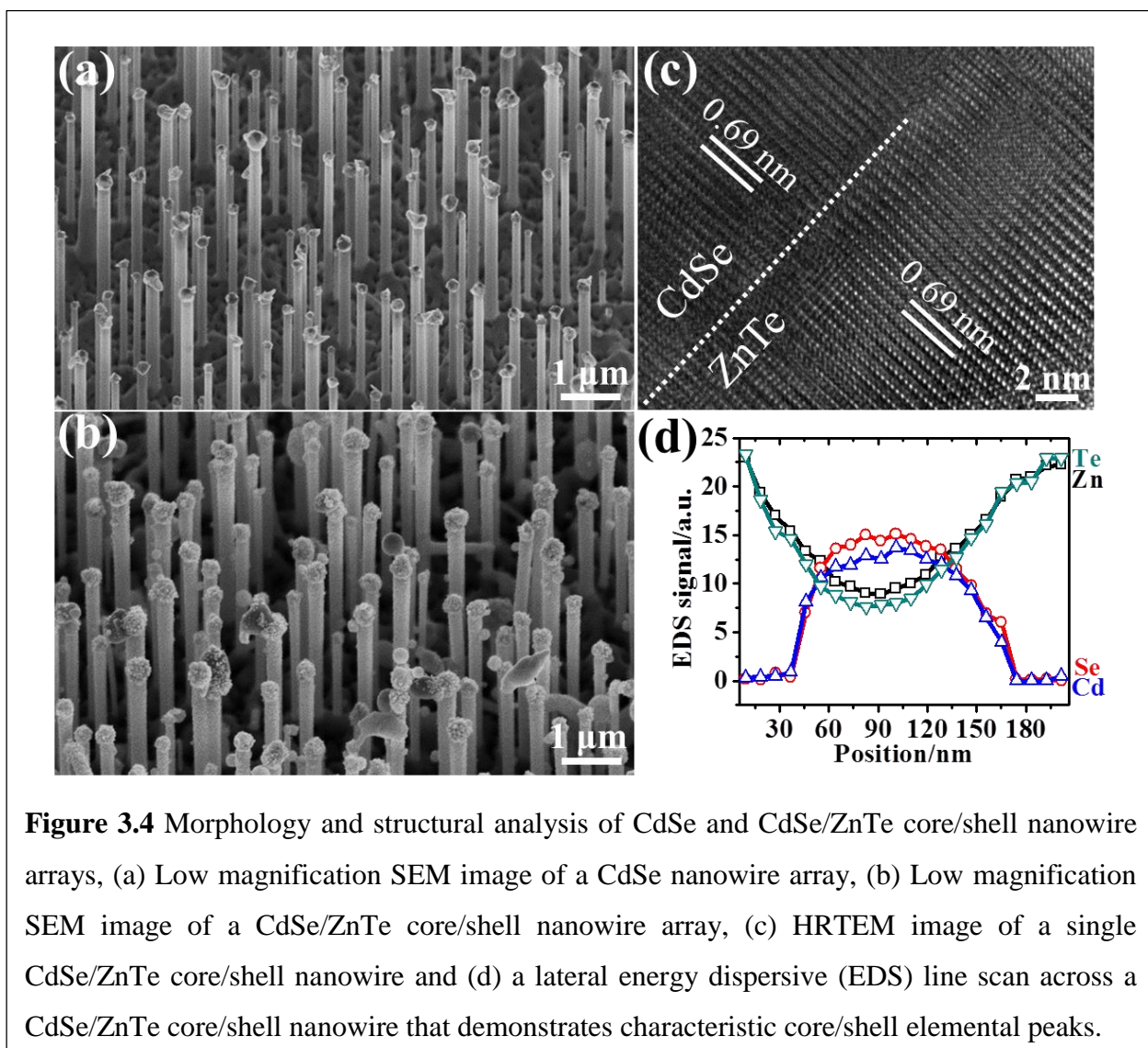


Figure 3.3 (a) a photograph of a typical prototype device. The dashed white rectangle (3mm \times 5mm) represents the area in which CdSe/ZnTe core/shell nanowire is grown. A 100 nm Ag coated polyester grating as top electrode is positioned on top of core/shell nanowire array, (b) UV-Vis absorption profile of a muscovite mica substrate, mica/CdSe thin film and CdSe/ZnTe core/shell nanowire array. The results indicate that light absorption occurs predominately in the nanowire array.

The nanowire aspect ratios (length/ diameter) were maintained between 20 to 30 in order to provide the necessary rigidity to withstand incoming ZnTe vapor flux, generated from the subsequent laser ablation process. As shown in the Figure 3.4 (a), the rational density of nanowires was obtained by carefully controlling the Au catalyst's layer thickness, thus ensuring an optimal ZnTe shell layer coating on the CdSe nanowires with minimized shadow effect.



Apparently, the diameter of CdSe/ZnTe core/shell nanowires, as seen in Figure 3.4 (b), increases slightly compared to bare CdSe nanowires in Figure 3.4 (a) as a result of ZnTe shell layer deposition. A HRTEM image of a single CdSe/ZnTe core/shell nanowire (Figure 3.4 (c)) reveals good epitaxial growth of the ZnTe shell on the CdSe core nanowire as previously reported.³⁰ A lateral energy dispersive X-ray (EDS) line scan across the CdSe/ZnTe core/shell nanowire clearly demonstrates a characteristic core/shell elemental distribution (Figure 3.4 (d)), further confirming the successful synthesis of a CdSe/ZnTe core/shell nanowire array with an abrupt, nearly lattice-matched interface.

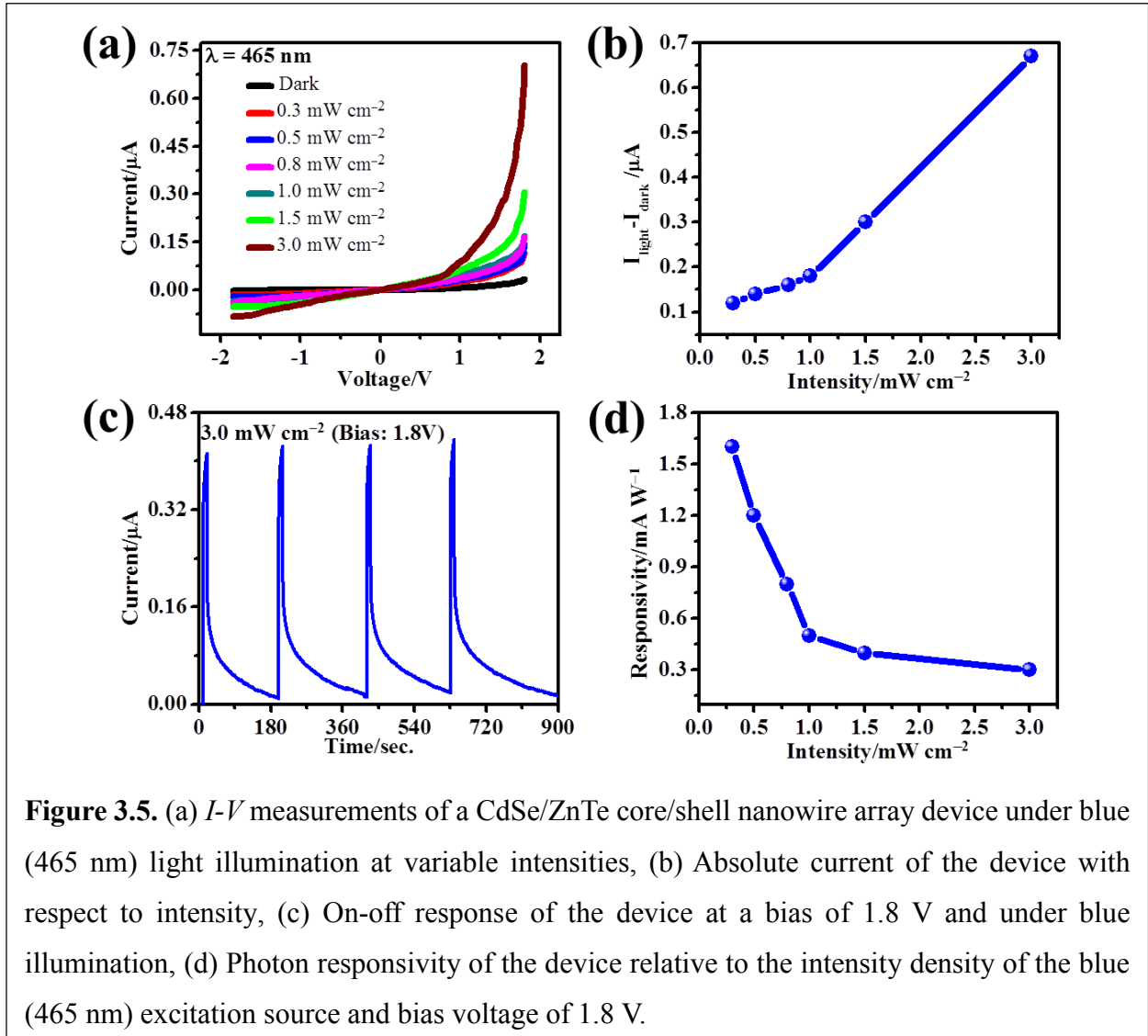
3.3.2 CdSe/ZnTe Core/Shell Nanowire Array Photodetector

3.3.2.1 Photodetector Under Blue Light Illumination

The performance of a CdSe/ZnTe core/shell photodetector under blue illumination ($\lambda = 465$ nm) is presented in Figure 3.5. A typical dark I - V response and under different illumination densities is displayed in Figure 3.5 (a), the device photo-current reached $0.71 \mu\text{A}$, which is about a 20-fold improvement compared to the dark current value of $0.03 \mu\text{A}$ with an applied bias of 1.8V and 3.0 mW cm^{-2} illumination density. The sensitivity of the photodetector, defined as $\frac{I_{\text{light}} - I_{\text{dark}}}{I_{\text{dark}}}$, is found to be $\sim 2.27 \times 10^3 \%$ under 3.0 mW cm^{-2} , which is an order of magnitude higher than the best performance of previously reported heterojunction photodetectors, such as P3HT:CdSe³⁴ and n-CdSe/p-Cu₂O.³⁵ Additionally, there is no obvious saturation under a wide range of illumination densities, which range from 0.3 to 3.0 mW cm^{-2} .

This makes the device functional between low to high illumination, which is a critical feature for industrial application. The photocurrent's dependence upon the illumination density is illustrated in Figure 3.5 (b). Figure 3.5 (c) shows the photodetector's on-off current response under blue illumination ($\lambda = 465$ nm). The device quickly attains its peak current value, and shows a

response speed as high as 0.1s, which is an order of magnitude higher than a reported ZnTe nanowire-based photodetector.³⁶ The improved response stems from increased photo-absorption and electron transport in the CdSe core. It is also observed that the off-current decays slowly, which was attributed to the persistent photocurrent arising from charged surface trap states, and is an effect previously found in other binary semiconductor nanowires.³⁷⁻⁴⁰



The performance of a photodetector is also determined by its total responsivity,⁴¹ as shown in Figure 3.5 (d), which is defined as

$$R = \frac{I_{light} - I_{dark}}{P_{ill}}$$

$$P_{ill} = I_{ill} \cdot A,$$

where I_{light} , and I_{dark} , are currents when the photodetector is under illumination and in the dark respectively. P_{ill} , I_{ill} , and A are the excitation power, illumination density, and the active/illuminated device area respectively. The calculated responsivity of a CdSe/ZnTe core/shell photodetector under 0.3 mW cm^{-2} of blue excitation ($\lambda = 465$) is 1.6 mA W^{-1} , which is comparable with other heterojunction photodetectors.⁴²⁻⁴⁴ The decrease in responsivity at higher illumination densities can be attributed to hole-trapping saturation and a transparent Schottky barrier at higher illumination densities.^{7,32}

3.3.2.2 Photodetector Under Green and UV Light Illumination

Similar I - V measurements were also performed under green ($\lambda = 520 \text{ nm}$, Figure 3.6) and UV illumination ($\lambda = 385 \text{ nm}$, Figure 3.7) to investigate the wide spectral responses of the photodetector. The detailed measurements are summarized in Figure 3.6 for green illumination and 3.7 for UV illumination. The measurements under green and UV illumination show an increase in absolute current from $0.03 \mu\text{A}$ to $0.18 \mu\text{A}$ (3.24 mW cm^{-2} , 1.8V bias) and $0.13 \mu\text{A}$ (1.32 mW cm^{-2} , 1.8V bias), respectively. The significant increase in absolute current (an order of magnitude under blue, a 6-fold increase under green, and more than a 4-fold increase under UV) can be attributed to the epitaxial interface in a CdSe/ZnTe core/shell nanowire array, which leads to significantly reduced recombination and scattering losses. Additionally, it can be seen that the response speed of the device is well preserved (0.1s) as observed under blue light illumination,

which indicates that the CdSe/ZnTe core/shell nanowire array photodetector has a fast and saturation free response under a wide optical range from 385 to 520 nm and illumination densities, e.g. from 0.04 ($\lambda = 385$ nm) to 3.24 mW cm^{-2} ($\lambda = 520$ nm).

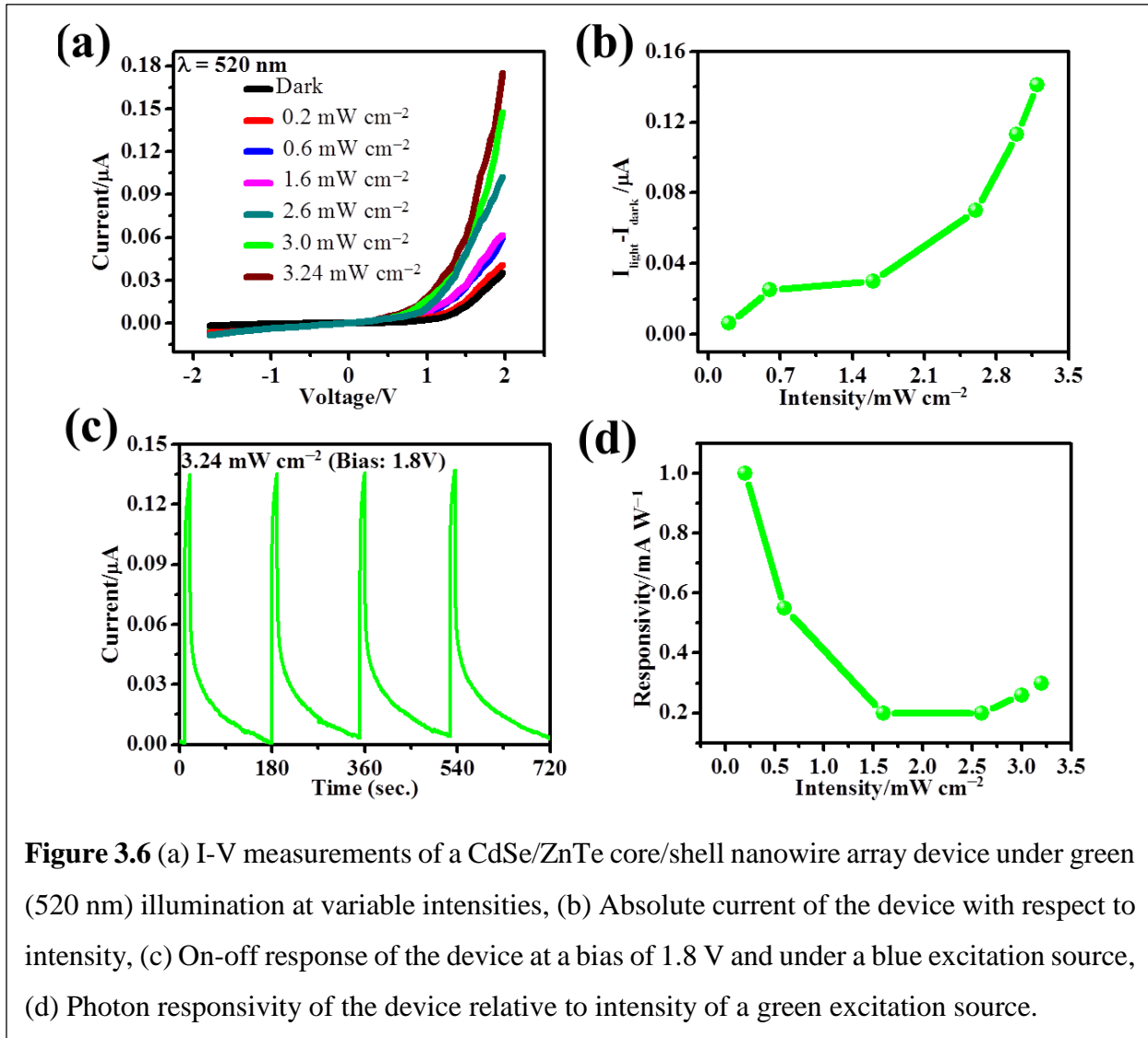


Figure 3.6 (a) I-V measurements of a CdSe/ZnTe core/shell nanowire array device under green (520 nm) illumination at variable intensities, (b) Absolute current of the device with respect to intensity, (c) On-off response of the device at a bias of 1.8 V and under a blue excitation source, (d) Photon responsivity of the device relative to intensity of a green excitation source.

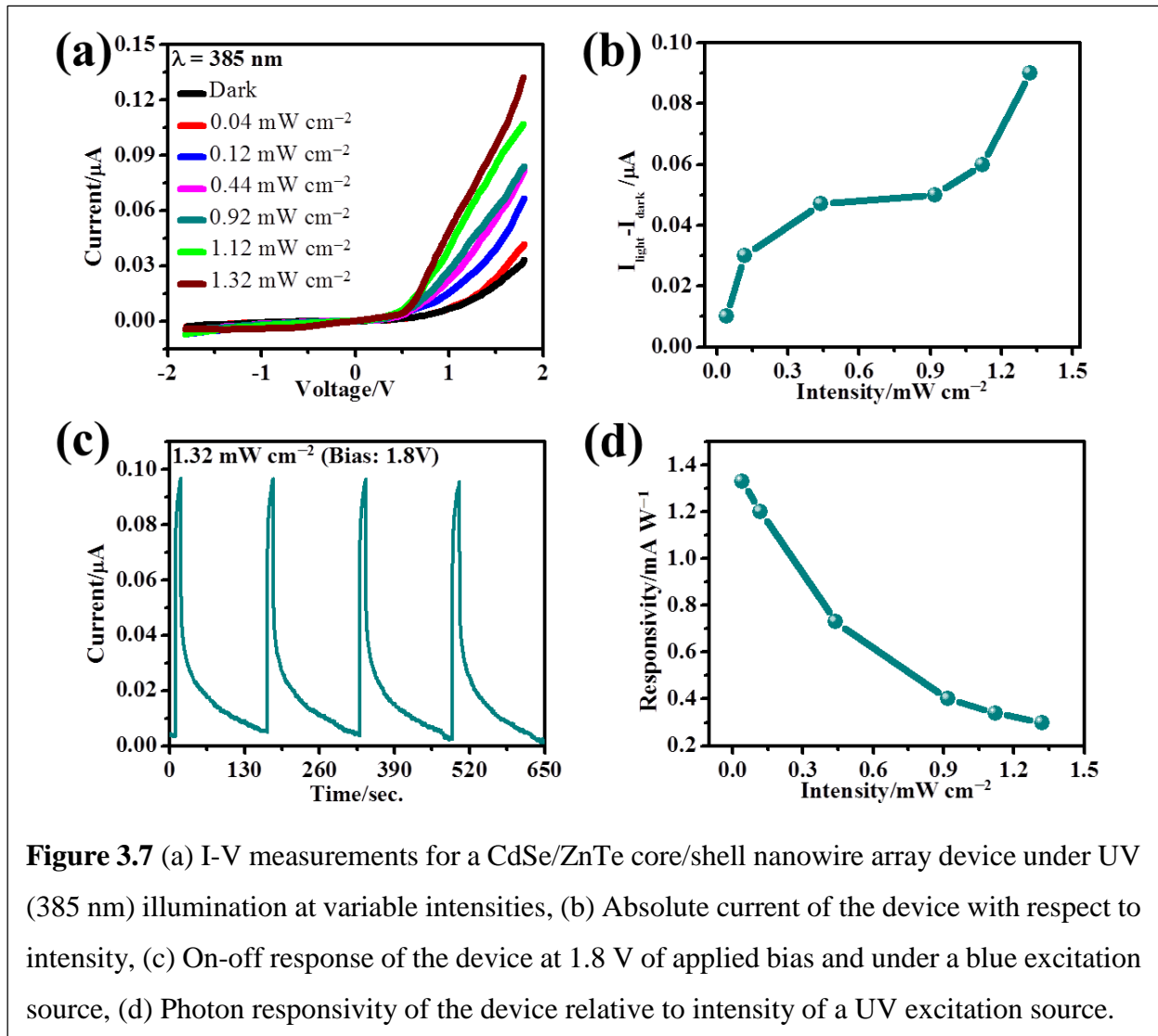


Figure 3.7 (a) I-V measurements for a CdSe/ZnTe core/shell nanowire array device under UV (385 nm) illumination at variable intensities, (b) Absolute current of the device with respect to intensity, (c) On-off response of the device at 1.8 V of applied bias and under a blue excitation source, (d) Photon responsivity of the device relative to intensity of a UV excitation source.

3.3.2.3 Piezo-phototronic Effect in CdSe/ZnTe Core/Shell Nanowire Array Photodetector

To further investigate the piezo-phototronic effect in the CdSe/ZnTe core/shell nanowire photodetector's performance, the device was subjected to compressive loads ranging from 0.05 to 0.30 kgf under blue, green and UV illumination. Figure 3.8 (a) displays the device I-V measurements under dark, blue ($\lambda = 465 \text{ nm}$), green ($\lambda = 520 \text{ nm}$) and UV ($\lambda = 385 \text{ nm}$) illumination without applied loads where current increases with increasing excitation frequency.

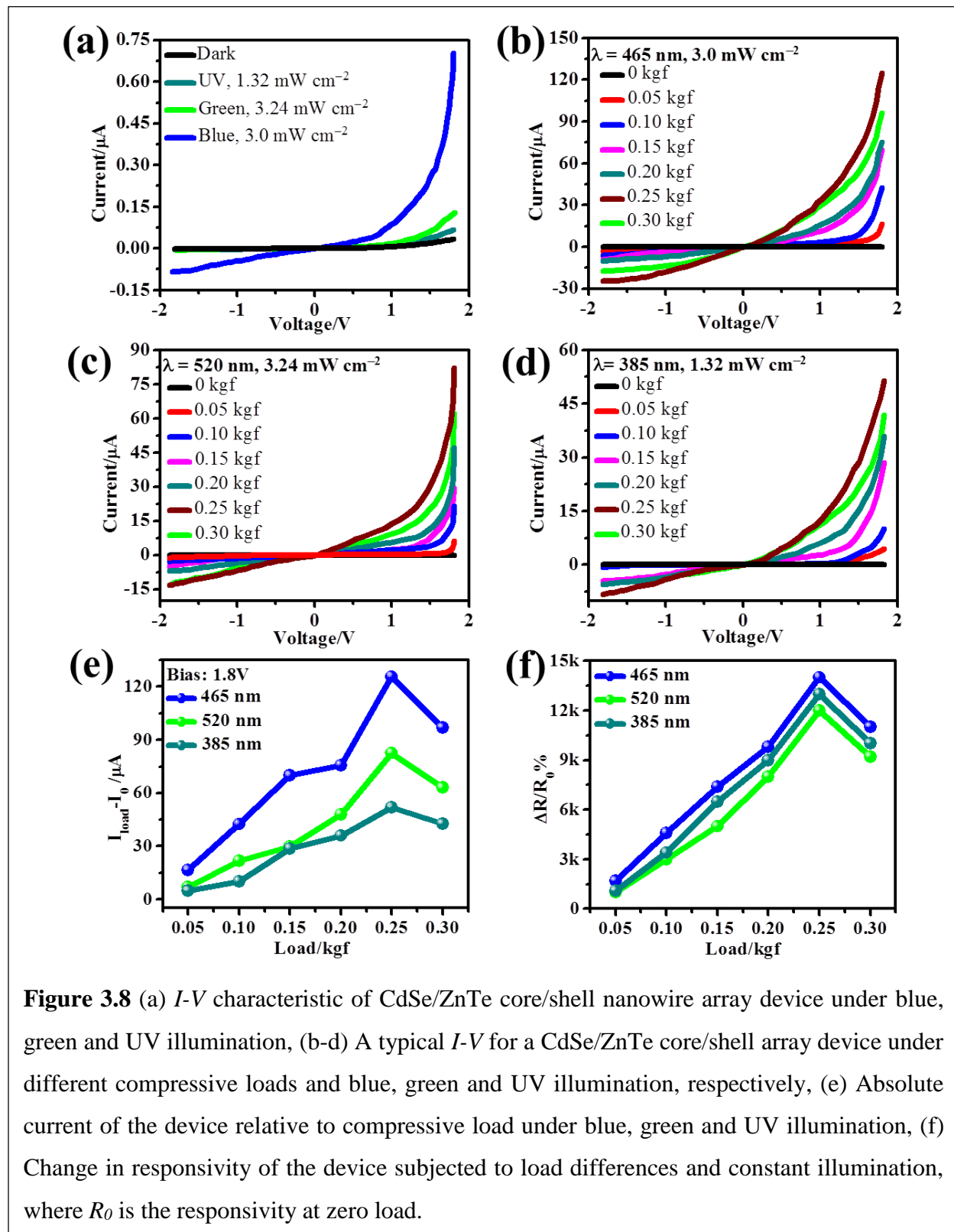


Figure 3.8 (b) represents the I - V measurements at different loads, e.g. from 0 to 0.3 kgf under blue illumination, and the observed peak current increases from 0.71 μ A without load to its maximum of 125 μ A at 0.25 kgf load, where a significant two orders of magnitude change can be observed. To investigate the performance of the device under a wide spectral range, similar I - V measurements were performed under green and UV light illumination with identical compressive loads (as the blue excitation source), which are shown in Figure 3.8 (c-d). The photocurrent reached its maximum value of 83 μ A (Figure 3.8 (c)) and 51 μ A (Figure 3.8 (d)) at 0.25 kgf compared to no load values of 0.18 μ A and 0.13 μ A (Figure 3.8 (a)) for green and UV illumination respectively. Generally, a sequential increment in photocurrent with increasing compressive loads from 0.05 to 0.25 kgf can also be seen. Figure 3.8 (e) is the variation of peak photocurrents relative to different compressive loads from 0.05 kgf to 0.30 kgf, representing an increasing tendency of the photocurrent until 0.25kgf. However, it was found that the photocurrents could not be further enhanced when compressive loads are over 0.25 kgf, as shown; photocurrents decreased once the load is 0.3 kgf. The I - V measurements were repeated for several cycles and showed reproducible results and steady performance. Therefore, structural degradation of the nanowire array as a source of the photocurrent decrease can be ruled out.

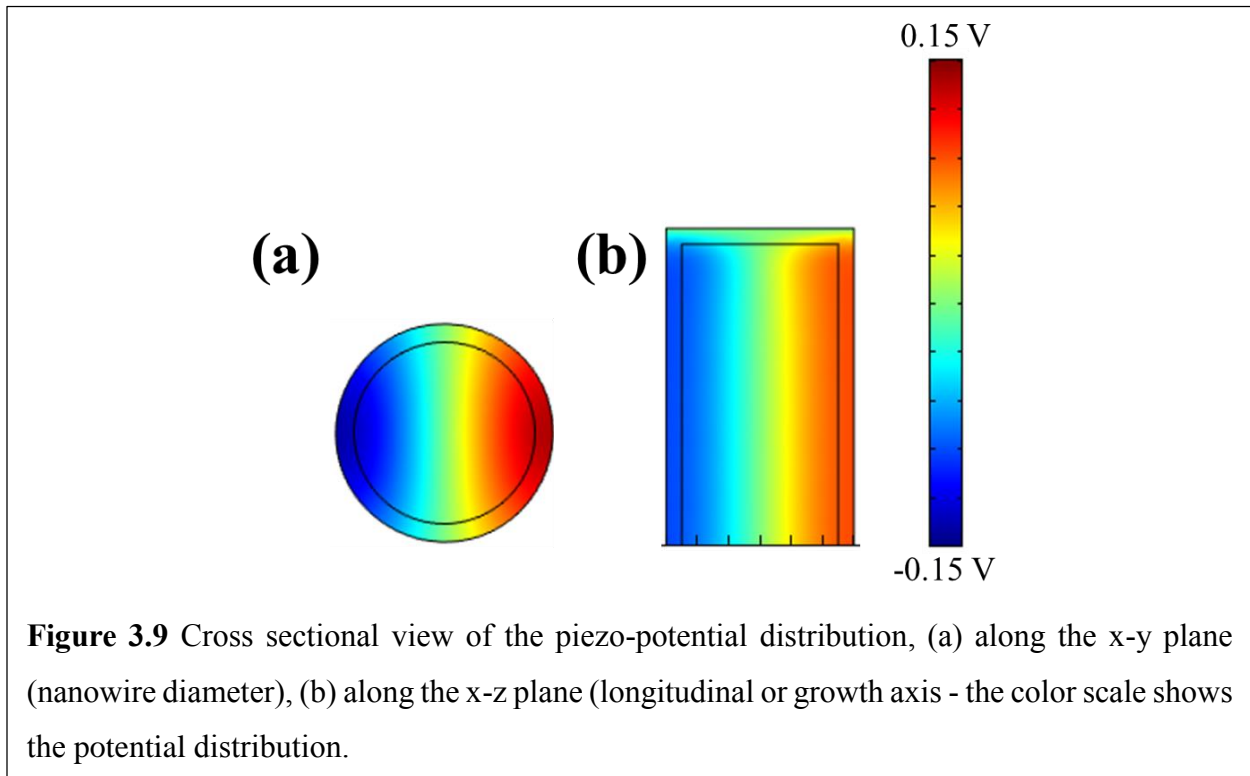
The reduced photocurrent is similar to the previously reported behavior of a single CdSe nanowire,²⁰ and can be explained by a theoretical model based on band bending at the CdSe/ZnTe interface under the influence of the piezo-potential, which will be discussed subsequently. The (%) change in responsivity ($\Delta R = (R_{\text{Load}} - R_0) / R_0 \times 100$) of the CdSe/ZnTe core/shell photodetector at compressive loads of 0.05 to 0.3 kgf is shown in Figure 3.8 (f) as well. The calculated (%) change in responsivity between illuminated samples with an applied load of 0.25 kgf and without an external load and under 1.8V bias results in a change of four orders of magnitude. The variation in

responsivity is remarkably high for this 3D, II-VI type-II core/shell nanowire array, which makes it an ideal candidate for a piezo-phototronic effect enhanced photodetector.

3.4 Working mechanism of piezo-phototronic photodetector

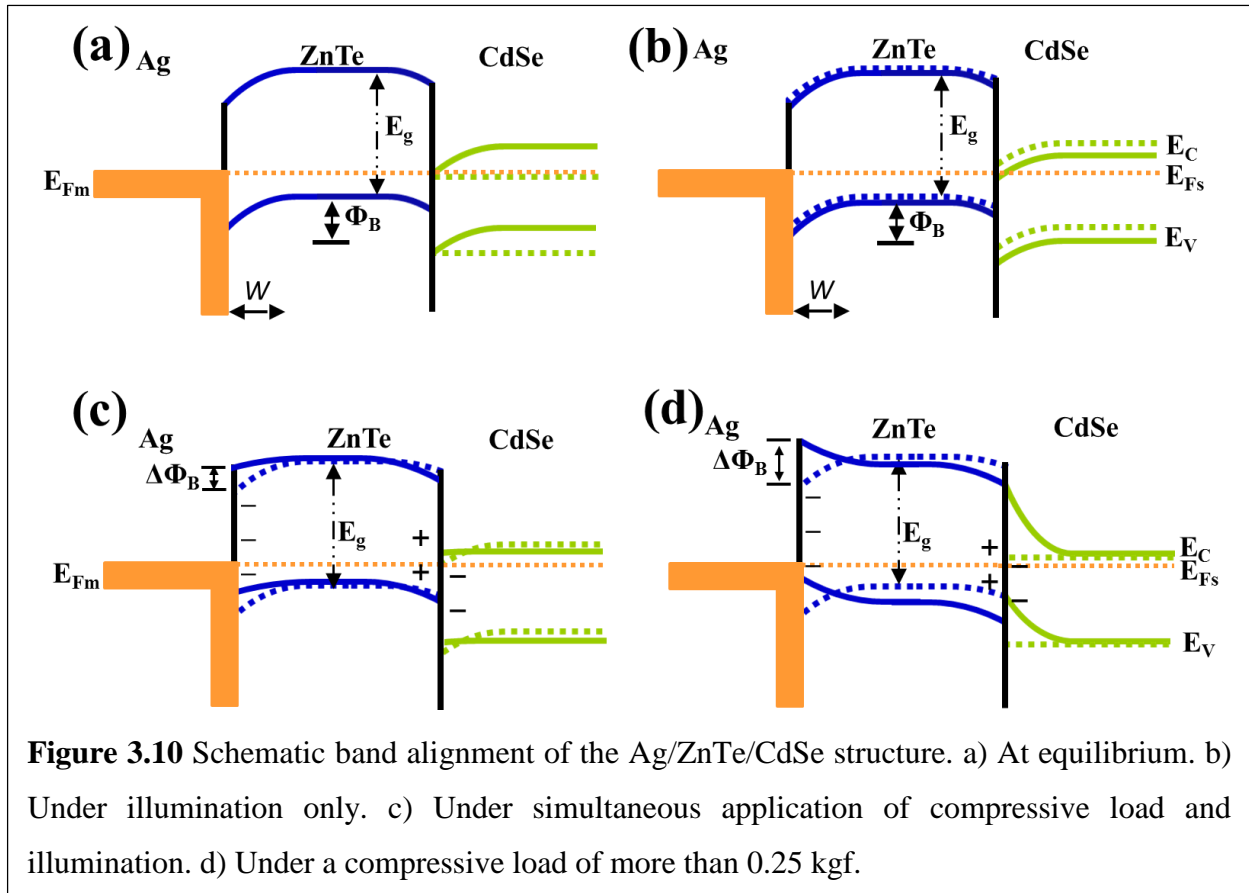
The improved photodetector performance under compressive load can be explained by a theoretical model based on the relative band alignment and its modification under the influence of piezopotential at the Ag-ZnTe and type-II, ZnTe/CdSe interfaces. As previously reported,¹⁰ a wurtzite CdSe nanowire undergoing lateral bending generates positive and negative piezopotential at the stretched (tensile) and compressed sides, respectively, of the nanowire surface.

Figure 3.9 (a) represents the COMSOL simulated piezo-potential distribution in cross sectional x-y plane perpendicular to z-axis (c-axis, growth direction) CdSe nanowire, whereas figure 3.9 (b) represents the piezo-potential distribution under same compressional load along x-z plane, which is longitudinal to c-axis of wurtzite CdSe crystal structure. Color code scheme



depicting the magnitude of piezopotential under external load represents the variation in magnitude of piezo-potential across x-y and x-z cross sectional plane which results in localization of electrons and holes in red and blue colored area in CdSe core and ZnTe shell, respectively. The charge carrier localization may partially screen the positive polarity piezo charges in CdSe core and negative polarity piezo charges in ZnTe shell, however the reverse polarity in each core and shell remains unaffected. This localized piezopotential then modifies the local Schottky barrier height at the Ag-ZnTe and ZnTe-CdSe interfaces, which controls the charge carrier transport and separation at the interface through the piezo-phototronic effect.

At equilibrium conditions, it is assumed that no net charge transfer takes place at the CdSe/ZnTe interface due to the staggered band alignment resulting from ZnTe's low-lying Fermi level, and a high electron transport barrier going from CdSe to ZnTe. When a Ag metal electrode is brought in contact with the ZnTe surface, a net diffusion current flows from ZnTe to the metal side resulting in ZnTe's Fermi level moving to lower energy; this also results into a lowering of the CdSe Fermi level (Figure 3.10 (a)).^{45,46} Once equilibrium is established, the majority diffusion current is retarded due to Schottky barrier created at the Ag-ZnTe interface. However, this barrier height can be tuned either by applying an external voltage or by modifying the inner piezopotential created in the non-centrosymmetric crystal structure under mechanical deformation, e.g. applying a load.



Upon illumination, the photo-generated electron-hole pairs momentarily shift the Fermi level slightly upwards for the thinner (~ 20 nm) ZnTe shell since ZnTe has a weak thickness-limited photo absorption compared to the thicker CdSe core, where moderate Fermi level lowering takes place due to greater absorption in the thicker (~ 200 nm), CdSe core (Figure 3.10 (b)). This Fermi level redistribution gives rise to photocurrent and, at fixed excitation wavelength, increases with increasing illumination density as observed in illumination density dependent I - V measurements (Figure 3.5, 3.6 and 3.7 (a)). When the nanowires are bent under an external load, the appearance of a positive piezopotential at the tensile surface reduces the Schottky barrier height (Figure 3.10 (c)) at the Ag-ZnTe interface, which leads to increased minority carrier diffusion electrons from ZnTe and holes from CdSe flow through the interface. The magnitude of the

piezopotential is dependent on the degree of mechanical deformation, therefore higher current flows at increased compressive loads.¹⁰ However, when the compressive strain is higher than a threshold value, which is 0.25 kgf in our system, it can raise the valence band edge of CdSe above ZnTe's valence band edge, as shown in Figure 3.10 (d), creating hole trapping states that lead to a decrease in the total current, as observed for 0.3 kgf load. The piezopotential lowering of the barrier height at the Ag-ZnTe interface and photo-excitation causing relative Fermi level redistribution create, in conjunction, a favorable situation for higher charge carrier injection between the Ag-ZnTe and ZnTe/CdSe interface (Figure 3.10 (d)) is created. It should be noted that unidirectional charge carrier injection, a combined effect of the piezopotential and photo-excitation, is greatly enhanced owing to the epitaxial nature of the CdSe/ZnTe interface, thereby resulting in higher peak current and a remarkably high responsivity change under simultaneous employment of load and illumination.

3.5 Conclusion

In summary, a broadband photodetector based on a type-II, epitaxially-grown CdSe/ZnTe heterojunction core/shell nanowire array has been successfully integrated. The epitaxial nature of the interface plays an important role as manifested by a high responsivity and significant sensitivity even at low illumination densities. The device performance is greatly enhanced by simultaneous application of compressive load and illumination owing to the piezo-phototronic effect. Two orders of magnitude change in the absolute current along with four orders of magnitude change in responsivity has been achieved, which is the highest increment observed so far. This investigation demonstrates the enhanced piezo-phototronic effect in a group II-VI, heterojunction, core/shell nanowire array fabricated as a photodetector.

References

1. (a) Wang, Z. L.; Wu, W., Piezotronics and piezo-phototronics—fundamentals and applications. *National Science Review* **2013**; (b) Wang, Z. L., Towards Self-Powered Nanosystems: From Nanogenerators to Nanopiezotronics. *Advanced Functional Materials* **2008**, *18* (22), 3553-3567.
2. Halasyamani, P. S.; Poeppelmeier, K. R., Noncentrosymmetric Oxides. *Chemistry of Materials* **1998**, *10* (10), 2753-2769.
3. Wang, Z. L.; Song, J., Piezoelectric Nanogenerators Based on Zinc Oxide Nanowire Arrays. *Science* **2006**, *312* (5771), 242-246.
4. Wang, X.; Song, J.; Liu, J.; Wang, Z. L., Direct-Current Nanogenerator Driven by Ultrasonic Waves. *Science* **2007**, *316* (5821), 102-105.
5. Wang, X.; Zhou, J.; Song, J.; Liu, J.; Xu, N.; Wang, Z. L., Piezoelectric Field Effect Transistor and Nanoforce Sensor Based on a Single ZnO Nanowire. *Nano Letters* **2006**, *6* (12), 2768-2772.
6. Hu, Y.; Chang, Y.; Fei, P.; Snyder, R. L.; Wang, Z. L., Designing the Electric Transport Characteristics of ZnO Micro/Nanowire Devices by Coupling Piezoelectric and Photoexcitation Effects. *ACS Nano* **2010**, *4* (2), 1234-1240.
7. Yang, Q.; Guo, X.; Wang, W.; Zhang, Y.; Xu, S.; Lien, D. H.; Wang, Z. L., Enhancing Sensitivity of a Single ZnO Micro-/Nanowire Photodetector by Piezo-phototronic Effect. *ACS Nano* **2010**, *4* (10), 6285-6291.
8. Zhang, Y.; Gao, G.; Chan, H. L. W.; Dai, J.; Wang, Y.; Hao, J., Piezo-Phototronic Effect-Induced Dual-Mode Light and Ultrasound Emissions from ZnS:Mn/PMN-PT Thin-Film Structures. *Advanced Materials* **2012**, *24* (13), 1729-1735.
9. Pan, C.; Dong, L.; Zhu, G.; Niu, S.; Yu, R.; Yang, Q.; Liu, Y.; Wang, Z. L., High-resolution electroluminescent imaging of pressure distribution using a piezoelectric nanowire LED array. *Nat Photon* **2013**, *7* (9), 752-758.

10. Gao, Y.; Wang, Z. L., Equilibrium Potential of Free Charge Carriers in a Bent Piezoelectric Semiconductive Nanowire. *Nano Letters* **2009**, *9* (3), 1103-1110.
11. Zhang, Y.; Wang; Mascarenhas, A., “Quantum Coaxial Cables” for Solar Energy Harvesting. *Nano Letters* **2007**, *7* (5), 1264-1269.
12. Pan, C.; Niu, S.; Ding, Y.; Dong, L.; Yu, R.; Liu, Y.; Zhu, G.; Wang, Z. L., Enhanced Cu₂S/CdS Coaxial Nanowire Solar Cells by Piezo-Phototronic Effect. *Nano Letters* **2012**, *12* (6), 3302-3307.
13. Boxberg, F.; Søndergaard, N.; Xu, H. Q., Photovoltaics with Piezoelectric Core–Shell Nanowires. *Nano Letters* **2010**, *10* (4), 1108-1112.
14. Schrier, J.; Demchenko, D. O.; Wang; Alivisatos, A. P., Optical Properties of ZnO/ZnS and ZnO/ZnTe Heterostructures for Photovoltaic Applications. *Nano Letters* **2007**, *7* (8), 2377-2382.
15. Wang, K.; Chen, J.; Zhou, W.; Zhang, Y.; Yan, Y.; Pern, J.; Mascarenhas, A., Direct Growth of Highly Mismatched Type II ZnO/ZnSe Core/Shell Nanowire Arrays on Transparent Conducting Oxide Substrates for Solar Cell Applications. *Advanced Materials* **2008**, *20* (17), 3248-3253.
16. Wang, K.; Chen, J. J.; Zeng, Z. M.; Tarr, J.; Zhou, W. L.; Zhang, Y.; Yan, Y. F.; Jiang, C. S.; Pern, J.; Mascarenhas, A., Synthesis and photovoltaic effect of vertically aligned ZnO/ZnS core/shell nanowire arrays. *Applied Physics Letters* **2010**, *96* (12), 123105.
17. Zhang, F.; Ding, Y.; Zhang, Y.; Zhang, X.; Wang, Z. L., Piezo-phototronic Effect Enhanced Visible and Ultraviolet Photodetection Using a ZnO–CdS Core–Shell Micro/nanowire. *ACS Nano* **2012**, *6* (10), 9229-9236.
18. Law, M.; Greene, L. E.; Johnson, J. C.; Saykally, R.; Yang, P., Nanowire dye-sensitized solar cells. *Nat Mater* **2005**, *4* (6), 455-459.
19. Wallentin, J.; Anttu, N.; Asoli, D.; Huffman, M.; Åberg, I.; Magnusson, M. H.; Siefer, G.; Fuss-Kailuweit, P.; Dimroth, F.; Witzigmann, B.; Xu, H. Q.; Samuelson, L.; Deppert, K.;

- Borgström, M. T., InP Nanowire Array Solar Cells Achieving 13.8% Efficiency by Exceeding the Ray Optics Limit. *Science* **2013**, 339 (6123), 1057-1060.
20. Zhang, F.; Niu, S.; Guo, W.; Zhu, G.; Liu, Y.; Zhang, X.; Wang, Z. L., Piezo-phototronic Effect Enhanced Visible/UV Photodetector of a Carbon-Fiber/ZnO-CdS Double-Shell Microwire. *ACS Nano* **2013**, 7 (5), 4537-4544.
21. Adachi, S., Optical Properties. In *Properties of Group-IV, III-V and II-VI Semiconductors*, John Wiley & Sons, Ltd: 2005; pp 211-281.
22. Liu, Z.; Chen, G.; Liang, B.; Yu, G.; Huang, H.; Chen, D.; Shen, G., Fabrication of high-quality ZnTe nanowires toward high-performance rigid/flexible visible-light photodetectors. *Optics Express* **2013**, 21 (6), 7799-7810.
23. Singh, A.; Li, X.; Protasenko, V.; Galantai, G.; Kuno, M.; Xing, H.; Jena, D., Polarization-Sensitive Nanowire Photodetectors Based on Solution-Synthesized CdSe Quantum-Wire Solids. *Nano Letters* **2007**, 7 (10), 2999-3006.
24. Zhang, L.; Shi, E.; Li, Z.; Li, P.; Jia, Y.; Ji, C.; Wei, J.; Wang, K.; Zhu, H.; Wu, D.; Cao, A., Wire-supported CdSe nanowire array photoelectrochemical solar cells. *Physical Chemistry Chemical Physics* **2012**, 14 (10), 3583-3588.
25. Löffler, T.; Hahn, T.; Thomson, M.; Jacob, F.; Roskos, H., Large-area electro-optic ZnTe terahertz emitters. *Optics Express* **2005**, 13 (14), 5353-5362.
26. He, Z.; Zhang, W.; Zhang, W.; Jie, J.; Luo, L.; Yuan, G.; Wang, J.; Wu, C. M. L.; Bello, I.; Lee, C.-S.; Lee, S.-T., High-Performance CdSe:In Nanowire Field-Effect Transistors Based on Top-Gate Configuration with High- κ Non-Oxide Dielectrics. *The Journal of Physical Chemistry C* **2010**, 114 (10), 4663-4668.
27. Khandelwal, A.; Jena, D.; Grebinski, J.; Hull, K.; Kuno, M., Ultrathin CdSe nanowire field-effect transistors. *Journal of Elec Materi* **2006**, 35 (1), 170-172.

28. Zhang, J.; Chen, P.-C.; Shen, G.; He, J.; Kumbhar, A.; Zhou, C.; Fang, J., p-Type Field-Effect Transistors of Single-Crystal Zinc Telluride Nanobelts. *Angewandte Chemie International Edition* **2008**, *47* (49), 9469-9471.
29. Li, G.; Zhai, T.; Jiang, Y.; Bando, Y.; Golberg, D., Enhanced Field-Emission and Red Lasing of Ordered CdSe Nanowire Branched Arrays. *The Journal of Physical Chemistry C* **2011**, *115* (19), 9740-9745.
30. Wang, K.; Rai, S. C.; Marmon, J.; Chen, J.; Yao, K.; Wozny, S.; Cao, B.; Yan, Y.; Zhang, Y.; Zhou, W., Nearly lattice matched all wurtzite CdSe/ZnTe type II core-shell nanowires with epitaxial interfaces for photovoltaics. *Nanoscale* **2014**, *6* (7), 3679-3685.
31. Zhou, Y. S.; Wang, K.; Han, W.; Rai, S. C.; Zhang, Y.; Ding, Y.; Pan, C.; Zhang, F.; Zhou, W.; Wang, Z. L., Vertically Aligned CdSe Nanowire Arrays for Energy Harvesting and Piezotronic Devices. *ACS Nano* **2012**, *6* (7), 6478-6482.
32. Dong, L.; Niu, S.; Pan, C.; Yu, R.; Zhang, Y.; Wang, Z. L., Piezo-Phototronic Effect of CdSe Nanowires. *Advanced Materials* **2012**, *24* (40), 5470-5475.
33. Utama, M. I. B.; Peng, Z.; Chen, R.; Peng, B.; Xu, X.; Dong, Y.; Wong, L. M.; Wang, S.; Sun, H.; Xiong, Q., Vertically Aligned Cadmium Chalcogenide Nanowire Arrays on Muscovite Mica: A Demonstration of Epitaxial Growth Strategy. *Nano Letters* **2010**, *11* (8), 3051-3057.
34. Wang, X.; Song, W.; Liu, B.; Chen, G.; Chen, D.; Zhou, C.; Shen, G., High-Performance Organic-Inorganic Hybrid Photodetectors Based on P3HT:CdSe Nanowire Heterojunctions on Rigid and Flexible Substrates. *Advanced Functional Materials* **2013**, *23* (9), 1202-1209.
35. Debgupta, J.; Devarapalli, R.; Rahman, S.; Shelke, M. V.; Pillai, V. K., Electrochemical preparation of vertically aligned, hollow CdSe nanotubes and their p-n junction hybrids with electrodeposited Cu₂O. *Nanoscale* **2014**, *6* (15), 9148-9156.
36. Cao, Y. L.; Liu, Z. T.; Chen, L. M.; Tang, Y. B.; Luo, L. B.; Jie, J. S.; Zhang, W. J.; Lee, S. T.; Lee, C. S., Single-crystalline ZnTe nanowires for application as high-performance Green/Ultraviolet photodetector. *Optics Express* **2011**, *19* (7), 6100-6108.

37. Katz, O.; Bahir, G.; Salzman, J., Persistent photocurrent and surface trapping in GaN Schottky ultraviolet detectors. *Applied Physics Letters* **2004**, *84* (20), 4092-4094.
38. Soci, C.; Zhang, A.; Xiang, B.; Dayeh, S. A.; Aplin, D. P. R.; Park, J.; Bao, X. Y.; Lo, Y. H.; Wang, D., ZnO Nanowire UV Photodetectors with High Internal Gain. *Nano Letters* **2007**, *7* (4), 1003-1009.
39. Demichel, O.; Heiss, M.; Bleuse, J.; Mariette, H.; Fontcuberta i Morral, A., Impact of surfaces on the optical properties of GaAs nanowires. *Applied Physics Letters* **2010**, *97*, 201907.
40. Gallo, E. M.; Chen, G.; Currie, M.; McGuckin, T.; Prete, P.; Lovergine, N.; Nabet, B.; Spanier, J. E., Picosecond response times in GaAs/AlGaAs core/shell nanowire-based photodetectors. *Applied Physics Letters* **2011**, *98*, 241113
41. Liu, Y.; Yang, Q.; Zhang, Y.; Yang, Z.; Wang, Z. L., Nanowire Piezo-phototronic Photodetector: Theory and Experimental Design. *Advanced Materials* **2012**, *24* (11), 1410-1417.
42. Zhu, H.; Shan, C. X.; Yao, B.; Li, B. H.; Zhang, J. Y.; Zhao, D. X.; Shen, D. Z.; Fan, X. W., High Spectrum Selectivity Ultraviolet Photodetector Fabricated from an n-ZnO/p-GaN Heterojunction. *The Journal of Physical Chemistry C* **2008**, *112* (51), 20546-20548.
43. Ni, P.-N.; Shan, C.-X.; Wang, S.-P.; Liu, X.-Y.; Shen, D.-Z., Self-powered spectrum-selective photodetectors fabricated from n-ZnO/p-NiO core-shell nanowire arrays. *Journal of Materials Chemistry C* **2013**, *1* (29), 4445-4449.
44. Qin, L.; Shao, D.; Shing, C.; Sawyer, S., Wavelength selective p-GaN/ZnO colloidal nanoparticle heterojunction photodiode. *Applied Physics Letters* **2013**, *102* (7), -.
45. Feng, X.; Zhang, Y.; Wang, Z., Theoretical study of piezotronic heterojunction. *Sci. China Technol. Sci.* **2013**, *56* (11), 2615-2621.
46. Wu, W.; Pan, C.; Zhang, Y.; Wen, X.; Wang, Z. L., Piezotronics and piezo-phototronics – From single nanodevices to array of devices and then to integrated functional system. *Nano Today* **2013**, *8* (6), 619-642.

Chapter 4 Piezo-phototronic photodetector based on fully wide band gap type-II core/shell nanowire array

4.1 Introduction

Piezo-phototronic effect, a word coined in 2010,¹ arises from the coupling of semiconducting, optical and piezoelectric properties which can play a crucial role in the ability to tune/control charge carrier generation, separation, transport and/or recombination at an interface/junction.² The inner piezopotential, generated due to strain in non-centrosymmetric wurtzite semiconducting crystal, is the underlying mechanism resulting in improved performance of optoelectronic devices, provided that the material selection/combination and device design can enable the coupling in a favorable manner.³ This concept was first demonstrated successfully in a single ZnO micro-/nanowire based ultraviolet (UV) photodetector⁴ to increase the responsivity of the device by more than 500% under nominal (-0.36%) uniaxial compressive strain. In spite of excellent semiconducting and piezoelectric properties, application of ZnO as a photodetector is limited to the UV region only owing to its wide band gap ($E_g \sim 3.2$ eV). Therefore, for more practical ZnO based piezo-phototronic photo sensing devices, it is critical to overcome the restriction imposed by the wide band gap which can be done by forming a heterostructure, more specifically, a core/shell structure, to achieve sufficient photo absorption in a broader spectral region.

**This chapter is adapted from: Satish C. Rai, Kai Wang, Jiajun Chen, Manish Bhatt, Weilie Zhou, “An UV/Visible Piezo-phototronic Photodetector Based on Truly Wide Band Gap ZnO/ZnS Core/Shell Nanowire Array”, ACS Nano, 2015, 9 (6), pp 6419–6427.*

This strategy does not only allow the efficient use of intrinsic materials properties of individual components, but also improves the charge carrier collection favored by radial geometry where electrons and holes are spatially confined in different conducting channels particularly in type-II heterostructures,^{5,6} resulting in reduced recombination losses.⁷⁻⁹ One such device based on single ZnO/CdS core/shell micro/nanowire¹⁰ extends the photodetection to visible region in which uniaxial compressive strain can further improve device performance. These promising attributes of core/shell nanowires can be further augmented in three dimensional arrays where photo absorption is enhanced by the trapping and re-scattering of incident photons.¹¹ Additionally, in nanowire arrays simultaneous multi-channel charge transport facilitates efficient collection of photo generated electron-hole pairs thereby leading to improved quantum efficiency^{12,13} which, when combined with piezo-phototronic effect opens up new avenues for achieving largely enhanced device performance.¹⁴ These features of three dimensional core/shell nanowire arrays have been successfully employed in realizing the UV/visible photodetector based on carbon fiber/ZnO/CdS double shell microwire¹⁵ and recently, in optical-fiber-nanowire hybrid structure¹⁶ suggesting that three dimensional core/shell nanowire arrays are a very promising candidate for piezo-phototronic device applications.

As an important piezoelectric semiconductor, ZnO has been extensively investigated for application in nanogenerators,^{17,18} electroluminescent¹⁹ and self-powered sensing devices,^{20,21} proving its adaptability to various applications. It has also been reported that ZnO nanowire can serve as a template to grow a nearly epitaxial ZnS shell layer with an abrupt interface, forming type-II heterojunction.²² An earlier work, based on band-corrected pseudopotential density functional theory calculation,²³ reports an indirect band gap of ~2.07 eV for type-II transition in ZnO/ZnS core/shell nanowires corresponding to Shockley-Quiesser efficiency limit of 23%, which

implies its potential towards photosensing device applications. In spite of numerous synthesis efforts for ZnO/ZnS heterostructure formations,²⁴⁻²⁹ and theoretical predictions about sufficient photo absorption²³ as required by photo sensing devices, so far, a prototype photosensing device based on three dimensional ZnO/ZnS core/shell nanowire array is still lacking. In present work, we demonstrate an efficient and highly sensitive broad band UV/Visible photodetector based on fully wide band gap, three dimensional (3D) ZnO/ZnS core/shell nanowire array in which the type-II transition plays a crucial role. More importantly, the device efficiency can be further improved, at least, by an order of magnitude rendering three orders of increase in relative responsivity by piezo-phototronic effect.³⁰

4.2 Experimental

Synthesis of ZnO/ZnS core/shell nanowire array was done *via* a two-step process. Firstly, ZnO nanowire array was grown on SiO₂ passivated ITO/glass (CG80IN, Delta Technologies LTD) substrate by chemical vapor deposition. Secondly, as grown ZnO nanowire array on ITO/glass substrate was transferred into a home built pulsed laser deposition system. Figure 3.1 represents the detailed schematics of the two step synthetic process involving CDV and PLD.

4.2.1 CVD growth of ZnO nanowire array on ITO/glass substrate

ZnO nanowire array was synthesized on SiO₂ passivated indium tin oxide (ITO) coated glass substrate by thermal evaporation of Zn powder (99.9%, metals basis, Alfa Aesar) in a three zone quartz tube furnace (GSL-1400X, MTI Corp). Initially, 10×10 mm ITO/glass substrate were cleaned by immersing in acetone, isopropyl alcohol (IPA) and deionized water (DI) each for 60 seconds in ultrasonic bath in the order of acetone/IPA/DI water. Substrates were taken out of the ultrasonic bath and were washed by copious amounts of flowing DI water followed by blow drying under Nitrogen (N₂). This standard substrate cleaning procedure is critical in order to remove dusts,

lint and grease deposited on it and to facilitate more uniform nanowire coverage on larger areas. Freshly prepared 15 mM seed solution of zinc acetate dehydrate ($\text{Zn}(\text{CH}_3\text{COO})_2 \cdot 2\text{H}_2\text{O}$) in DI water was drop casted on the conductive side and blow dried by Nitrogen (N_2). This process was repeated several time in order to ensure uniform coverage of seed solution followed by air heating at $500\text{ }^\circ\text{C}$ to convert $\text{Zn}(\text{CH}_3\text{COO})_2 \cdot 2\text{H}_2\text{O}$ into ZnO seeds. 4g of Zn powder was loaded in alumina crucible and positioned at the center of the three zone tube furnace. The SiO_2 passivated ITO/glass substrate was positioned at 25 cm downstream in the second zone of the furnace. The substrate distance from the central zone is crucial to achieve optimum density, length and diameter of ZnO nanowires. Quartz tube was evacuated to 30 mTorr using rough pump and was back filled by pure Ar and the process was repeated several time to eliminate residual gases from the tube. The temperatures of the first and second zones were ramped to $900\text{ }^\circ\text{C}$ and $550\text{ }^\circ\text{C}$ under 350 standard cubic centimeter (sccm) Ar/ O_2 (6:1) flow for a total reaction time of 1 hour and tube pressure was maintained at 50 mTorr by controlling the pumping rate. After reaction was complete, the furnace was cooled down to room temperature naturally and ZnO nanowires were formed in a white layer on ITO substrate.

4.2.2 ZnO/ZnS core/shell nanowire array by PLD

In order to synthesize ZnO/ZnS core/shell nanowire array, the ITO substrate with ZnO nanowire array was transferred to a home built pulsed laser deposition system (PLD) as described previously.⁸ Briefly, a ZnS target (99.99%, Kurt. J. Lesker) prepared by cold pressing was loaded upright in alumina crucible and positioned in the middle of the furnace (Lindberg/Blue M™ Mini-Mite™) and tube was evacuated to 30 mTorr base pressure using rough pump. The temperature of the furnace was ramped up to $500\text{ }^\circ\text{C}$ and was maintained during ablation process. Nd:YAG laser (LOTIS TII-LS 2147) was used to ablate the ZnS target. The laser wavelength, energy density

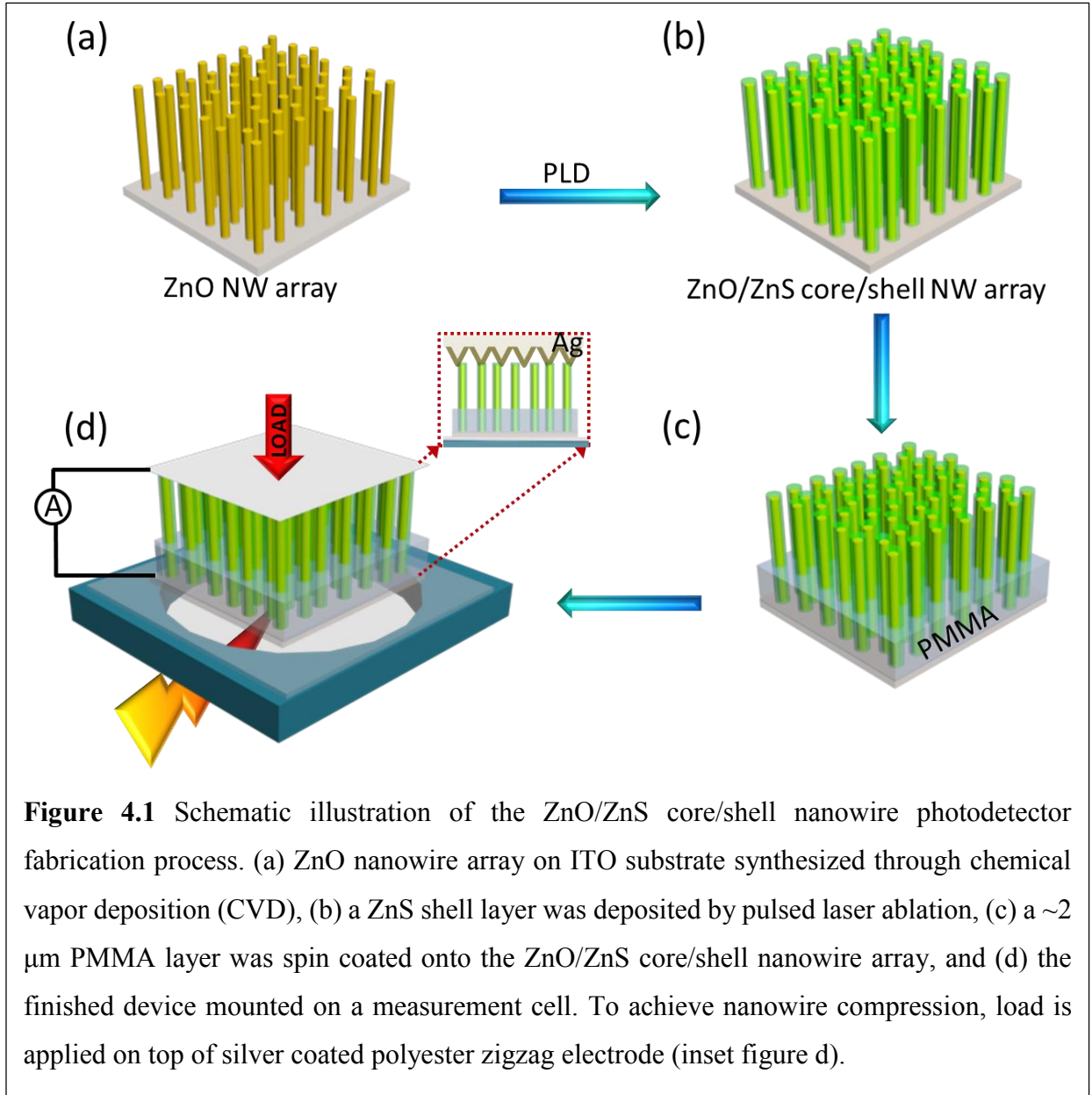
and ablation frequency were 1064 nm, 30 mJ/cm² and 2Hz to achieve optimum coating thickness and uniform shell layer coverage. ZnO nanowire on ITO substrate was positioned 3 cm away from the target and ablation was performed for 20 minutes at 30 mTorr base pressure.

4.2.3 Materials characterization

Structural and morphological characterizations were carried out with HITACHI Su8010 field-emission scanning electron microscope (FESEM), and a FEI Tecnai G2 F30 ST high-resolution transmission electron microscope (HRTEM) equipped with a nanoprobe energy-dispersive (EDS) X-ray spectroscope. Additional details of optical and structural characterizations can be found in a previously published literature.²² Room temperature photoluminescence (PL) measurements were measured by a Horiba LabRAM HR800 confocal Raman system with a Synapse charge-coupled detector (CCD). A 100x MPLAN objective lens (NA = 0.9) were used for 532 and 442 nm excitation, and a 50x UV objective lens (NA = 0.55) was used for 325nm excitation. Laser powers were 148.2, 151.7, and 139.6 μ W, respectively. Background measurements of the substrate were subtracted from all spectra.

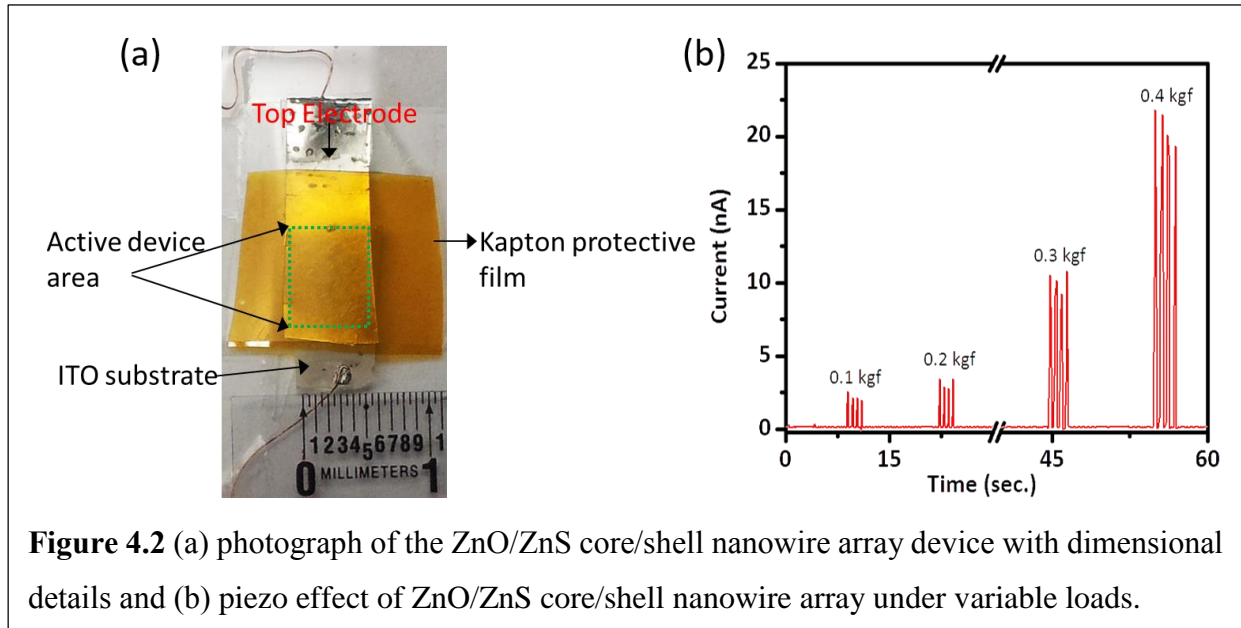
4.2.4 Device fabrication and measurements

A 3D photodetector was integrated on ZnO/ZnS core/shell nanowire array by positioning the Ag/polyester zigzag electrode on top of the nanowire array for the contact formation at the nanowire tips only and to ensure optimal compression under applied load (inset in Figure 4.1 (d)).¹⁸ Figure 4.1 represents a schematic pictorial flow of the complete device integration steps. As synthesized ZnO/ZnS core/shell nanowire array on ITO substrate was spin coated by a thin layer of PMMA followed by O₂ plasma etching for a few minutes. For zigzag top electrode fabrication polyester grating (12700 lines/inch, Edmund Optics) was sputter coated with 30 nm silver (Ag) and positioned on top of the nanowire array. ITO substrate and zigzag/Ag film were connected by



copper leads using silver paste. The electrical measurements were carried out using low noise current pre-amplifier (SR-570, Stanford Research Systems), and a source meter (Keithley-2401) coupled with a computer interface. A typical device photograph is shown in (Figure 4.2 (a)) with total active device area of 30 mm^2 which was used to calculate the responsivity. In order to confirm that piezoelectric property of wurtzite ZnO is unaffected by zinc blend ZnS shell layer deposition, a current *versus* time (I - T) measurement of the ZnO/ZnS core/shell nanowire array under cyclic

strain both in dark and in the absence of any external bias was performed. Figure 4.2 (b) represents the result of a typical I - T measurement where peak piezo-current exhibits an increase as the load increases, which is in accordance with earlier report.³¹



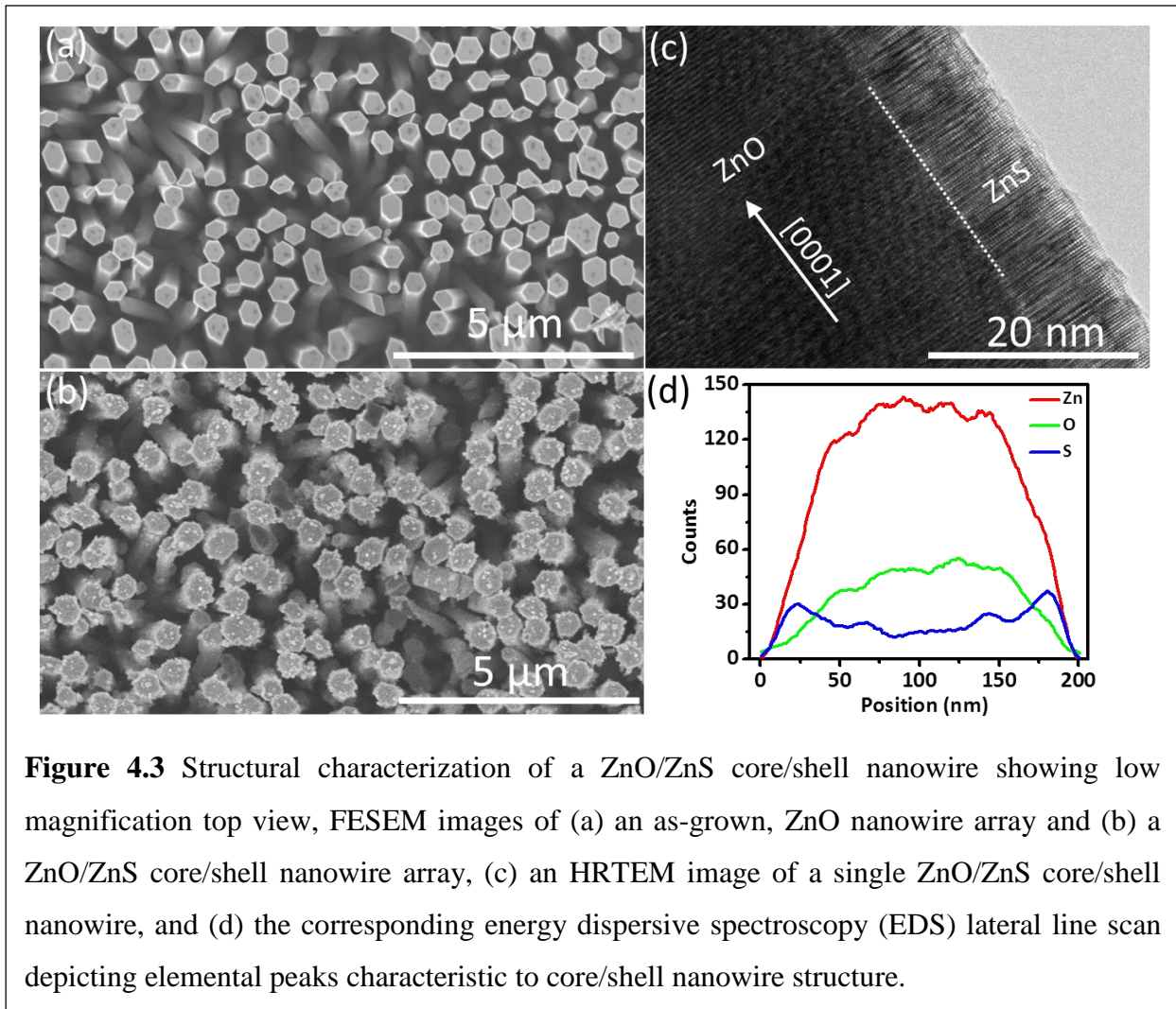
Additionally, to eliminate that contact change can achieve better device performance, control measurements were performed before actual piezo-phototronic measurements were carried out. The resistance of the device was measured after packing as well as under different load conditions. For a typical device it was found that resistance varies from ~ 300 k Ω at no load condition to ~ 180 k Ω at a maximum of 0.4 kgf. Previous studies done on similar nanowire arrays predicts that at a fixed external forward bias,^{18,32} the peak current is inversely proportional to the total resistance given by $R_c + R_i$, where R_c is contact induced and R_i is internal resistance of the nanowire array. Assuming, that all the nanowires are in contact with top electrode at maximal compression, at fixed bias the total increase in current due to change in total resistance is expected to be two times whereas in our case the overall increase of the current is ~ 31 times. Based on these

measurements, we can conclude that improved performance of the device is dictated by piezo-phototronic effect rather than contact change.

4.3 Results and Discussion

4.3.1 Structure characterization

Figure 4.3 represents the structural characterization of a ZnO/ZnS core/shell nanowire array, where Figure 4.3 (a) and (b) are top views low magnification field emission scanning electron microscope (FESEM) images of the as-grown ZnO nanowire array and a ZnO/ZnS core/shell nanowire array on indium tin oxide coated (ITO) glass substrate.⁸



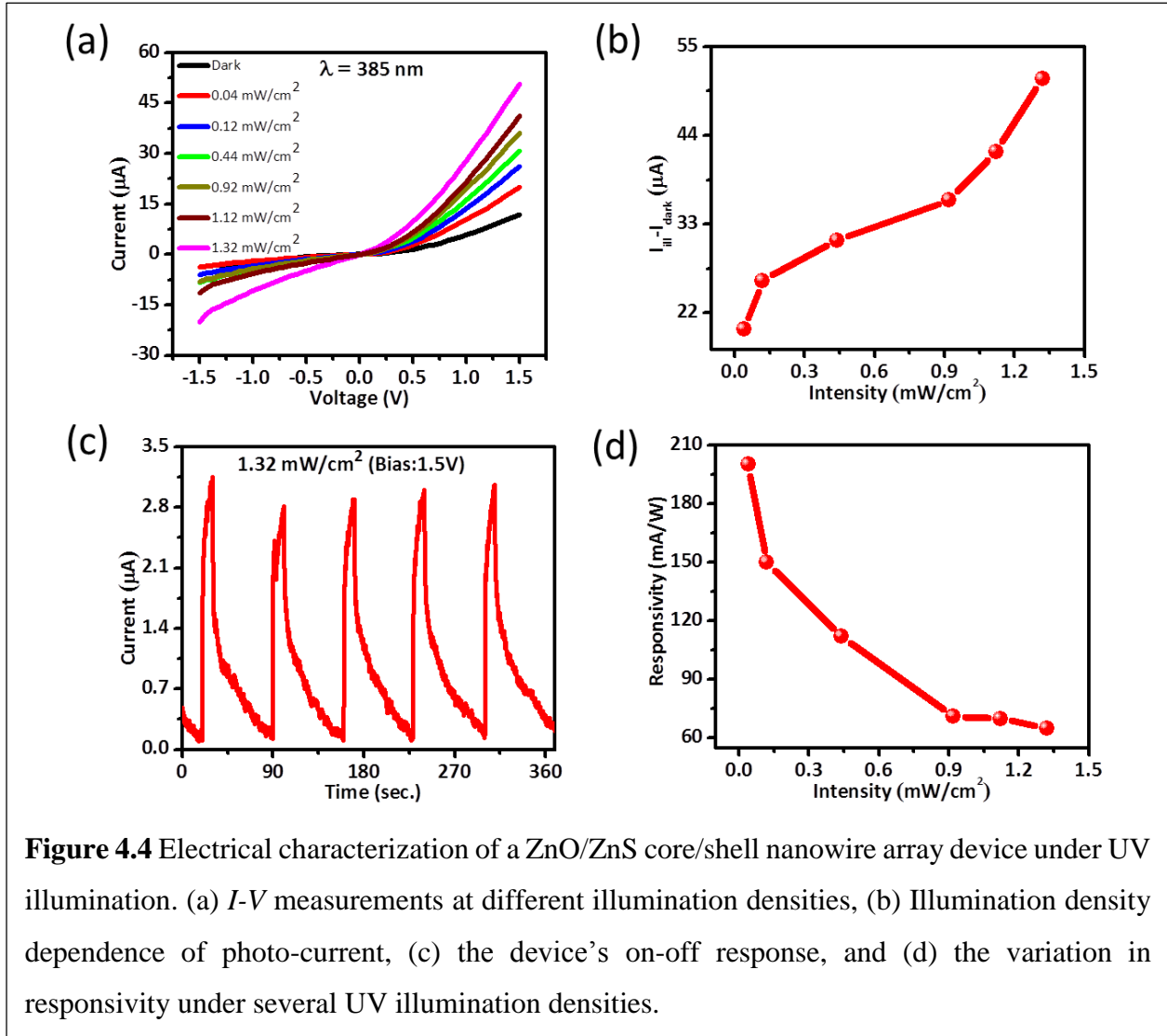
Rational density and smooth surface ZnO nanowires, with lengths and diameters in the range of 5~6 μm and 150~200 nm, respectively, can be seen in Figure 4.3 (a), whereas a slightly rough surface and increased diameter, with few ZnS particulates deposited on the tips, is observed in Figure 4.3 (b) for the core/shell nanowires. A high resolution transmission electron microscope (HRTEM) image of a typical single ZnO/ZnS core/shell nanowire is displayed in Figure 4.3 (c) where two different lattice fringes, corresponding to the zinc-blend ZnS shell and wurtzite ZnO core separated by an abrupt interface can be seen, which is similar to the previously reported work.²² Furthermore, Figure 4.3 (d) illustrates an energy dispersive (EDS) line scan collected along the lateral direction of a core/shell nanowire, which shows the characteristic core/shell elemental distribution further confirming the successful synthesis of ZnO/ZnS core/shell nanowires.^{33,34}

4.3.2 ZnO/ZnS core/shell nanowire array photodetector

4.3.2.1 Photodetector under UV illumination

A typical I - V measurement of the photodetector integrated on 3D ZnO/ZnS core/shell nanowire array under a UV (385 nm) excitation source is displayed in Figure 4.4. It can be seen that the photocurrent increases, Figure 4.4 (a), with an increase in the UV illumination density resulting from the higher intensity influenced increment in the generation rate (G) of electron-hole pairs, within the limit of $h\nu > E_g$ and defined by $G = \alpha F(1-R)e^{-\alpha x}$ where, α is the absorption coefficient, R is the surface reflectivity, and F is the incident photon flux.³⁵ Under steady state illumination at a fixed wavelength, the generation rate is solely determined by incident photon flux density (F), where an increase in F will improve the electron-hole pair generation rate. Since $E_{g, \text{ZnS}} (3.7 \text{ eV}) > E_{385 \text{ nm}} (3.22 \text{ eV}) \approx E_{g, \text{ZnO}} (3.2 \text{ eV})$, the excitation wavelength used only matches ZnO optical band gap, and it is reasonable to assume that the photocurrent contribution from the electron-hole pairs predominantly arise from photo absorption taking place in the ZnO core in a core/shell nanowire. In addition to band-to-band absorption in ZnO, the contribution from

simultaneous indirect type-II transitions occurring between the valence band maxima of the ZnS_{VBM} to the conduction band minima of the ZnO_{CBM} has to be considered, and its effect on device performance will be discussed in details to follow.



Variation in photocurrent with illumination intensity is plotted in Figure 4.4 (b), where an increase of 325% in photocurrent ($\sim 51 \mu\text{A}$), at an intensity of 1.32 mW/cm^2 can be seen as compared to the ($\sim 12 \mu\text{A}$) dark current. Time-dependent photocurrent measurement at a power density of 1.32 mW/cm^2 and bias of 1.5V is shown in Figure 4.4 (c), which suggests stable device

switching behavior. The performance of a practical photodetector is also characterized by its responsivity (R_λ) at a particular wavelength, which is an important parameter that is defined as¹⁴

$$R_\lambda = \frac{I_{light} - I_{dark}}{P_{ill}}$$

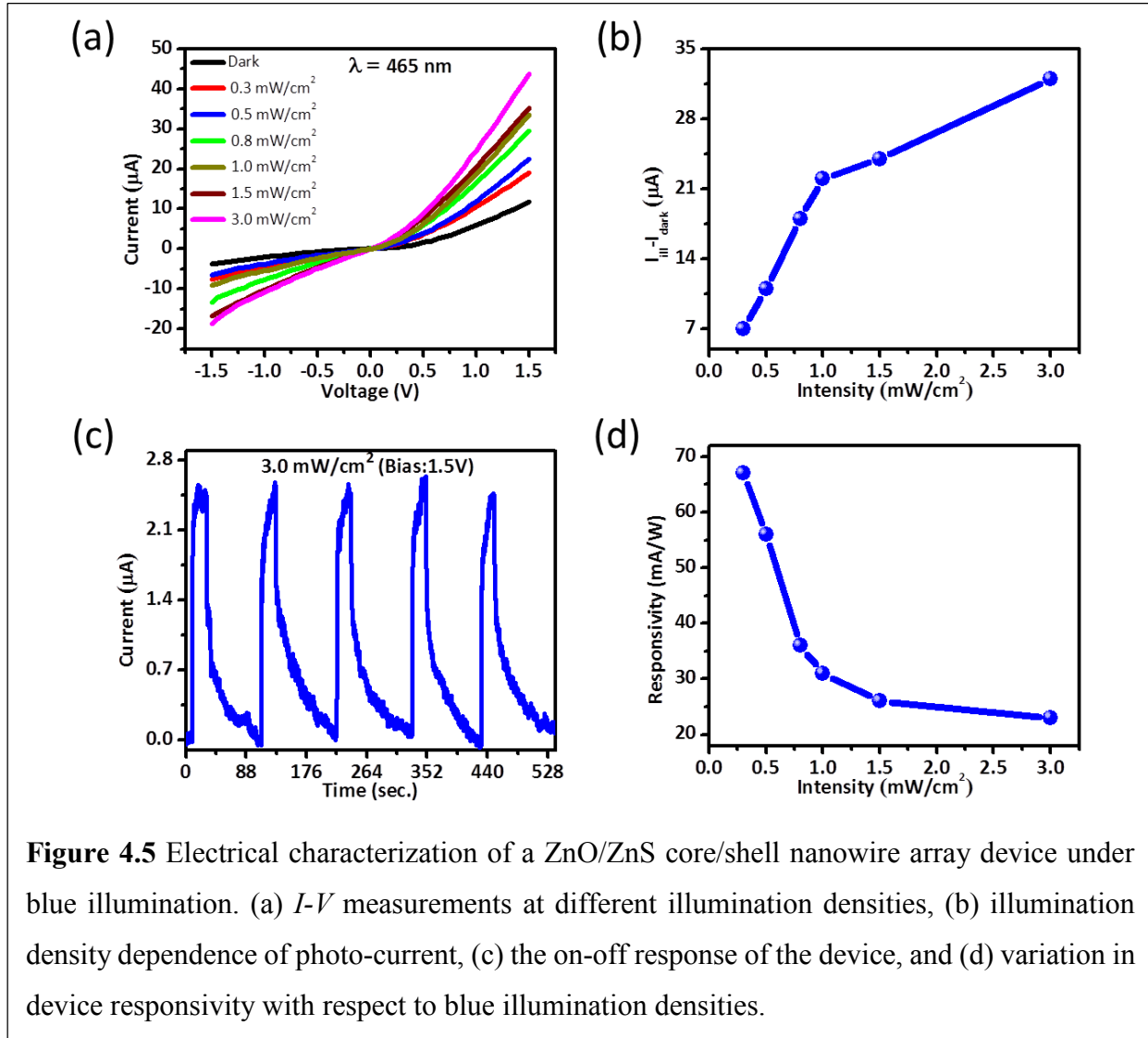
$$P_{ill} = I_{ill} \cdot A$$

where I_{light} , and I_{dark} , are currents when the photodetector is under illumination and in the dark, respectively. P_{ill} , I_{ill} , and A are the excitation power, illumination density, and the active/illuminated device area, respectively. The responsivity for UV (385 nm) excitation source, denoted as R_{385nm} , with a 0.04 mW/cm² illumination density was found to be 0.2 A/W, which is similar to a single crystal ZnS nanobelt UV sensor,³⁶ and is orders of magnitude higher than similar photodetectors fabricated with a 3D array of nanowires.³²⁻⁴¹ This responsivity value corresponds to an external quantum efficiency (EQE) of about 65% if the internal photoconductive gain is assumed to be one.⁴² The high responsivity achieved in the ZnO/ZnS core/shell nanowire array device can mainly be attributed to the abrupt nature of the interface between ZnO and ZnS, which effectively inhibits carrier recombination and facilitates an efficient carrier separation.

4.3.2.2 Photodetector under blue and green illumination

The performance of the ZnO/ZnS core/shell nanowire array photodetector was also investigated under blue (465 nm) and green (520 nm) excitation source, and the results are summarized in Figure 4.5 and 4.6, respectively. It should be noted that the photon energy corresponding to blue (2.66 eV) and green (2.38 eV) wavelengths are significantly lower than those needed to promote direct band-to-band absorption in ZnO ($E_g \sim 3.2$ eV)⁴³ and ZnS ($E_g \sim 3.7$ eV), which leads us to believe that the photocurrent response must be arising from an indirect type-

II transition of electrons between the ZnS_{VBM} (shell) and ZnO_{CBM} (core). Remarkably, the photodetector response exhibits a similar behavior, as observed for UV (385 nm) excitation source (Figure 4.4).



The peak photocurrents under blue and green excitations reached $\sim 44 \mu\text{A}$ ($3 \text{ mW}/\text{cm}^2$, Figure 4.5 (a)) and $\sim 18 \mu\text{A}$ ($3.2 \text{ mW}/\text{cm}^2$, Figure 4.6 (a)), respectively, which correspond to an increase of 267% for blue and 50% for green wavelength as compared to the $\sim 12 \mu\text{A}$ dark current. The photocurrent variation plot, with illumination intensities (Figure 4.5-4.6 (b)) and time dependence (Figure 4.5-4.6 (c)), shows electron-hole pair generation rate dependent linear increase

of photocurrents in addition to fast and stable response as seen from the switching behavior of the device. Figure 4.5-4.6 (d) contains responsivity vs. intensity plots of the photodetector under blue and green illumination respectively. Apparently, the responsivity values under blue and green excitation are smaller than under UV mainly due to the absence of the direct band-to-band absorption in ZnO, and weaker absorption at longer wavelengths.

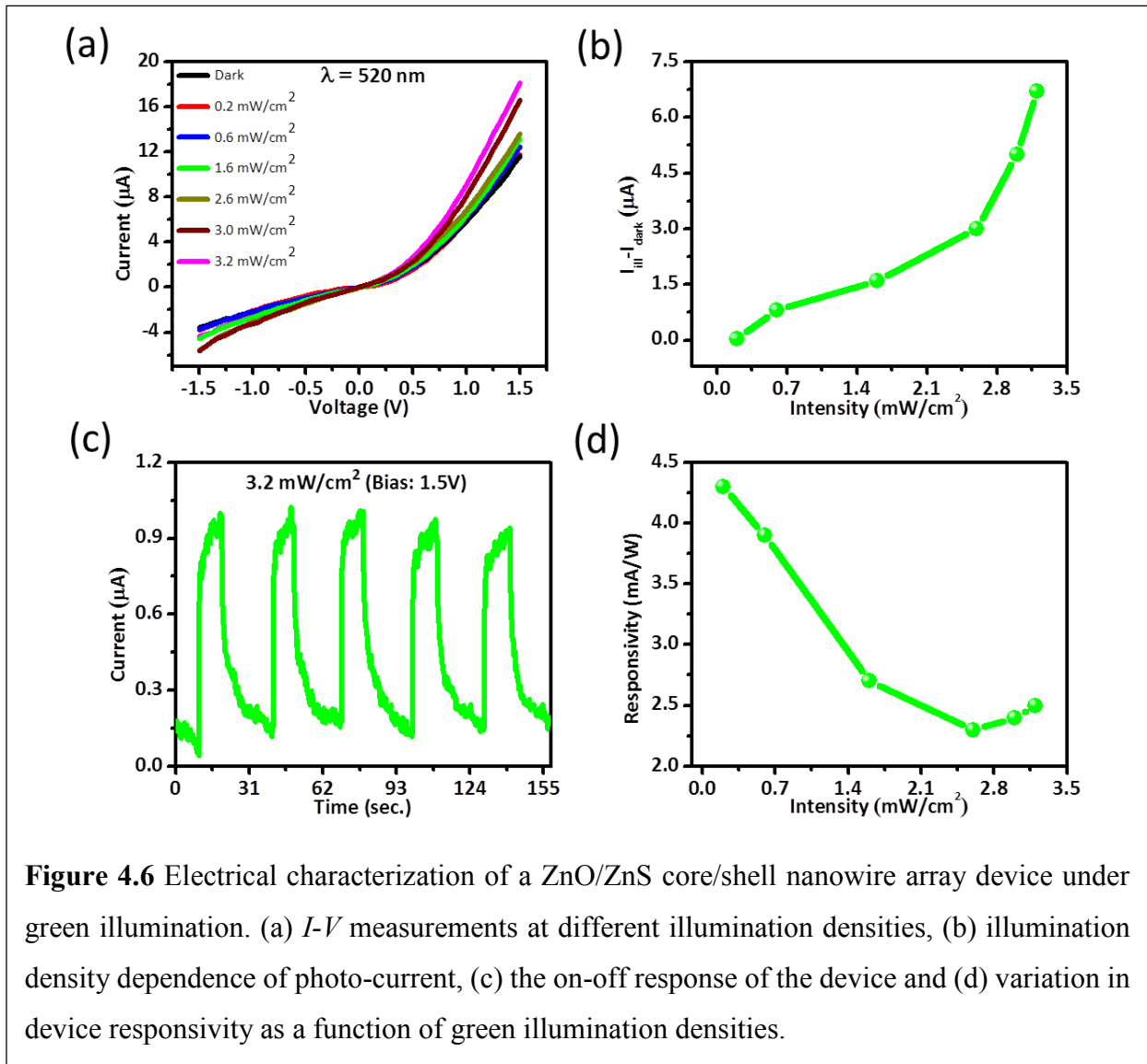


Figure 4.6 Electrical characterization of a ZnO/ZnS core/shell nanowire array device under green illumination. (a) $I-V$ measurements at different illumination densities, (b) illumination density dependence of photo-current, (c) the on-off response of the device and (d) variation in device responsivity as a function of green illumination densities.

4.3.2.3 Investigation on indirect type-II transition

It has been reported previously that strain at the heterostructure interface could reduce the natural band gap⁴⁴⁻⁴⁷ slightly, whereas only a staggered type-II band alignment could give rise to a much smaller band gap than either of the individual core or shell material.⁷ The strain and quantum confinement effect are the two reasons which may affect the natural type-II band gap (~1.93 eV) of ZnO/ZnS core/shell nanowire and these two effects were considered to predict an effective energy gap at the ZnO/ZnS interface near 2 eV for quantum core/shell nanowires.²³ In regards to the ZnO/ZnS core/shell nanowire diameter (150-200 nm), no quantum confinement effect can play a role in modifying the band gap although a weak effect of strain on type-II energy gap may exist. Figure 4.7 contains room temperature photoluminescence (PL) spectra measured with three excitation wavelengths: 325 nm, 442 nm, and 532 nm where 325 nm excitation revealed ZnO band edge emission at 3.26 eV, but the ZnS band edge emission (3.7 eV) was not present presumably due to the fact that ZnS shell is relatively thin.⁴⁸ Both blue (442 nm) and green (532 nm) lasers yield a broad band emission with its peak at around 2 eV, in general agreement with the predicted value for type-II transition.⁴⁷ Within this range, ZnO has defect-related peaks at 2.33 and 2.53 eV respectively, while 2.64 eV (ZnS) and 2.25 eV (ZnO/ZnS) were previously reported with above bandgap excitation.^{49,50} These emissions are expected to be very weak under either 442 or 532 nm excitation. Both green emission quenching⁵¹ and weak ZnS emission⁴⁸ would result in some contributions that could lead to the broad emission band which can be understood as resulting from structural fluctuations in nanowire core size and/or shell thickness, and perhaps also some defect related transitions, as observed similarly in the type-II ZnO/ZnSe core/shell nanowire array.⁵² The dominant effect of the type-II transition⁵³ observed in photodetection measurements under blue and green excitation sources is mainly attributed to the abrupt interface between the ZnO core and ZnS shell.

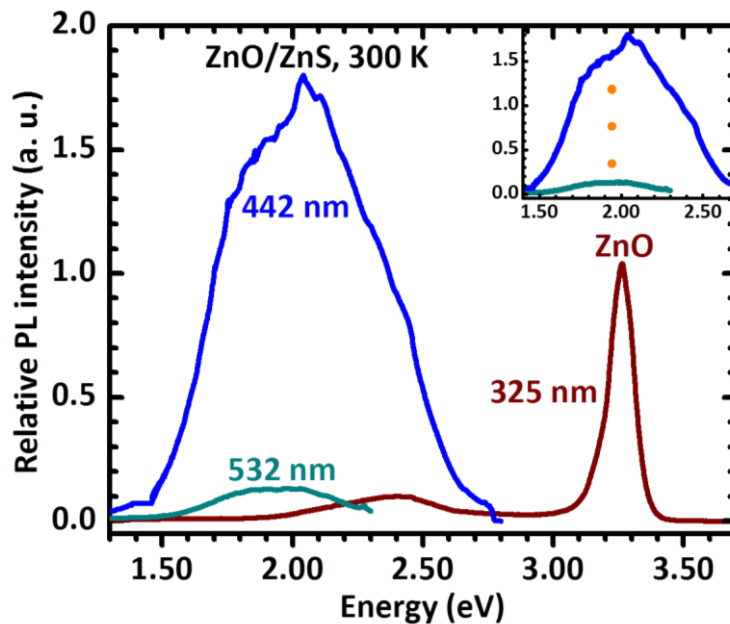
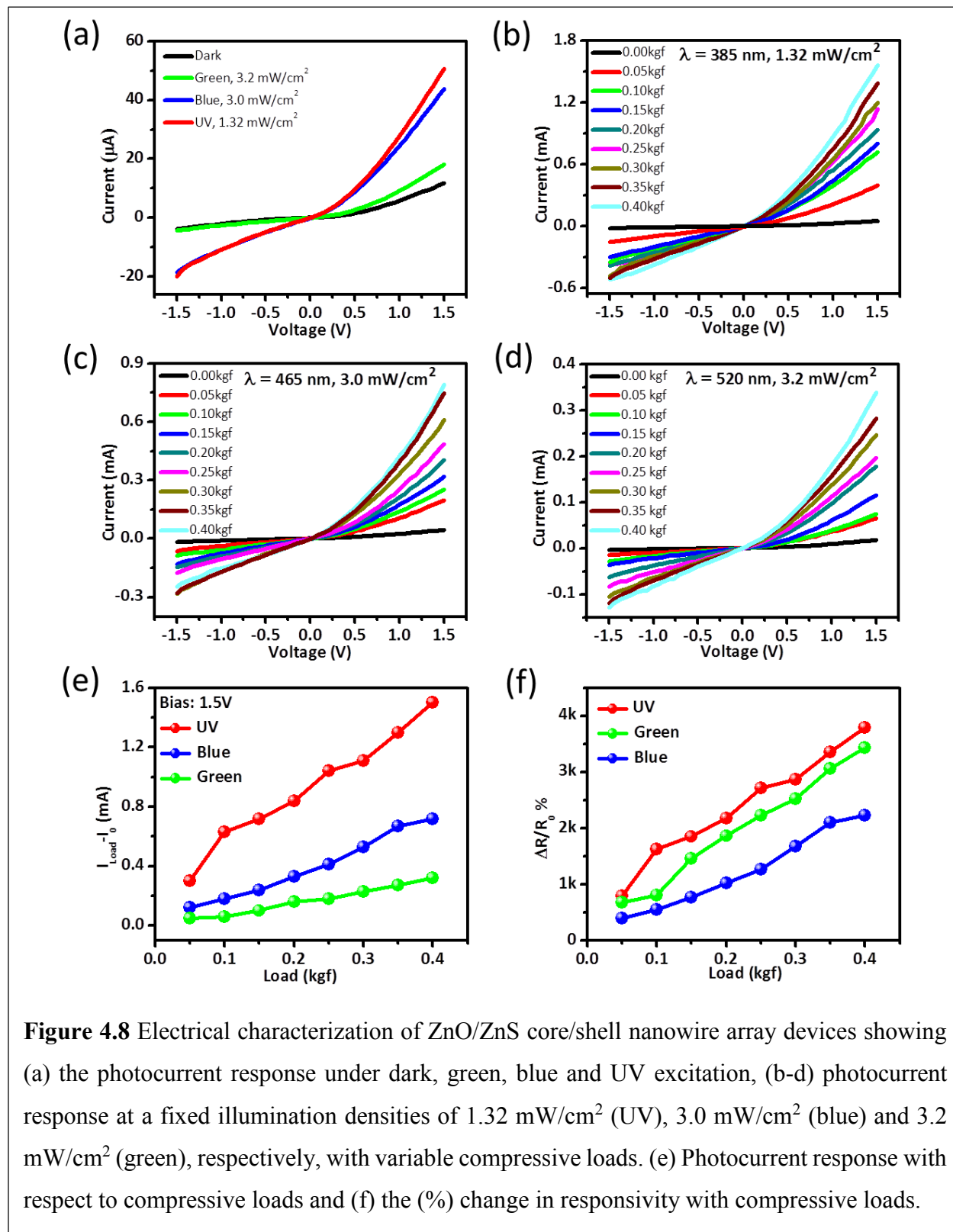


Figure 4.7 Room temperature PL for ZnO/ZnS core/shell nanowires collected with comparable laser power $\sim 145 \mu\text{W}$ under 532, 442, and 325 nm excitation, respectively. Spectra range from 1.3 eV to the edge of each laser's emission. ZnO produces green emission at 2.40 eV. Lower excitation energies produced broader type-II transition peaks. (Inset) Magnification of the type-II transition PL peaks. The dotted orange line marks the broad peak center at ~ 1.95 eV.

4.3.2.4 ZnO/ZnS core/shell nanowire piezo-phototronic photodetector

In order to investigate the effect of the built-in piezopotential on photodetector performance, ZnO/ZnS core/shell nanowire array devices were subjected to compressive loads under UV, blue and green excitation sources. Figure 4.8 (a) is a typical I - V measurement of the device at peak illumination densities under UV, blue and green excitation. In the absence of a compressive load, the peak photocurrent increases with the photon energy. Figure 4.8 (b) displays the result of I - V measurements under a compressive load varying from 0.05 kilogram force (kgf) to 0.4 kgf at a UV illumination density of $1.32 \text{ mW}/\text{cm}^2$.



It can be seen (Figure 4.8 (b)) that increasing the compressive load results in an increase in peak photocurrent under steady photon flux. Interestingly, the peak photocurrent (1.51 mA) at 0.4 kgf under steady state illumination is an order of magnitude (~31 times) higher than peak photocurrent without a load (51 μ A). A similar trend also appears in I - V measurements for blue (Figure 4.8 (c)) and green (Figure 4.8 (d)) excitation sources at fixed illumination intensities of 3 mW/cm² and 3.2 mW/cm² respectively, where the application of a compressive load resulted in a photocurrent change of an order of magnitude (~18 times) for blue and (~19 times) for green excitation sources compared to no load.

The change in peak photocurrent at compressive loads varying from 0.05 kgf to 0.4 kgf for UV (1.32 mW/cm²), blue (3 mW/cm²) and green (3.2 mW/cm²) illumination at a bias of 1.5V is summarized in Figure 4.8 (e), where the increasing photocurrent with compressive load is a trend. Additionally, the increment in peak photocurrent is found to be higher for UV illumination followed by blue and green illumination, which can be attributed to the combined effect of direct band-to-band UV absorption in ZnO and the type-II transition occurring from the ZnS_{VBM} to the ZnO_{CBM}. This band-to-band absorption for blue and green wavelengths, however, will not happen in either the ZnO core or the ZnS shell because of the very high/wide bandgap energies. This leads to photo absorption only *via* an indirect type-II transition below individual core and shell bandgap energies.

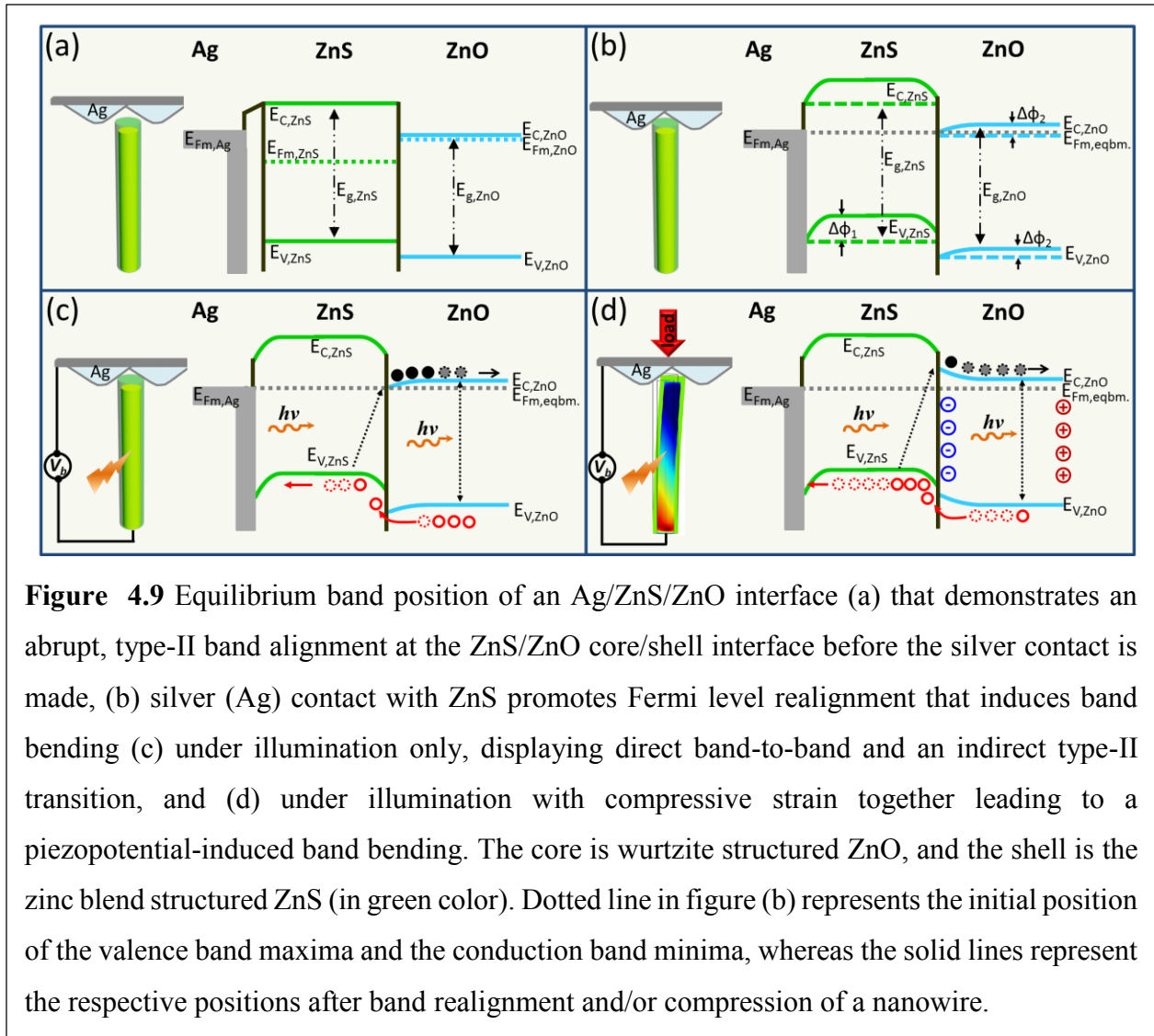
Absolute responsivities calculated for a 0.4 kgf compressive load under UV (1.32 mW/cm²), blue (3 mW/cm²) and green (3.2 mW/cm²) illumination at 1.5V bias are 2.5 A/W, 0.54 A/W and 0.13 A/W respectively, which are at least an order of magnitude higher for all the illumination sources compared to no load conditions. A comparative change in responsivity, conventionally calculated as^{10,15} $(R_{Load}-R_0/R_0)$ %, where R_{Load} and R_0 are defined as responsivities

with and without load, is displayed in Figure 4.8 (f). The (%) change in responsivity under compressive load observed in the ZnO/ZnS core/shell nanowire array photodetector is three orders of magnitude higher than the responsivity without a load.

4.4 Working principle of fully wide band gap type-II piezo-phototronic photodetector

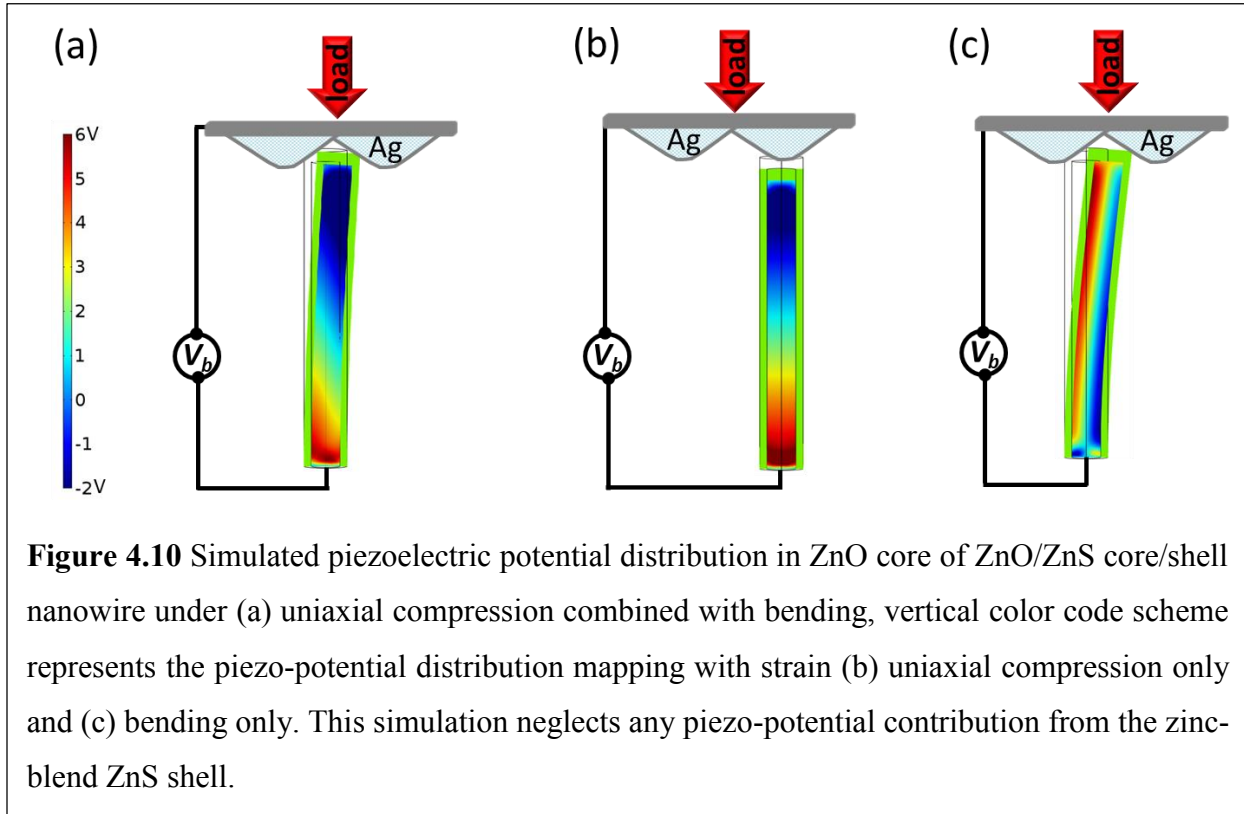
The piezo-phototronic effect enhanced performance of ZnO/ZnS core/shell nanowire array photodetector under compressive load can be qualitatively explained through band diagram and realignment of band positions under the influence of the inner piezopotential. Figure 4.9 displays the relative band positions of a ZnO/ZnS core/shell nanowire in different configurations. As shown in Figure 4.9 (a), in the absence of silver (Ag) metal contact to ZnS, there is no net charge transport across the junction because of staggered type-II band alignment where the Fermi level of ZnO is higher than that of ZnS, whereas the ZnS_{CBM} is higher than that for ZnO_{CBM} . Once silver contact to ZnS was made, the net electron transfer from silver to ZnS compensates the Fermi level imbalance, causing a downward bending of ZnS conduction and valence bands, and also compensates ZnO Fermi level imbalance with minor downward band bending as shown in Figure 4.9 (b). Under UV illumination, as shown in Figure 4.9 (c), a direct band-to-band transition takes place only in ZnO, and a weak type-II transition occurs between the ZnS_{VBM} and ZnO_{CBM} . The type-II transition is a preferred absorption mode under both blue and green illumination. No significant Fermi level shift exists in ZnO and ZnS because of weak absorption under low illumination densities, whereas the net charge transfer between ZnO and ZnS is suppressed due to the barrier created for hole injection from ZnO to ZnS, and interface trap states for electron transport generated from downward bending of ZnO. The appearance of hole and electron trap

state barriers ($\Delta\phi_1$ & $\Delta\phi_2$) are unfavorable for photosensing devices and can be tuned through the inner piezopotential to improve charge transport.



The structural characterization of ZnO/ZnS reveals that ZnS is zinc blend which is known not to possess piezoelectric property; therefore the COMSOL simulation of piezo-potential distribution in core/shell nanowire ignores the effect of ZnS shell. Figure 4.10 represents a typical simulated piezopotential distribution in ZnO core of a single ZnO/ZnS core/shell nanowire under three different strain modes at 0.4 kgf compressional load which corresponds to 200 μN at each nanowire. The strain-piezopotential distribution maps for other loads are different only in the

magnitude of piezopotential with similar distribution profile in each outlined deformation case. The scale bar representing the magnitude of piezopotential distribution by color code on vertical scale has been shown in Figure 4.10.



When nanowires are compressed under zigzag top electrode, each individual nanowire may undergo one of the three possible (Figure 4.10) elastic deformation modes, resulting in a piezopotential distribution in ZnO core of ZnO/ZnS core/shell nanowire array. In view of slight off the vertical axis oriented growth of ZnO nanowires on ITO and high length/diameter (aspect) ratio (Figure 4.3 (a)), it is reasonable to believe that under externally applied load majority of the nanowires experienced shear deformation, as shown in Figure 4.10 (a) for a single nanowire, that dominates the electrical transport properties of the device. However, the existence of either uniaxial compression (Figure 4.10 (b)) or bending only (Figure 4.10 (c)) mode of elastic

deformation in few nanowires cannot be completely ruled out. In the absence of piezoelectric effect in zinc blend structured ZnS, the localized negative polarization charges appearing in ZnO⁵⁴ at the ZnO-ZnS interface bends the edges of valence (VB) and conduction bands (CB) of ZnO to higher energy (Figure 4.9 (d)).

It should be noted that in each outlined deformation mode (Figure 4.10 a, b and c) the band position at ZnO-ZnS interface changes in similar manner provided we consider the negative polarization charges at the interface. This upward bending of bands of ZnO due to the presence of negative piezoelectric charges eliminates the pre-existing barrier $\Delta\phi_2$ that is not favorable for the separation of electrons resulting in a quick separation of holes and electrons in ZnS and ZnO, respectively (Figure 4.9 (d)), in addition to unaffected transport of type-II generated holes in ZnS. Both of these process acts synergistically to increase the conductance that results in higher current at the same bias and illumination compared to the no strain case. The moderate upward bending of ZnO valence and conduction band edges may also promote the type-II transition because the photon energies provided by blue and green excitation sources are still sufficiently high to promote electron transition from the ZnS_{VBM} to the ZnO_{CBM} , by eliminating the local trapping of electrons at the interface. Therefore, the electrons and holes are transported through the conductive channels provided by ZnO and ZnS, respectively. The piezoelectric polarization charges induced electron-hole separation is referred to as the piezo-phototronic effect,⁵⁵ and it explains the higher responsivity enhancement observed under blue and green illumination under compressive loads although the improvement is not as high as seen for UV illumination due to absence of direct band-to-band absorption.

4.5 Conclusions

In summary, an efficient and highly sensitive broad-band UV/Visible photodetector was successfully integrated on fully wide band gap ZnO/ZnS heterojunction 3D core/shell nanowire array. The abrupt interface between ZnO and ZnS plays a dominant role in photon absorption *via* an indirect type-II transition which was strongly manifested in the photodetection of visible illumination (blue and green). The absolute device responsivity was further increased through the piezo-phototronic effect by an order of magnitude under simultaneous application of load and illumination resulting in three orders of change in the relative responsivity. This investigation demonstrates an efficient prototype UV/Visible piezo-phototronic photodetector integrated on truly wide band gap 3D ZnO/ZnS core/shell nanowire array, in which the band gap limited photo absorption is overcome by a type-II transition, which enables the use of wide band gap materials in broader (UV to Visible) wavelength detection.

References

1. Wang, Z. L., *Piezotronics and Piezo-Phototronics*. Springer: 2013; p 248.
2. Feng, X.; Zhang, Y.; Wang, Z., Theoretical study of piezotronic heterojunction. *Sci. China Technol. Sci.* **2013**, *56* (11), 2615-2621.
3. Yang, Q.; Wang, W.; Xu, S.; Wang, Z. L., Enhancing Light Emission of ZnO Microwire-Based Diodes by Piezo-Phototronic Effect. *Nano Letters* **2011**, *11* (9), 4012-4017.
4. Yang, Q.; Guo, X.; Wang, W.; Zhang, Y.; Xu, S.; Lien, D. H.; Wang, Z. L., Enhancing Sensitivity of a Single ZnO Micro-/Nanowire Photodetector by Piezo-phototronic Effect. *ACS Nano* **2010**, *4* (10), 6285-6291.
5. Boxberg, F.; Søndergaard, N.; Xu, H. Q., Photovoltaics with Piezoelectric Core-Shell Nanowires. *Nano Letters* **2010**, *10* (4), 1108-1112.
6. Pan, C.; Niu, S.; Ding, Y.; Dong, L.; Yu, R.; Liu, Y.; Zhu, G.; Wang, Z. L., Enhanced Cu₂S/CdS Coaxial Nanowire Solar Cells by Piezo-Phototronic Effect. *Nano Letters* **2012**, *12* (6), 3302-3307.
7. Zhang, Y.; Lin-Wang; Mascarenhas, A., "Quantum Coaxial Cables" for Solar Energy Harvesting. *Nano Letters* **2007**, *7* (5), 1264-1269.
8. Wang, K.; Chen, J.; Zhou, W.; Zhang, Y.; Yan, Y.; Pern, J.; Mascarenhas, A., Direct Growth of Highly Mismatched Type II ZnO/ZnSe Core/Shell Nanowire Arrays on Transparent Conducting Oxide Substrates for Solar Cell Applications. *Advanced Materials* **2008**, *20* (17), 3248-3253.
9. Wu, Z.; Zhang, Y.; Zheng, J.; Lin, X.; Chen, X.; Huang, B.; Wang, H.; Huang, K.; Li, S.; Kang, J., An all-inorganic type-II heterojunction array with nearly full solar spectral response based on ZnO/ZnSe core/shell nanowires. *Journal of Materials Chemistry* **2011**, *21* (16), 6020-6026.

10. Zhang, F.; Ding, Y.; Zhang, Y.; Zhang, X.; Wang, Z. L., Piezo-phototronic Effect Enhanced Visible and Ultraviolet Photodetection Using a ZnO–CdS Core–Shell Micro/nanowire. *ACS Nano* **2012**, *6* (10), 9229-9236.
11. Wallentin, J.; Anttu, N.; Asoli, D.; Huffman, M.; Åberg, I.; Magnusson, M. H.; Siefert, G.; Fuss-Kailuweit, P.; Dimroth, F.; Witzigmann, B.; Xu, H. Q.; Samuelson, L.; Deppert, K.; Borgström, M. T., InP Nanowire Array Solar Cells Achieving 13.8% Efficiency by Exceeding the Ray Optics Limit. *Science* **2013**, *339* (6123), 1057-1060.
12. Law, M.; Greene, L. E.; Johnson, J. C.; Saykally, R.; Yang, P., Nanowire dye-sensitized solar cells. *Nat Mater* **2005**, *4* (6), 455-459.
13. Yao, M.; Huang, N.; Cong, S.; Chi, C.-Y.; Seyedi, M. A.; Lin, Y.-T.; Cao, Y.; Povinelli, M. L.; Dapkus, P. D.; Zhou, C., GaAs Nanowire Array Solar Cells with Axial p–i–n Junctions. *Nano Letters* **2014**, *14* (6), 3293-3303.
14. Liu, Y.; Yang, Q.; Zhang, Y.; Yang, Z.; Wang, Z. L., Nanowire Piezo-phototronic Photodetector: Theory and Experimental Design. *Advanced Materials* **2012**, *24* (11), 1410-1417.
15. Zhang, F.; Niu, S.; Guo, W.; Zhu, G.; Liu, Y.; Zhang, X.; Wang, Z. L., Piezo-phototronic Effect Enhanced Visible/UV Photodetector of a Carbon-Fiber/ZnO–CdS Double-Shell Microwire. *ACS Nano* **2013**, *7* (5), 4537-4544.
16. Wang, Z.; Yu, R.; Pan, C.; Liu, Y.; Ding, Y.; Wang, Z. L., Piezo-Phototronic UV/Visible Photosensing with Optical-Fiber–Nanowire Hybridized Structures. *Advanced Materials* **2015**, n/a-n/a.
17. Wang, Z. L.; Song, J., Piezoelectric Nanogenerators Based on Zinc Oxide Nanowire Arrays. *Science* **2006**, *312* (5771), 242-246.
18. Wang, X.; Song, J.; Liu, J.; Wang, Z. L., Direct-Current Nanogenerator Driven by Ultrasonic Waves. *Science* **2007**, *316* (5821), 102-105.

19. Pan, C.; Dong, L.; Zhu, G.; Niu, S.; Yu, R.; Yang, Q.; Liu, Y.; Wang, Z. L., High-resolution electroluminescent imaging of pressure distribution using a piezoelectric nanowire LED array. *Nat Photon* **2013**, *7* (9), 752-758.
20. Pradel, K. C.; Wu, W.; Ding, Y.; Wang, Z. L., Solution-Derived ZnO Homojunction Nanowire Films on Wearable Substrates for Energy Conversion and Self-Powered Gesture Recognition. *Nano Letters* **2014**, *14* (12), 6897-6905.
21. Li, X.; Lin, Z.-H.; Cheng, G.; Wen, X.; Liu, Y.; Niu, S.; Wang, Z. L., 3D Fiber-Based Hybrid Nanogenerator for Energy Harvesting and as a Self-Powered Pressure Sensor. *ACS Nano* **2014**, *8* (10), 10674-10681.
22. Wang, K.; Chen, J. J.; Zeng, Z. M.; Tarr, J.; Zhou, W. L.; Zhang, Y.; Yan, Y. F.; Jiang, C. S.; Pern, J.; Mascarenhas, A., Synthesis and photovoltaic effect of vertically aligned ZnO/ZnS core/shell nanowire arrays. *Applied Physics Letters* **2010**, *96* (12), 123105.
23. Schrier, J.; Demchenko, D. O.; Wang, Alivisatos, A. P., Optical Properties of ZnO/ZnS and ZnO/ZnTe Heterostructures for Photovoltaic Applications. *Nano Letters* **2007**, *7* (8), 2377-2382.
24. Yan, C.; Xue, D., Conversion of ZnO Nanorod Arrays into ZnO/ZnS Nanocable and ZnS Nanotube Arrays via an in Situ Chemistry Strategy. *The Journal of Physical Chemistry B* **2006**, *110* (51), 25850-25855.
25. Ahmad, M.; Yan, X.; Zhu, J., Controlled Synthesis, Structural Evolution, and Photoluminescence Properties of Nanoscale One-Dimensional Hierarchical ZnO/ZnS Heterostructures. *The Journal of Physical Chemistry C* **2011**, *115* (5), 1831-1837.
26. Panda, S. K.; Dev, A.; Chaudhuri, S., Fabrication and Luminescent Properties of c-Axis Oriented ZnO-ZnS Core-Shell and ZnS Nanorod Arrays by Sulfidation of Aligned ZnO Nanorod Arrays. *The Journal of Physical Chemistry C* **2007**, *111* (13), 5039-5043.
27. Huang, X.; Wang, M.; Willinger, M.-G.; Shao, L.; Su, D. S.; Meng, X.-M., Assembly of Three-Dimensional Hetero-Epitaxial ZnO/ZnS Core/Shell Nanorod and Single Crystalline Hollow ZnS Nanotube Arrays. *ACS Nano* **2012**, *6* (8), 7333-7339.

28. Athauda, T. J.; Madduma-Bandarage, U. S. K.; Vasquez, Y., Integration of ZnO/ZnS nanostructured materials into a cotton fabric platform. *RSC Advances* **2014**, *4* (106), 61327-61332.
29. Zhang, W.; Wang, S.; Wang, Y.; Zhu, Z.; Gao, X.; Yang, J.; Zhang, H. x., ZnO@ZnS core/shell microrods with enhanced gas sensing properties. *RSC Advances* **2015**, *5* (4), 2620-2629.
30. Lu, M.-Y.; Song, J.; Lu, M.-P.; Lee, C.-Y.; Chen, L.-J.; Wang, Z. L., ZnO–ZnS Heterojunction and ZnS Nanowire Arrays for Electricity Generation. *ACS Nano* **2009**, *3* (2), 357-362.
31. Qin, Y.; Wang, X.; Wang, Z. L., Microfibre-nanowire hybrid structure for energy scavenging. *Nature* **2008**, *451* (7180), 809-813.
32. Zhang, Z.; Liao, Q.; Yu, Y.; Wang, X.; Zhang, Y., Enhanced photoresponse of ZnO nanorods-based self-powered photodetector by piezotronic interface engineering. *Nano Energy* **2014**, *9* (0), 237-244.
33. Wang, Y.; Zhan, X.; Wang, F.; Wang, Q.; Safdar, M.; He, J., Crystalline ZnO/ZnS_xSe_{1-x} core-shell nanowire arrays for efficient visible-light photoelectrocatalysis. *Journal of Materials Chemistry A* **2014**, *2* (43), 18413-18419.
34. Wang, K.; Rai, S. C.; Marmon, J.; Chen, J.; Yao, K.; Wozny, S.; Cao, B.; Yan, Y.; Zhang, Y.; Zhou, W., Nearly lattice matched all wurtzite CdSe/ZnTe type II core-shell nanowires with epitaxial interfaces for photovoltaics. *Nanoscale* **2014**, *6* (7), 3679-3685.
35. Soga, T., Preface. In *Nanostructured Materials for Solar Energy Conversion*, Soga, T., Ed. Elsevier: Amsterdam, 2006; pp v-vi.
36. Fang, X.; Bando, Y.; Liao, M.; Gautam, U. K.; Zhi, C.; Dierre, B.; Liu, B.; Zhai, T.; Sekiguchi, T.; Koide, Y.; Golberg, D., Single-Crystalline ZnS Nanobelts as Ultraviolet-Light Sensors. *Advanced Materials* **2009**, *21* (20), 2034-2039.

37. Vj, L.; Oh, J.; Nayak, A. P.; Katzenmeyer, A. M.; Gilchrist, K. H.; Grego, S.; Kobayashi, N. P.; Shih-Yuan, W.; Talin, A. A.; Dhar, N. K.; Islam, M. S., A Perspective on Nanowire Photodetectors: Current Status, Future Challenges, and Opportunities. *Selected Topics in Quantum Electronics, IEEE Journal of* **2011**, *17* (4), 1002-1032.
38. Ni, P.-N.; Shan, C.-X.; Wang, S.-P.; Liu, X.-Y.; Shen, D.-Z., Self-powered spectrum-selective photodetectors fabricated from n-ZnO/p-NiO core-shell nanowire arrays. *Journal of Materials Chemistry C* **2013**, *1* (29), 4445-4449.
39. Zhu, H.; Shan, C. X.; Yao, B.; Li, B. H.; Zhang, J. Y.; Zhao, D. X.; Shen, D. Z.; Fan, X. W., High Spectrum Selectivity Ultraviolet Photodetector Fabricated from an n-ZnO/p-GaN Heterojunction. *The Journal of Physical Chemistry C* **2008**, *112* (51), 20546-20548.
40. Lin, P.; Chen, X.; Yan, X.; Zhang, Z.; Yuan, H.; Li, P.; Zhao, Y.; Zhang, Y., Enhanced photoresponse of Cu₂O/ZnO heterojunction with piezo-modulated interface engineering. *Nano Res.* **2014**, *7* (6), 860-868.
41. Qin, L.; Shao, D.; Shing, C.; Sawyer, S., Wavelength selective p-GaN/ZnO colloidal nanoparticle heterojunction photodiode. *Applied Physics Letters* **2013**, *102* (7), -.
42. Soci, C.; Zhang, A.; Xiang, B.; Dayeh, S. A.; Aplin, D. P. R.; Park, J.; Bao, X. Y.; Lo, Y. H.; Wang, D., ZnO Nanowire UV Photodetectors with High Internal Gain. *Nano Letters* **2007**, *7* (4), 1003-1009.
43. Srikant, V.; Clarke, D. R., On the optical band gap of zinc oxide. *Journal of Applied Physics* **1998**, *83* (10), 5447-5451.
44. Morkel, M.; Weinhardt, L.; Lohmüller, B.; Heske, C.; Umbach, E.; Riedl, W.; Zweigart, S.; Karg, F., Flat conduction-band alignment at the CdS/CuInSe₂ thin-film solar-cell heterojunction. *Applied Physics Letters* **2001**, *79* (27), 4482-4484.
45. Moon, C.-Y.; Wei, S.-H.; Zhu, Y. Z.; Chen, G. D., Band-gap bowing coefficients in large size-mismatched II-VI alloys: first-principles calculations. *Physical Review B* **2006**, *74* (23), 233202.

46. Haight, R.; Barkhouse, A.; Gunawan, O.; Shin, B.; Copel, M.; Hopstaken, M.; Mitzi, D. B., Band alignment at the $\text{Cu}_2\text{ZnSn}(\text{S}_x\text{Se}_{1-x})_4/\text{CdS}$ interface. *Applied Physics Letters* **2011**, *98* (25), 253502.
47. Sun, L.; Haight, R.; Sinsersuksakul, P.; Bok Kim, S.; Park, H. H.; Gordon, R. G., Band alignment of $\text{SnS}/\text{Zn}(\text{O},\text{S})$ heterojunctions in SnS thin film solar cells. *Applied Physics Letters* **2013**, *103* (18), 181904.
48. Murphy, M. W.; Zhou, X. T.; Ko, J. Y. P.; Zhou, J. G.; Heigl, F.; Sham, T. K., Optical emission of biaxial ZnO-ZnS nanoribbon heterostructures. *The Journal of Chemical Physics* **2009**, *130* (8), 084707.
49. Wang, X.; Gao, P.; Li, J.; Summers, C. J.; Wang, Z. L., Rectangular Porous ZnO-ZnS Nanocables and ZnS Nanotubes. *Advanced Materials* **2002**, *14* (23), 1732-1735.
50. Zhang, S.; Yin, B.; Jiang, H.; Qu, F.; Umar, A.; Wu, X., Hybrid ZnO/ZnS nanoforests as the electrode materials for high performance supercapacitor application. *Dalton Transactions* **2015**, *44* (5), 2409-2415.
51. Li, J.; Zhao, D.; Meng, X.; Zhang, Z.; Zhang, J.; Shen, D.; Lu, Y.; Fan, X., Enhanced Ultraviolet Emission from ZnS -Coated ZnO Nanowires Fabricated by Self-Assembling Method. *The Journal of Physical Chemistry B* **2006**, *110* (30), 14685-14687.
52. Zhang, Y.; Wu, Z.; Zheng, J.; Lin, X.; Zhan, H.; Li, S.; Kang, J.; Bleuse, J.; Mariette, H., ZnO/ZnSe type II core-shell nanowire array solar cell. *Solar Energy Materials and Solar Cells* **2012**, *102* (0), 15-18.
53. Vainorius, N.; Jacobsson, D.; Lehmann, S.; Gustafsson, A.; Dick, K. A.; Samuelson, L.; Pistol, M.-E., Observation of type-II recombination in single wurtzite/zinc-blende GaAs heterojunction nanowires. *Physical Review B* **2014**, *89* (16), 165423.
54. Gao, Y.; Wang, Z. L., Equilibrium Potential of Free Charge Carriers in a Bent Piezoelectric Semiconductive Nanowire. *Nano Letters* **2009**, *9* (3), 1103-1110.

55. Liu, Y.; Zhang, Y.; Yang, Q.; Niu, S.; Wang, Z. L., Fundamental theories of piezotronics and piezo-phototronics. *Nano Energy* (0).

Chapter 5 3D ZnO nanowire based piezo-magneto-photo sensor

5.1 Introduction

Optoelectronic devices integrated on nanostructures semiconductors are considered crucial to achieve improved device performance arising from high surface to volume ratio and also for miniaturization of these devices¹⁻⁶ for optoelectronic device applications such as in transistors,⁷⁻⁹ field emitters,¹⁰⁻¹³ photodetectors^{14,15} and solar cells.¹⁶⁻¹⁹ Especially, oxide nanostructures such as ZnO, SnO₂, etc. are of particular importance owing to their relatively easier synthesis²⁰ by low temperature hydrothermal/solvothermal and thermal evaporation methods for their application in visible-blind photodetectors^{21,22} arising from their wide band gap. In particular, ZnO nanostructures has attracted much attention because of its piezoelectric property and non-cytotoxicity which makes it suitable for self-powered environmentally friendly device applications. Starting from past decade, research efforts on one dimensional ZnO nanostructures has led to demonstration of its piezoelectric property enabled mechanical to electrical energy nanogenerator device for powering micro/nanosystems.²³⁻²⁵ Since then, coupling of piezoelectric and semiconducting property in ZnO nanowires has been reported to significantly affect the performance of the devices such as photodetectors,^{26,27} biological sensors,²⁸ and light emitting diodes²⁹ by tuning/controlling the charge carrier generation, recombination and/or transport across interface/junction popularly known as piezotronics³⁰ and piezo-phototronics.³¹ It is apparent that continued research efforts are focused on improving the performance of the device without cumbersome materials processing steps, such as doping and surface passivation or intricate device

designs which may not be scalable. The coupling of inherent material properties such as semiconducting, optical, electrical/magnetic, and piezoelectric is rather more advantageous to achieve improved device performance and/or to have multiple functionalities in a single device. In a similar way, external stimulus magnetic field³² has also been investigated for its effect on the performance of the devices and has been reported that external field does affect the performance of the device and has been successfully applied in bipolar transistors,³³ photovoltaics,³⁴ photodetection³⁵ and logic devices.³⁶ From these findings it can be anticipated that the effect of external stimulus must also act on the devices working on the principle of piezotronic and piezo-phototronic where coupled piezoelectric and semiconducting property can further be influenced by externally applied field. However, so far there is no such report on investigation of external field effect on the performance of piezo-phototronic device except one, where effect of external electric field on the performance of piezotronic device was studied.³⁷ The findings suggests that the Schottky barrier height changes under the influence of external electric field in a way that piezotronic effect was suppressed.

Owing to excellent semiconducting and piezoelectric properties, ZnO is an ideal platform to study the effect of external magnetic field on the piezo-phototronic effect which can enable the design of new class of sensor having multiple functionalities such as photosensors, magnetosensors and pressure sensors or a combination of these thereof. In the present work we investigate the effect of external magnetic field on the performance of ZnO nanowire array based piezotronic and piezo-phototronic device. The study reveals that external magnetic field can tune the piezotronic device performance making it suitable for magnetic field sensorics and, in particular, piezo-phototronic effect can be further improved under the influence of external magnetic field. The

findings are supported by theoretical simulations and a working mechanism is also proposed for this device.

5.2 Experimental

5.2.1 Synthesis and Characterization

Synthesis of ZnO nanowire array was performed as per the details mentioned in earlier chapter section 4.2.1. Briefly, ZnO nanowire array was grown on SiO₂ passivated ITO/glass (CG80IN, Delta Technologies LTD) substrate by thermal evaporation of Zn powder (99.9%, metals basis, Alfa Aesar). Structural and morphological characterizations were carried out with HITACHI Su8010 field-emission scanning electron microscope (FESEM), and a FEI Tecnai G2 F30 ST high-resolution transmission electron microscope (HRTEM) equipped with a nanoprobe energy-dispersive (EDS) X-ray spectroscope.

5.2.2 Device fabrication and measurements

For detailed description of device fabrication steps, section 4.2.4 from chapter 4 should be consulted except for the change that external magnetic field was applied parallel to the Ag-ZnO interface, i.e. perpendicular to the substrate plane and along z-axis (c-axis of nanowire growth). The field was applied along all three mutually orthogonal axes namely, x , y and z -axis and observed changes in I - V measurements are discussed in the sections to follow. A brief schematics of the device processing key steps are illustrated in Figure 5.1 (a-d). The electrical measurements were carried out using low noise current pre-amplifier (SR-570, Stanford Research Systems), and a source meter (Keithley-2401) coupled with a computer interface.

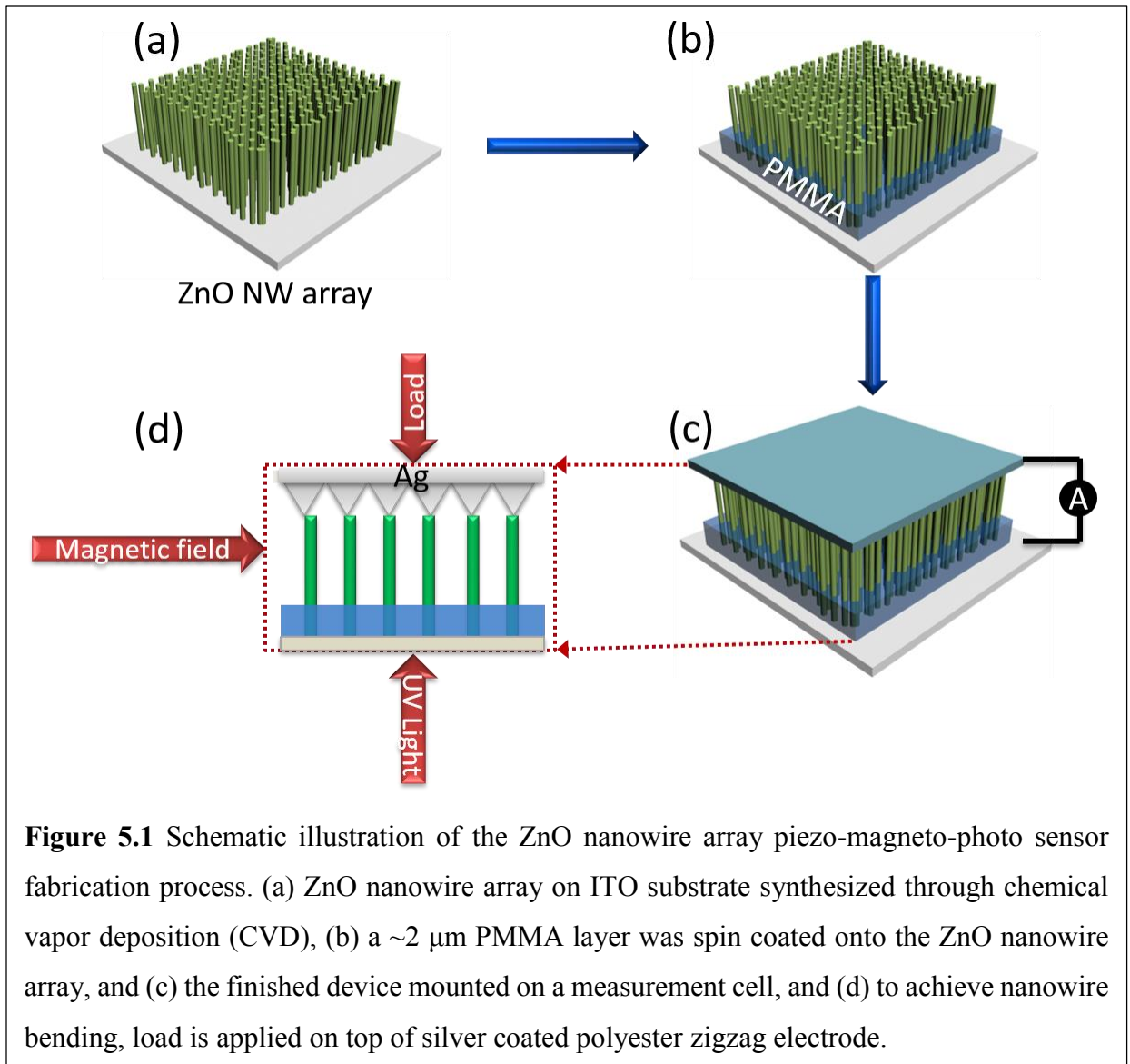
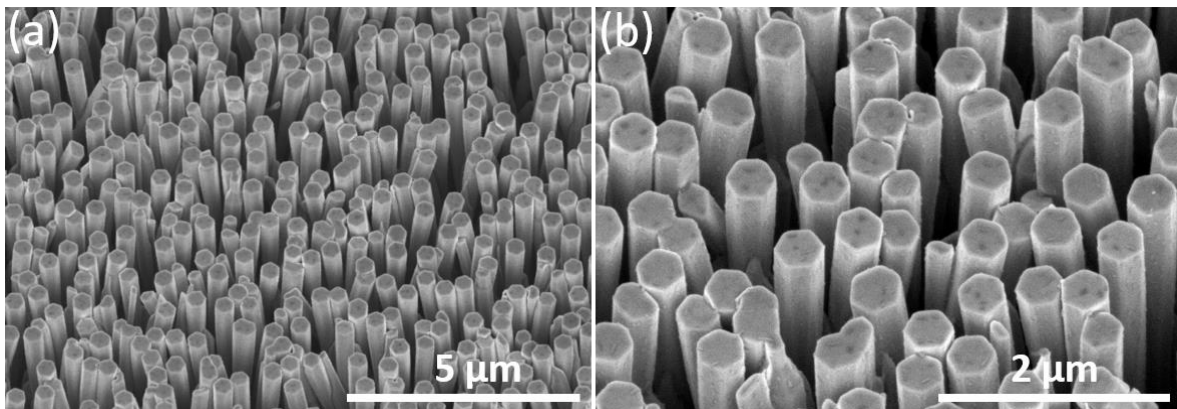


Figure 5.1 Schematic illustration of the ZnO nanowire array piezo-magneto-photo sensor fabrication process. (a) ZnO nanowire array on ITO substrate synthesized through chemical vapor deposition (CVD), (b) a $\sim 2 \mu\text{m}$ PMMA layer was spin coated onto the ZnO nanowire array, and (c) the finished device mounted on a measurement cell, and (d) to achieve nanowire bending, load is applied on top of silver coated polyester zigzag electrode.

5.3 Results and Discussion

5.3.1 Structure characterization

Figure 5.2 displays result of structure characterization of ZnO nanowires, where Figure 5.2 (a) and (b) are low and high magnification tilted top view FESEM image of ZnO nanowire array grown on ITO substrate. The typical length and diameter of ZnO nanowires are $\sim 5 \mu\text{m}$ and $\sim 300 \text{nm}$, respectively.



Missing low mag TEM/SAED and HRTEM of ZnO nanowire

Figure 5.2 Structural characterization of a ZnO nanowire array, showing (a) low and (b) high magnification tilted top view, FESEM images of as-grown, ZnO nanowire array, (c) low magnification TEM image of a single ZnO nanowire, and (d) HRTEM image and (inset) SAED pattern of ZnO nanowire depicting characteristic single crystal diffraction pattern.

It can be seen that the nanowires are preferentially aligned to the substrate normal and are grown with uniform coverage and high density. Similar length and diameter of the nanowires is highly desirable in order to achieve maximum number of nanowires in contact with top electrode and for optimum straining where each individual nanowire experiences almost same magnitude of elastic deformation. Figure 5.2 (c) is a low magnification TEM image showing clean surface and uniform diameter of ZnO nanowire from tip to base and Figure 5.2 (d) is HRTEM image of the

same nanowires where lattice fringes and SAED characteristic of single crystal ZnO wurtzite structure can be clearly seen.

5.3.2 ZnO nanowire array piezo-magneto sensor

Figure 5.3 summarizes the *I-V* measurements of ZnO nanowire array based piezo-magneto sensor in dark where Figure 5.3 (a) represents the *I-V* measurements of the device subjected to variable strain under different compressional loads only, ranging from 0 to 100 gram force (gf). It can be seen that the peak dark current value increases gradually from $\sim 65 \mu\text{A}$ at no strain to $\sim 536 \mu\text{A}$ at 100 gf of straining load, which amounts to $\sim 725\%$ of increment in peak current. This increase in the peak current can be attributed to the lowering of Schottky barrier height at ZnO/Ag interface resulting from inner piezopotential generated due to the bending under compressional load.²⁶ Figure 5.3 (b) is the *I-V* measurement of the device under same measurement condition except that the device was exposed to a uniform magnetic field of strength $600 \mu\text{T}$ along a direction parallel to the ZnO/Ag contact plane and perpendicular to the axis of nanowire growth. The absolute peak current for no load condition is persevered whereas the peak current at maximum of 100 gf load decreases to $\sim 507 \mu\text{A}$. The same trend of decrease in peak dark current is also evident from the measurement of peak current at 5 gf where it decreases from $\sim 84 \mu\text{A}$ to $\sim 77 \mu\text{A}$, at 20 gf from $\sim 147 \mu\text{A}$ to $\sim 126 \mu\text{A}$, and at 50 gf from $\sim 429 \mu\text{A}$ to $\sim 422 \mu\text{A}$.

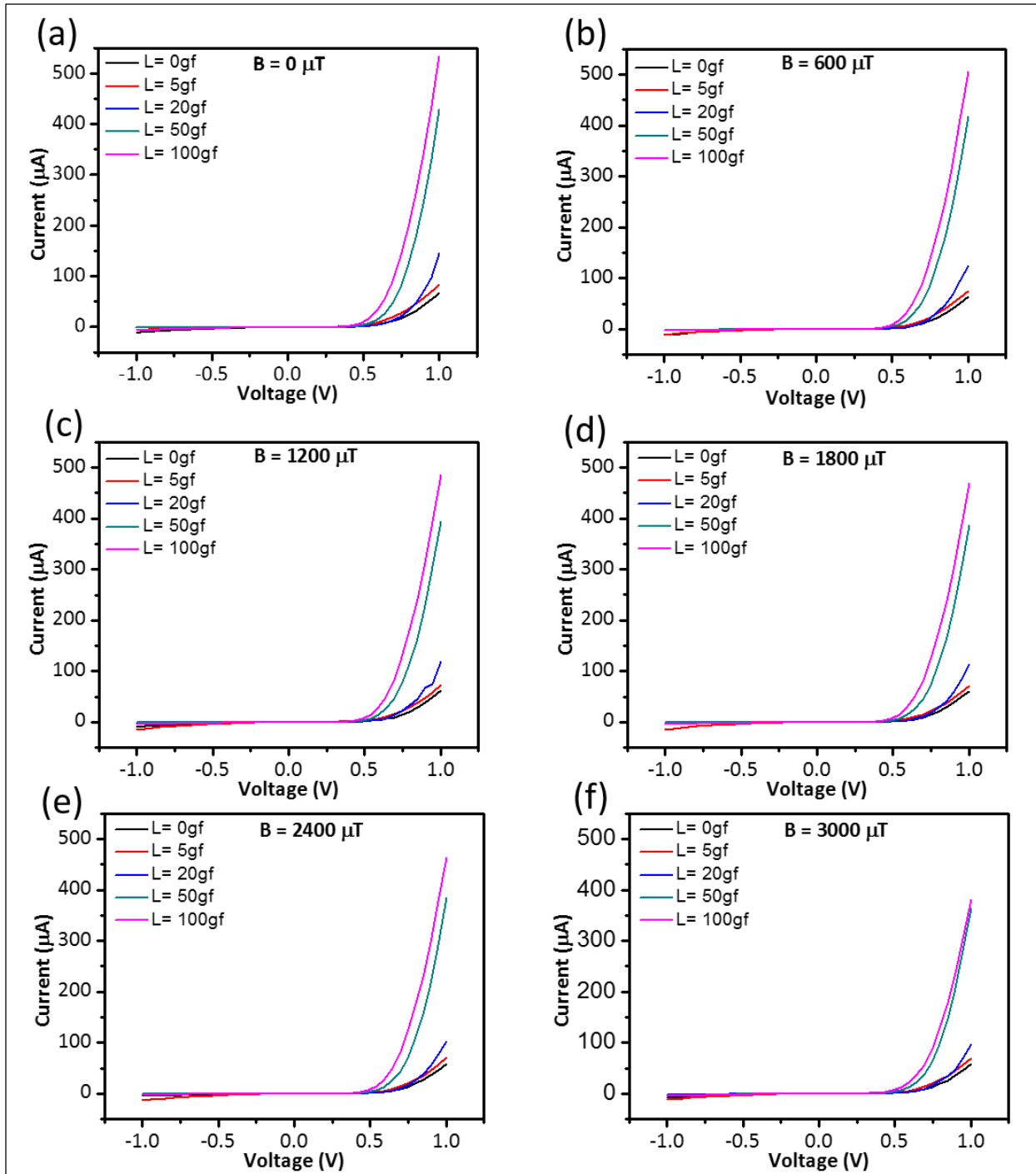


Figure 5.3 Typical I - V characteristic of ZnO nanowire array based piezo-magneto sensor in dark under (a) compressional strain only and (b-f) under compressional strain combined with 600-3000 μT of external magnetic field. A successive decrease in peak current is apparent with increasing magnetic field strength for any particular fixed strain amount.

The decrease amount to $\sim 6-8\%$ in our case of small strain generating compressional loads was a distinct and reproducible feature observed over every measurement performed repeatedly and cannot be attributed to measurement error. The device was then investigated for its behavior under linearly increasing magnetic field strengths applied in multiples of $600 \mu\text{T}$ and reaching to a maximum of up to $3000 \mu\text{T}$ in order to understand the effect of external magnetic field of piezotronic behavior of the device and to rule out the measurement error factor. Figure 5.3 (c-f) represents the $I-V$ measurements of the device performed under $1200, 1800, 2400$ and $3000 \mu\text{T}$ of magnetic field strength while keeping the compressional loads as same as used in $600 \mu\text{T}$ measurement condition, Figure 5.3 (b). In each measurement condition the peak current displays consistent decreasing trend with increasing strength of magnetic field at any fixed load and at maximum field strength of $3000 \mu\text{T}$ and 100 gf the peak current attains a value of $\sim 383 \mu\text{A}$ compared to peak current of $\sim 536 \mu\text{A}$ at no field for 100 gf compressional load which amounts to a decrease of $\sim 29\%$. This significant decrease in peak current in dark and under $3000 \mu\text{T}$ of field strength is indicative of the external field influence on the performance of piezotronic device and suggests an underlying coupling mechanism. The findings are similar in nature as published earlier investigating the effect of external electric field on the performance of single ZnO nanowire based piezotronic device where the decrease in the response was attributed to the suppression of piezotronic effect by high strength electric field which happens to change the contact between ZnO-Ag from Schottky to Ohmic resulting in non-rectifying $I-V$ curve.³⁷ However, the changeover of Schottky to Ohmic contact between ZnO-Ag is not true in our case as the $I-V$ curves (Figure 5.3) are still rectifying in nature. In order to investigate the Schottky to Ohmic flattening of contact between ZnO-Ag for our 3D piezotronic device, measurements were carried out in magnetic field

strengths two orders of magnitude higher than the previously used 3000 μT and results are summarized in Figure 5.4.

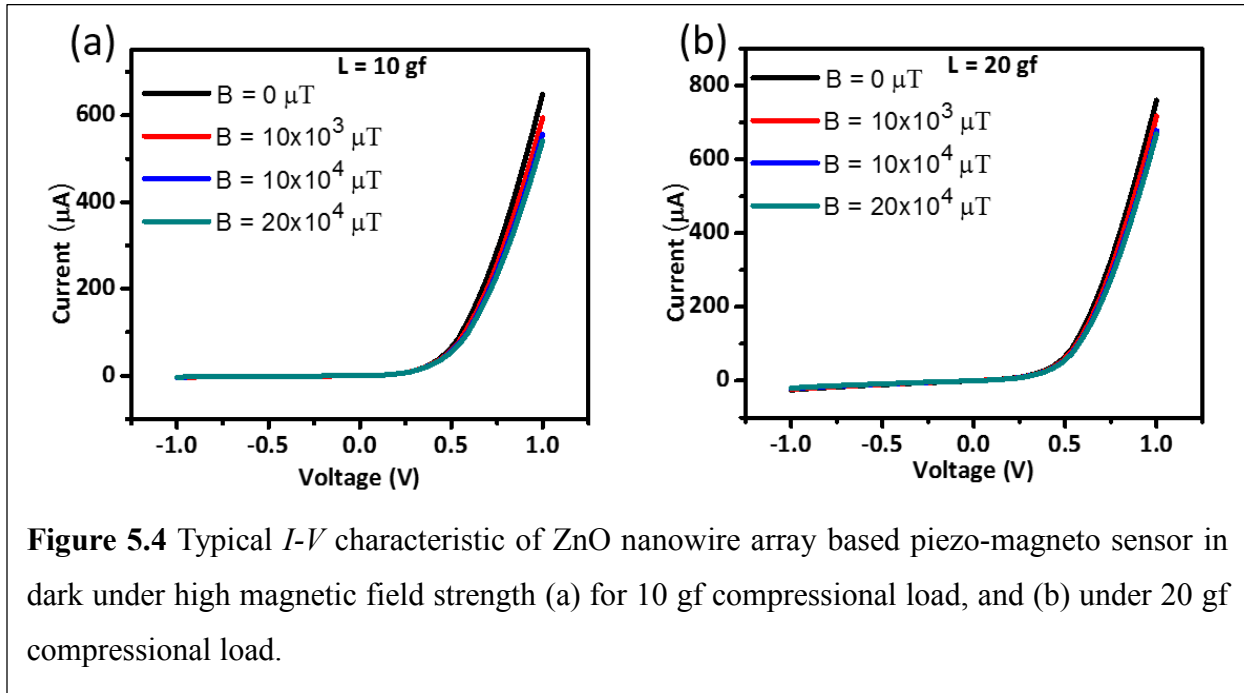


Figure 5.4 Typical *I-V* characteristic of ZnO nanowire array based piezo-magneto sensor in dark under high magnetic field strength (a) for 10 gf compressional load, and (b) under 20 gf compressional load.

In Figure 5.4 (a), *I-V* curves were recorded in dark for 10 gf compressional load at 0- $20 \times 10^4 \mu\text{T}$ field strengths where the decrease in peak current is apparent as magnetic field strength increases and at peak magnetic field strength of $20 \times 10^4 \mu\text{T}$ the total decrease amounts to be $\sim 17\%$. In a similar measurement that was performed with 20 gf force on the same device the total decrease in peak current amounts to $\sim 12\%$. However, in spite of following the decreasing trend in the peak current under magnetic field, the *I-V* curves still maintains the rectifying behavior as was seen at low magnetic field strengths (Figure 5.3) indicating that the Schottky contact between ZnO-Ag remains unaffected under magnetic field and whatever nominal Schottky barrier modulation occurs is only resulting from immobile polarization charges.²⁷

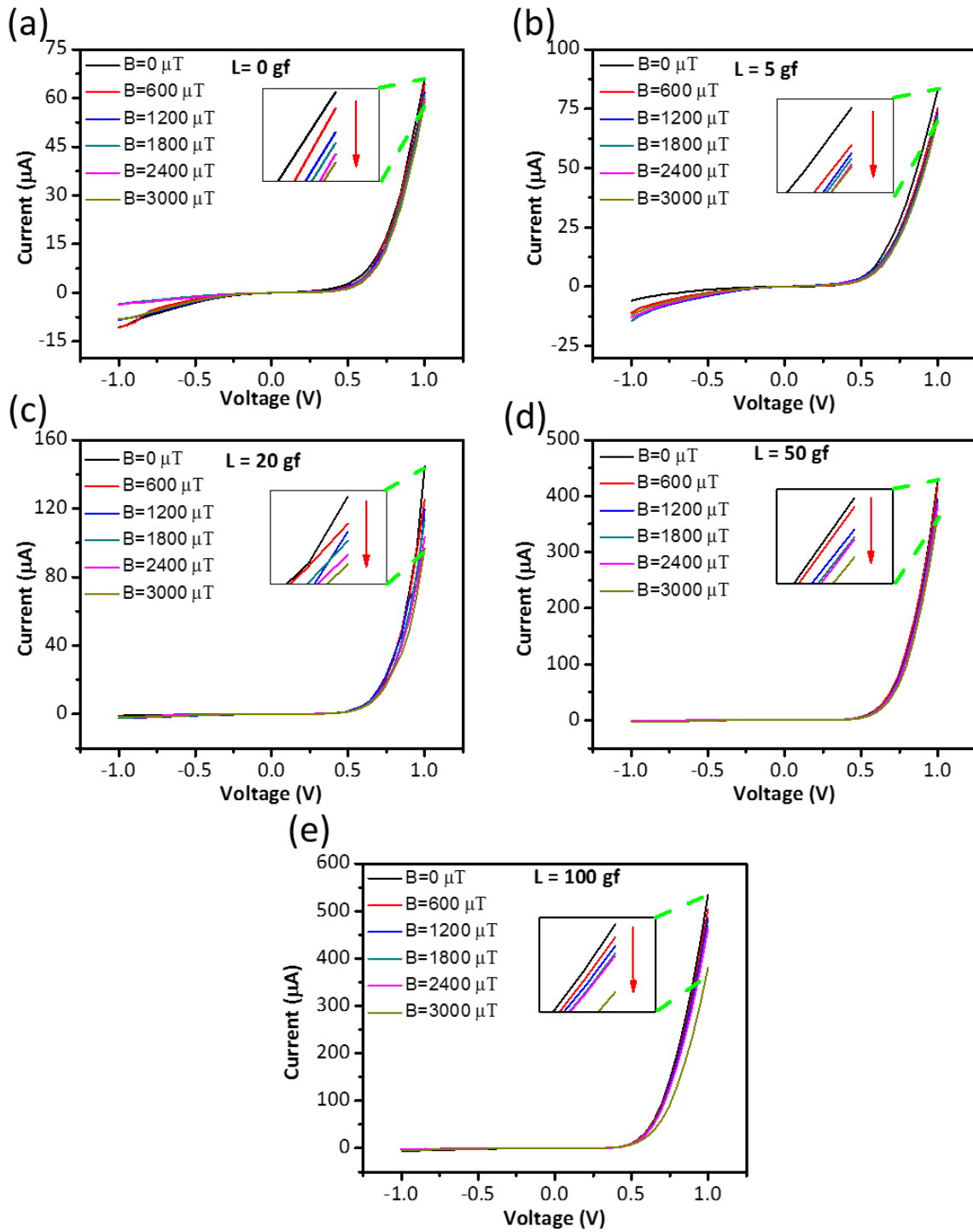
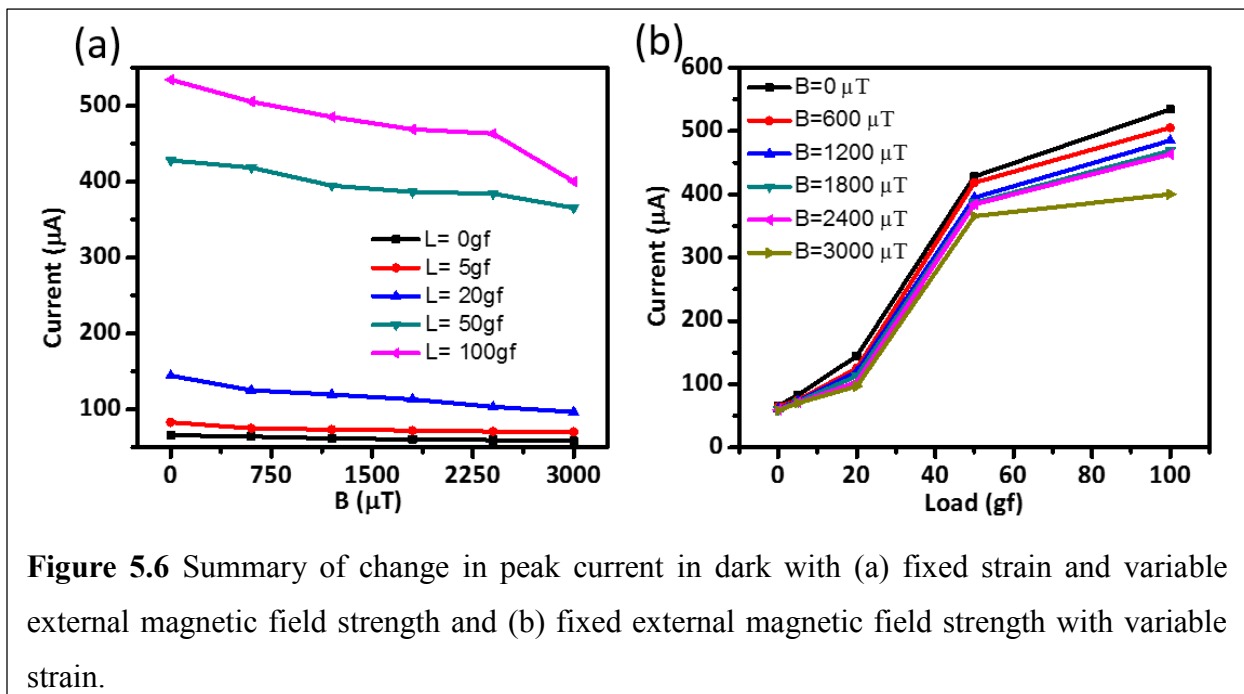


Figure 5.5 Typical I - V characteristic of ZnO nanowire array based piezo-magneto sensor in dark under fixed compressional loads of (a) 0gf, (b) 5gf, (c) 20 gf, (d) 50 gf, and (e) 100 gf with varying magnetic field strengths of 0-3000 μ T. In each measurement condition the decreasing trend in peak current (insets) with increasing magnetic field strength is preserved.

Similar measurements were repeated on the same piezotronic device with fixed compressional loads at a time and by varying the magnetic field strengths only to examine the reproducibility and the data is summarized in Figure 5.5. It is confirmed that the decreasing trend in peak current with increasing magnetic field strength is unchanged and that the total amount of decrease in peak current with magnetic field is nominal in the absence of strain whereas the total decrease is more pronounced when the strain is present. The observation certainly infers the inherent coupling of piezotronic effect with external magnetic field. The detailed mechanism of coupling will be discussed subsequently.

The measurement results from Figure 5.3 and 5.5 are summarized in Figure 5.6 where Figure 5.6 (a) is the summary plot of I - V measurements performed at fixed compressional loads of 0-100 gf with respect to varying magnetic field strength of 0-3000 μ T and Figure 5.6 (b) is summary of measurements performed at fixed magnetic field strengths of 0-3000 μ T with respect to variable compressional loads of 0-100 gf.



A step by step increase in absolute current with increasing load amount from 0 to 100 gf is seen in Figure 5.6 (a) with linear decrease in peak current at each load with increasing magnetic field strength. The decrease is gradual and free of any inflection points suggesting that the effect of external magnetic field is rather continuous. The same inference can also be drawn from Figure 5.6 (b) where absolute current shows more pronounced linear increase with compressional load as compared to modest decrease in peak current with increasing magnetic field strength. From Figure 5.6 (a-b) it is apparently clear that the compressional load has stronger effect on current than the magnetic field only and this feature is retained even when load and magnetic field is combined together indicating that the influence of compressional load and external magnetic field are essentially independent of each other but can affect the device performance synergistically when present simultaneously.

5.3.3 Working mechanism of piezo-magneto sensor

The working mechanism of ZnO nanowire array piezo-magneto sensor can be demonstrated by band energy diagram and by appropriate incorporation of polarization charges generated by compressional load and by including external magnetic field. Figure 5.7 illustrates the detailed band diagram of Ag-ZnO nanowire array in various conditions, where Figure 5.7 (a) is the band energy diagram of Ag and ZnO, assuming that no metallurgical contact is established and CBM, VBM and Fermi levels are displayed accordingly. No charge transfer occurs at this point to compensate the relative Fermi level difference. In Figure 5.7 (b), the metallurgical contact between Ag and ZnO was established and equilibrium was achieved for Fermi level realignment after thermally generated electron transfer from CBM of ZnO to metal side, thus creating a downward slope in CBM and VBM in proximity of Ag-ZnO interface leading to creation of depletion zone of width W and a barrier (V_b) for further electron diffusion from ZnO to Ag side.

Under applied forward bias (V) the built in barrier potential is reduced by applied the amount of applied bias ($V_b - V$) leading to diffusion of majority electrons from ZnO to Ag manifested by forward current in I - V measurements. When external compressional load is applied polarization charges are created in ZnO nanowire,³⁸ especially the positive polarity of charges created along in ZnO interior along ZnO-Ag interface, as seen in Figure 5.7 (c), lowers the barrier height thereby allowing diffusion of more electrons resulting in increase in forward current. As the compressional load increases the elastic deformation of ZnO increases creating more polarization charges and further lowering of CBM and VBM takes place leading to higher forward current, however the total majority diffusion current across ZnO-Ag interface is limited by the number of thermally generated electron-hole pairs in ZnO and by structural integrity imposed elastic deformation limit of ZnO nanowires, which means that current can only increase to certain extent. When external magnetic field is applied (Figure 5.7 (d)) in presence of forward bias and compressional load the free charge carriers experience Lorentz force which deflects the electrons and holes in opposite directions. The magnetic field was applied parallel to Ag-ZnO interface that is also perpendicular to c -axis (z -axis or \perp to substrate normal) of ZnO nanowire growth direction, the simplest form of Lorentz force on electrons can be written as:

$$F_{L,-y} = ev_z B_{-x}$$

where, e is the electronic charge, v is electron velocity and B is magnetic field strength. The components of magnetic field, Lorentz force and electron velocity is considered in $-x$, $-y$ and z directions, respectively. The deflection force on electrons accumulates them along the surface of ZnO nanowires where they were trapped by surface defects of ZnO, thereby reducing the number of available free electrons leading to a decrease in conductance or increase in resistance.³⁹ The altered conductance in presence of external magnetic field then results in reduction of forward

current. As the strength of magnetic field increases the Lorentz deflection force on majority electrons becomes stronger and the decrease in forward current is more prominent as summarized in Figure 5.6 (a).

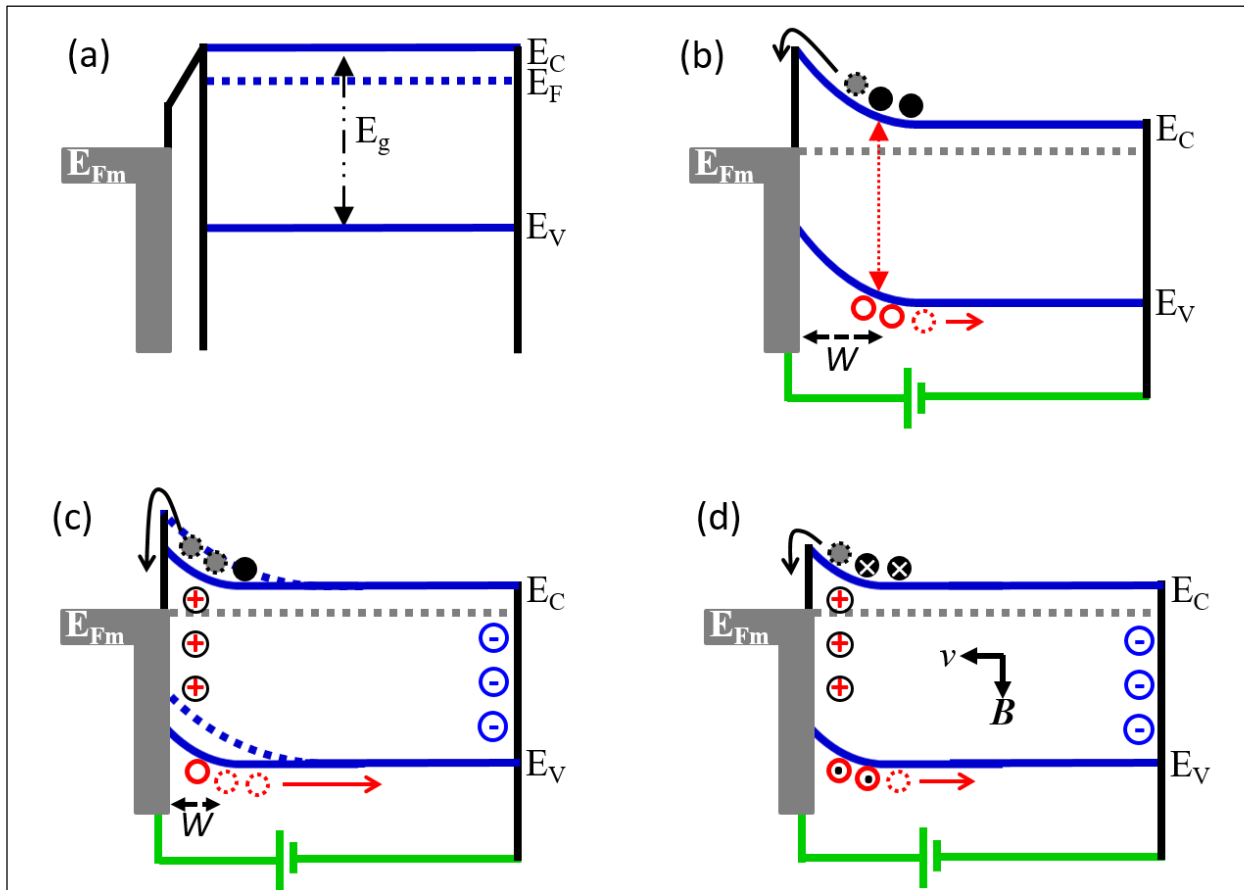


Figure 5.7 Working mechanism of ZnO nanowire array piezo-magneto sensor, where (a) represents the energy band diagram of Ag-ZnO before metallurgical contact is made, (b) after contact in equilibrium under external forward bias and in dark, (c) under compressional load generated polarization charge at inner surface of ZnO in proximity of Ag-ZnO interface, and (d) under influence of external magnetic field applied parallel to the Ag-ZnO interface and perpendicular to c-axis of ZnO nanowire growth. Direction of Lorentz force is displayed by \times for electrons and by \cdot for holes. Solid lines and circles represent static and dotted ones represent dynamic condition where band position are altered (dotted blue lines) and dotted circles (empty/filled) represents charge carrier flow direction with arrows.

5.3.4 ZnO nanowire array piezo-magneto-photo sensor

To further investigate the effect of external magnetic field on the performance of ZnO nanowire array piezo-phototronic device, I - V measurements were carried out on the same device under UV ($\lambda = 385$ nm) illumination in presence of magnetic field. Figure 5.8 (a) is the result of I - V measurements under steady UV illumination density of 1.32 mW/cm^2 with increasing compressional loads and in the absence of external magnetic field. The device was soaked under UV illumination for sufficiently long time in order to saturate the device which ensures no further increase in the peak current from illumination only. Compared to dark current value of $\sim 65 \text{ }\mu\text{A}$, the photocurrent under UV illumination attains a value of 1.15 mA at no strain and no external field which is an order of magnitude (~ 18 times) enhancement. Keeping the illumination steady, increase in compressional load results in higher photocurrent as seen in Figure 5.8 (a), where it attains a value of 5.5 mA at 100 gf load accounting to 85 times increase compared to dark current. Maintaining the illumination and load, when external magnetic field is applied parallel to Ag-ZnO interface the photocurrent further increases, though the increase in peak photocurrent is small for weak magnetic field strength as is the case for $600 \text{ }\mu\text{T}$ field measurements in Figure 5.8 (b). However, this increment in photocurrent is consistent with each applied load, namely 5 to 100 gf and is reproducible over several measurement cycles. It was also observed that when field is applied parallel to the z -axis (along c -axis of nanowire growth) no change in photocurrent was recorded, indicating that photocurrent has directional dependence on the external magnetic field. A similar trend in increasing photocurrent was observed when magnetic field strength was increased from $600 \text{ }\mu\text{T}$ to $1200 \text{ }\mu\text{T}$ where peak photocurrent at 100 gf was recorded to be 5.75 mA . As the field strength increases the photocurrent becomes higher and higher for each compressional load, reaching to a value of 5.9 mA at 100 gf for $3000 \text{ }\mu\text{T}$ of field strength.

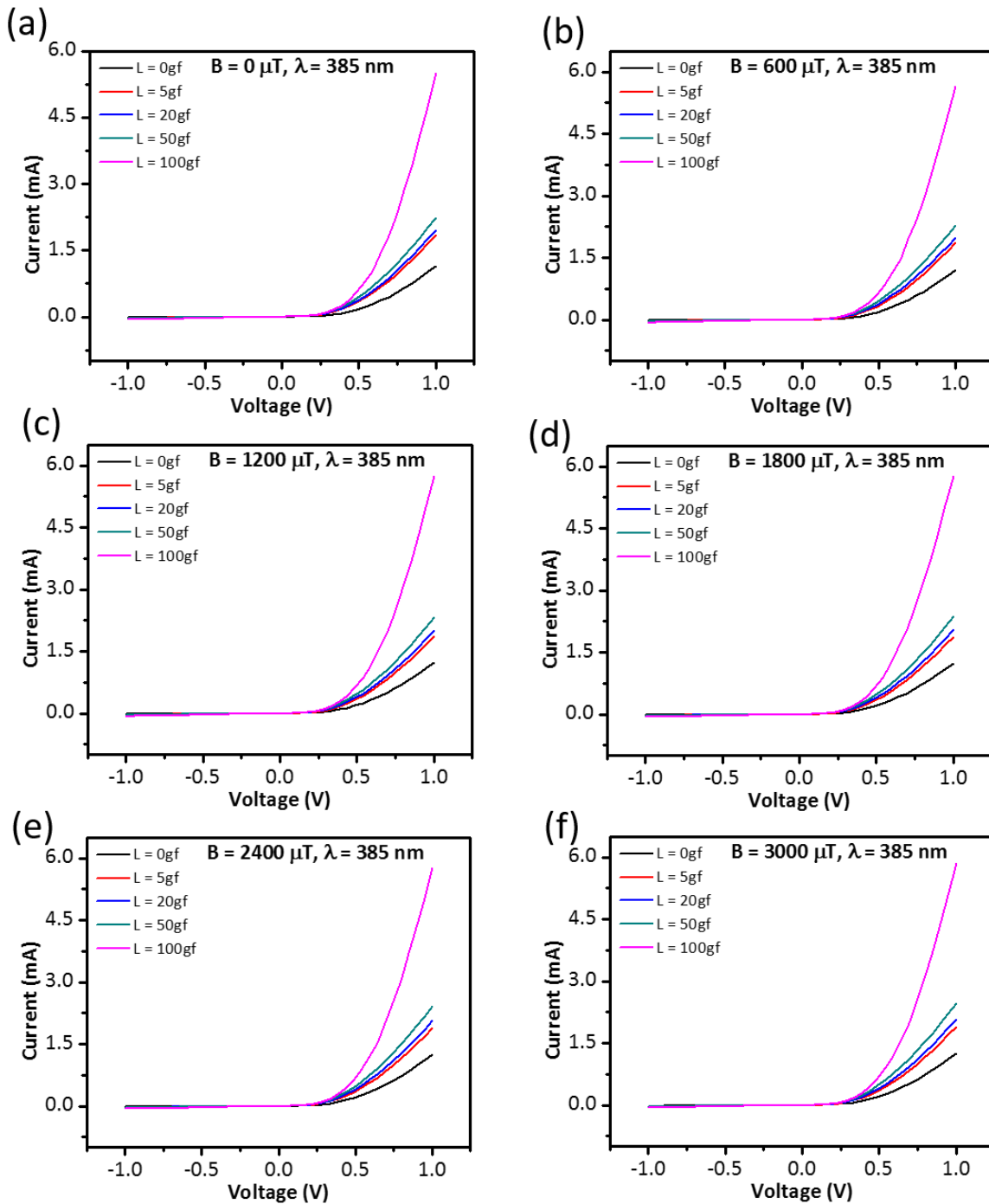


Figure 5.8 Typical I - V characteristic of ZnO nanowire array based piezo-magneto-photo sensor under UV illumination density of 1.32 mW/cm^2 (a) compressional strain only and (b-f) under compressional strain combined with 600-3000 μT of external magnetic field. A gradual increase in peak current is apparent with increasing magnetic field strength under steady UV illumination density.

Similar measurements were also performed to further investigate the reproducibility of the measurement and robustness of the device under steady state UV illumination density of 1.32 mW/cm^2 , fixed compressional load and variable magnetic field strength of 600 to 3000 μT . The measurement results are illustrated in Figure 5.9. *I-V* response of the device in dark and under steady state UV illumination density of 1.32 mW/cm^2 only is presented in Figure 5.9 (a) showing manifold increase in photocurrent compared to dark current. Figure 5.9 (b) is the *I-V* measurement performed under steady state UV illumination density of 1.32 mW/cm^2 with varying external magnetic field strength of 0 to 3000 μT and in absence of compressional load. The inset in Figure 5.9 (b) is the enlarged view of the changes in the photocurrent under external magnetic field influence where peak photocurrent increases gradually with increasing strength of magnetic field attaining a value of 1.26 mA at 3000 μT compared to 1.15 mA in the absence of magnetic field amounting to a total change of $\sim 10\%$. Similar nominal increment in peak current was also observed for intermediate magnetic field strengths applied. Figure 5.9 (c) represents the result of *I-V* measurements of the device under steady state UV illumination density of 1.32 mW/cm^2 at a fixed load of 5gf and varying magnetic field strength of 0 to 3000 μT . The measured peak photocurrent under steady state UV illumination with 5 gf compressional load was found to be 1.8 mA which is significantly higher than the peak photocurrent value of 1.15 mA observed for steady state UV illumination in absence of compressional load. The peak photocurrent further increases as the magnetic field is applied and rises with increase in magnetic field strength. The total amount of increase in the photocurrent under external magnetic field at 5 gf load and 3000 μT was found to be $\sim 6\%$. A similar trend of increase in photocurrent with increasing magnetic field strength was also observed for 20, 50 and 100 gf loads and measurement plots are shown in Figures 5.9 (d-f).

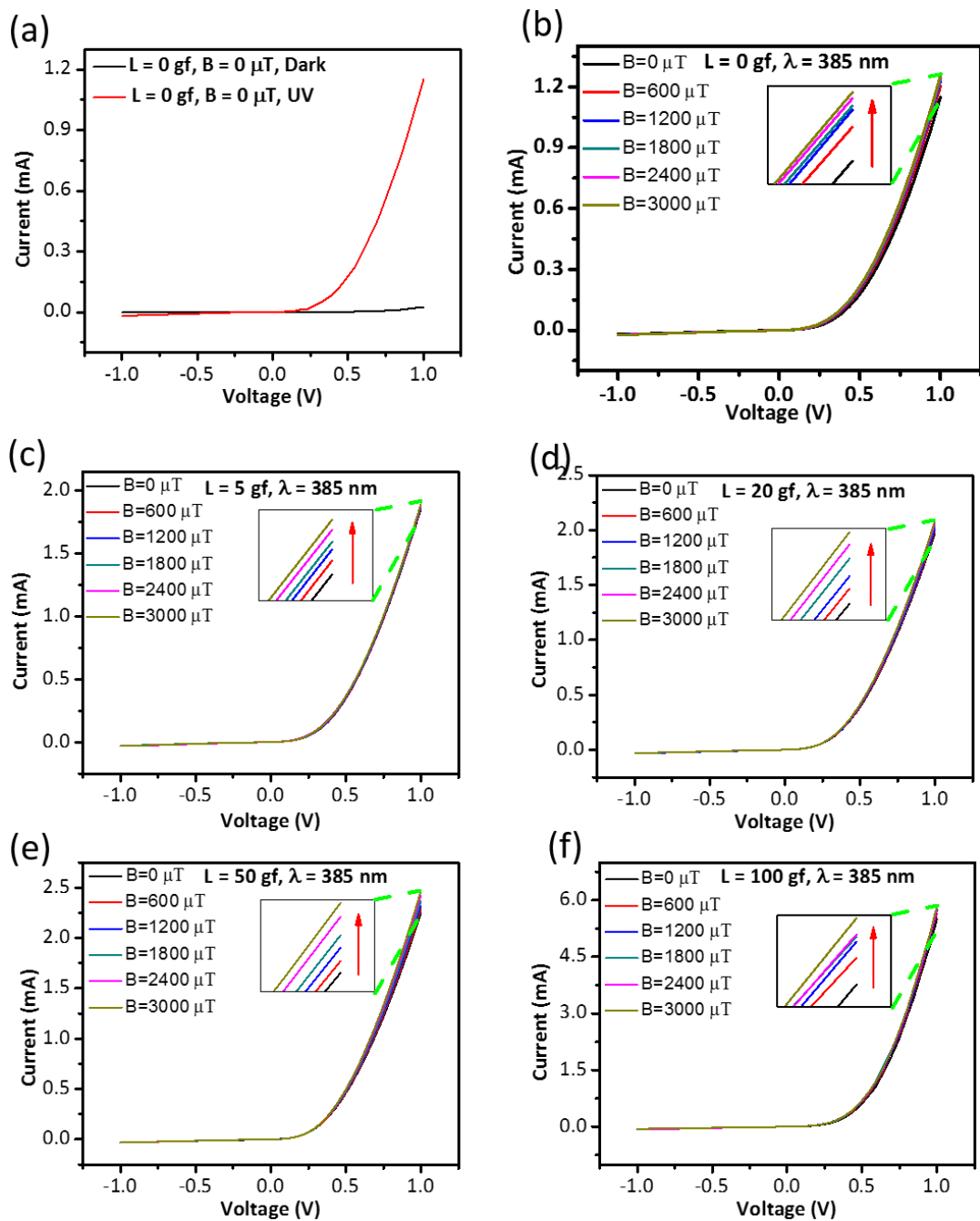
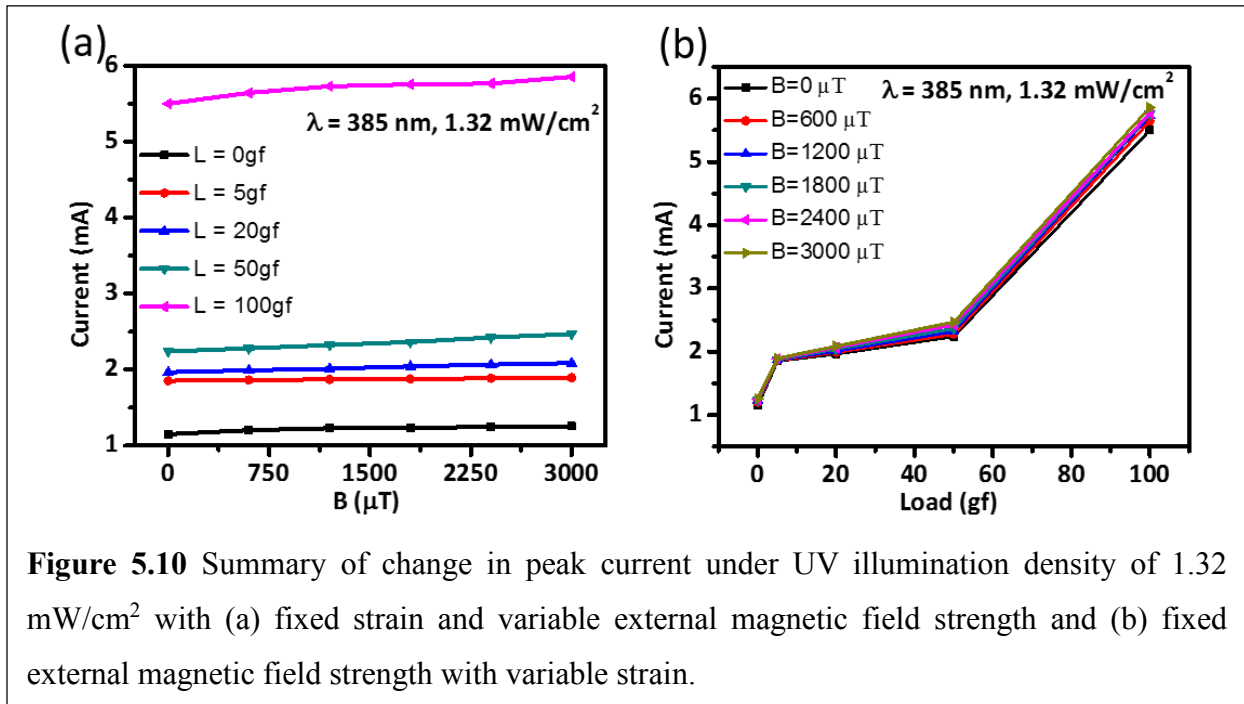


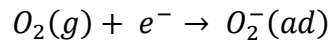
Figure 5.9 *I-V* measurements of ZnO nanowire array piezo-magneto-photo sensor in (a) dark and under UV illumination density of 1.32 mW/cm^2 (b) steady state UV illumination density of 1.32 mW/cm^2 combined with varying magnetic field strengths of 600 to 3000 μ T, and (c-f) in presence of steady state UV illumination and fixed loads of 5, 20, 50 and 100 gf with variable magnetic field strength of 600 to 3000 μ T, respectively in each load condition. Insets represents the enlarged view of the changes in peak current.

The measurement results from Figure 5.8 and 5.9 are summarized in figure 5.10, where 5.10 (a) is the summary plot of I - V measurements performed under steady state UV illumination density of 1.32 mW/cm^2 at various fixed loads ranging from 0 to 100 gf and variable magnetic field strength of 0 to 3000 μT for each load condition. As can be seen, in Figure 5.10 (a), at each fixed load the increase in magnetic field strength results in enhanced photocurrent where magnitude of enhancement varies with field strength. This clearly demonstrates the coupling of external magnetic field with piezo-phototronic effect. Figure 5.10 (b) is a plot of peak photocurrent variation with fixed magnetic field strengths of 0 to 3000 μT with changing loads from 0 to 100 gf for each magnetic field applied. It is apparent after comparison of Figure 5.10 (a) and (b) that the inner piezopotential has stronger effect on the peak photocurrent as compared to the external magnetic field only and both can be coupled together to achieve enhanced current.



5.3.5 Working mechanism of piezo-magneto-photo sensor

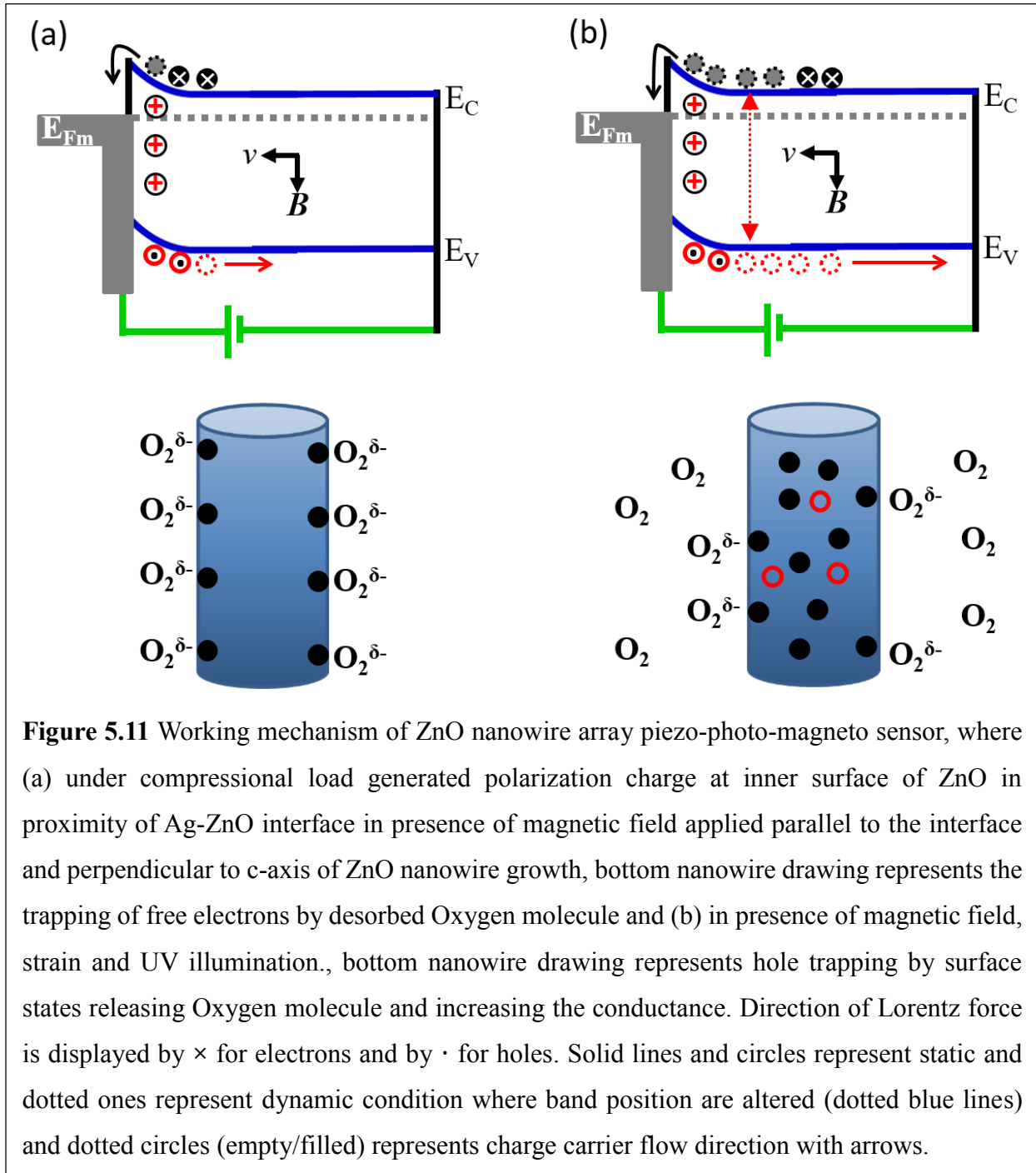
The mechanism of piezo-magneto-photo coupling can be understood through relative band alignment between Ag-ZnO and a representative drawing of molecular Oxygen adsorption-desorption on high surface area ZnO nanowire concurrently with Lorentz force mediated deflection of free charge carriers in presence of external magnetic field illustrated in Figure 5.11. Figure 5.11(a) is band diagram of Ag-ZnO under compressional strain and external magnetic field applied parallel to the interface. The bottom drawing represents a typical nanowire surface under ambient where surface adsorbed Oxygen molecules are shown. Due to high surface area, the conductance of ZnO nanowire is significantly affected by surface states which has adsorbed oxygen molecules on the surface. Under dark, limited number of thermally generated free charge carriers are available to contribute to the conductance of ZnO nanowire and any mechanism of free charge carrier removal will significantly decrease the conductance, in other words increase the resistance causing a decrease in current. The adsorbed oxygen molecule on the surface happens to trap the free electrons.⁴⁰⁻⁴¹⁻⁴²⁻⁴³



In the absence of free electrons near the surface region a low conductivity depletion layer is formed. When external magnetic field is present, the Lorentz deflection force tends to accumulate the electrons near the surface which increases the number of adsorbed oxygen molecules hence increasing the width of low conduction depletion layer.³⁹ Alternatively, the dependence of nanowire resistance on oxygen partial pressure can be written as⁴⁴

$$R_{NW} \propto p(O_2)^n$$

In our case, the oxygen partial pressure is proportional to the free electrons accumulation on the nanowire surface which in turn is dependent on the direction and strength of magnetic field applied.

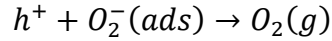


This relationship can be described as follows:³⁵

$$R_{NW} \propto p(O_2)^n \propto B_{app}$$

where, R_{NW} is the resistance of the nanowire, $p(O_2)^n$ is ambient oxygen partial pressure at nanowire surface and n is empirically calculated index with numerical value between 0 and 1, B_{app} is external magnetic field strength. As the magnetic field strength parallel to Ag-ZnO interface increases, it deflects higher number of free electrons to the surface of the nanowires which gets trapped by surface adsorbed oxygen molecules leaving behind a low conducting depletion layer and increased resistance of the individual nanowires.

In the presence of UV illumination (Figure 5.11 (b)), electron-hole pairs are generated in ZnO nanowires leading to hole migration to the surface arising from potential slope produced by band bending and discharging the negatively charged adsorbed oxygen molecules, consequently oxygen is photo desorbed (Figure 5.11 (b), bottom nanowire) from the nanowire surface:



The unpaired electrons then result in increased conductance of ZnO nanowire resulting in significantly increased photocurrent. At fixed UV illumination density, increase in magnetic field could only slightly deflect the holes to the surface trap states as the band bending has stronger effect on hole migration which predominantly dictates the conductance of the nanowires, therefore only slight increase in photocurrent was observed with increasing magnetic field strength.

5.4 Conclusions

In summary, influence of external magnetic field was investigated on ZnO nanowire array based piezotronic and piezo-phototronic device. It is observed that the external magnetic field has

notable effect on the ZnO nanowire array piezotronic device where coupling of external magnetic field applied parallel to Ag-ZnO interface results in reduced current because of Lorentz force induced deflection of free charge carriers, in particular majority electrons in intrinsically *n-type* ZnO nanowire array piezotronic device. Furthermore, in presence of steady state UV illumination and fixed compressional load, externally applied magnetic field causes an increase in photocurrent which increases almost linearly with higher magnetic field strengths. The effect of external magnetic field on piezotronic and piezo-phototronic ZnO nanowire array device was discussed qualitatively through energy band diagram and relative band bending caused by inner piezo charges appearing at the interface of Ag-ZnO. From *I-V* measurement performed under compressional load, UV illumination and magnetic field, it is apparent that magnetic field strength affects the conductance of nanowires *via* surface trap states tuning. The device exhibits multiple functionality in its ability to detect external stimuli such as pressure in form of compressional load, illumination in form of UV wavelength and magnetic field of variable strength and their combination as well.

References

1. Nalwa, H. S., *Handbook of Advanced Electronic and Photonic Materials and Devices*. Academic Press: 2000.
2. Vaseashta, A.; Dimova-Malinovska, D., Nanostructured and nanoscale devices, sensors and detectors. *Science and Technology of Advanced Materials* **2005**, *6* (3–4), 312-318.
3. Mamalis, A. G., Recent advances in nanotechnology. *Journal of Materials Processing Technology* **2007**, *181* (1–3), 52-58.
4. Vaseashta, A. K.; Dimova-Malinovska, D.; Marshall, J. M., *Nanostructured and Advanced Materials for Applications in Sensor, Optoelectronic and Photovoltaic Technology: Proceedings of the NATO Advanced Study Institute on Nanostructured and Advanced Materials for Applications in Sensors, Optoelectronic and Photovoltaic Technology Sozopol, Bulgaria, 6-17 September 2004*. Springer Netherlands: 2007.
5. Yan, R.; Gargas, D.; Yang, P., Nanowire photonics. *Nat Photon* **2009**, *3* (10), 569-576.
6. Wiederrecht, G., *Handbook of Nanoscale Optics and Electronics*. Elsevier Science: 2010.
7. Katz, H. E., Chemically Sensitive Field-Effect Transistors and Chemiresistors: New Materials and Device Structures. *Electroanalysis* **2004**, *16* (22), 1837-1842.
8. Sun, B.; Siringhaus, H., Solution-Processed Zinc Oxide Field-Effect Transistors Based on Self-Assembly of Colloidal Nanorods. *Nano Letters* **2005**, *5* (12), 2408-2413.
9. Choi, Y.; Park, W.-Y.; Kang, M. S.; Yi, G.-R.; Lee, J.-Y.; Kim, Y.-H.; Cho, J. H., Monolithic Metal Oxide Transistors. *ACS Nano* **2015**, *9* (4), 4288-4295.
10. Saito, Y., *Carbon Nanotube and Related Field Emitters: Fundamentals and Applications*. Wiley: 2010.
11. Gaurav, M.; Indranil, L., Recent progress in nanostructured next-generation field emission devices. *Journal of Physics D: Applied Physics* **2014**, *47* (32), 323001.

12. Swanwick, M. E.; Keathley, P. D.; Fallahi, A.; Krogen, P. R.; Laurent, G.; Moses, J.; Kärtner, F. X.; Velásquez-García, L. F., Nanostructured Ultrafast Silicon-Tip Optical Field-Emitter Arrays. *Nano Letters* **2014**, *14* (9), 5035-5043.
13. Chen, D. D.; Michael, E. S.; Phillip, D. K.; Franz, X. K.; Luis, F. V.-G., Multiplexing and scaling-down of nanostructured photon-triggered silicon field emitter arrays for maximum total electron yield. *Nanotechnology* **2015**, *26* (26), 265202.
14. Hegg, M. C.; Horning, M. P.; Baehr-Jones, T.; Hochberg, M.; Lin, L. Y., Nanogap quantum dot photodetectors with high sensitivity and bandwidth. *Applied Physics Letters* **2010**, *96* (10), 101118.
15. Strzhemechny, Y., Recent Advances in the Design of Photodetectors Based on Thin-Film and Nanostructured ZnO. In *Nanoscale Sensors*, Li, S.; Wu, J.; Wang, Z. M.; Jiang, Y., Eds. Springer International Publishing: 2013; Vol. 19, pp 153-188.
16. Yu, K.; Chen, J., Enhancing Solar Cell Efficiencies through 1-D Nanostructures. *Nanoscale Research Letters* **2009**, *4* (1), 1-10.
17. Nozik, A. J., Nanoscience and Nanostructures for Photovoltaics and Solar Fuels. *Nano Letters* **2010**, *10* (8), 2735-2741.
18. Polman, A.; Atwater, H. A., Photonic design principles for ultrahigh-efficiency photovoltaics. *Nat Mater* **2012**, *11* (3), 174-177.
19. Yu, M.; Long, Y.-Z.; Sun, B.; Fan, Z., Recent advances in solar cells based on one-dimensional nanostructure arrays. *Nanoscale* **2012**, *4* (9), 2783-2796.
20. Jagadish, C.; Pearton, S. J., *Zinc Oxide Bulk, Thin Films and Nanostructures: Processing, Properties, and Applications*. Elsevier Science: 2011.
21. Zhai, T.; Fang, X.; Liao, M.; Xu, X.; Zeng, H.; Yoshio, B.; Golberg, D., A Comprehensive Review of One-Dimensional Metal-Oxide Nanostructure Photodetectors. *Sensors (Basel, Switzerland)* **2009**, *9* (8), 6504-6529.

22. Yu, J. S.; Ko, Y. H.; Nagaraju, G. In *Low-dimensional II-VI oxide-based semiconductor nanostructure photodetectors for light sensing*, 2015; pp 93702X-93702X-8.
23. Wang, Z. L.; Song, J., Piezoelectric Nanogenerators Based on Zinc Oxide Nanowire Arrays. *Science* **2006**, *312* (5771), 242-246.
24. Wang, X.; Song, J.; Liu, J.; Wang, Z. L., Direct-Current Nanogenerator Driven by Ultrasonic Waves. *Science* **2007**, *316* (5821), 102-105.
25. Pradel, K. C.; Wu, W.; Ding, Y.; Wang, Z. L., Solution-Derived ZnO Homojunction Nanowire Films on Wearable Substrates for Energy Conversion and Self-Powered Gesture Recognition. *Nano Letters* **2014**, *14* (12), 6897-6905.
26. Yang, Q.; Guo, X.; Wang, W.; Zhang, Y.; Xu, S.; Lien, D. H.; Wang, Z. L., Enhancing Sensitivity of a Single ZnO Micro-/Nanowire Photodetector by Piezo-phototronic Effect. *ACS Nano* **2010**, *4* (10), 6285-6291.
27. Zhang, Z.; Liao, Q.; Yu, Y.; Wang, X.; Zhang, Y., Enhanced photoresponse of ZnO nanorods-based self-powered photodetector by piezotronic interface engineering. *Nano Energy* **2014**, *9* (0), 237-244.
28. Yu, R.; Pan, C.; Chen, J.; Zhu, G.; Wang, Z. L., Enhanced Performance of a ZnO Nanowire-Based Self-Powered Glucose Sensor by Piezotronic Effect. *Advanced Functional Materials* **2013**, *23* (47), 5868-5874.
29. Yang, Q.; Wang, W.; Xu, S.; Wang, Z. L., Enhancing Light Emission of ZnO Microwire-Based Diodes by Piezo-Phototronic Effect. *Nano Letters* **2011**, *11* (9), 4012-4017.
30. Lin Wang, Z. In *Self-powered nanosystem: From nanogenerators to piezotronics*, Solid-State and Integrated Circuit Technology (ICSICT), 2010 10th IEEE International Conference on, 1-4 Nov. 2010; 2010; pp 4-4.
31. Wang, Z. L., Piezopotential gated nanowire devices: Piezotronics and piezo-phototronics. *Nano Today* **2010**, *5* (6), 540-552.

32. Kozlov, A. V.; Cheremisinov, A. A.; Polomoshnov, S. A.; Tikhonov, R. D.; Shamanaev, S. V. In *Model of effect of pn-junction magnetic field modulation*, Micro/Nanotechnologies and Electron Devices (EDM), 2011 International Conference and Seminar of Young Specialists on, June 30 2011-July 4 2011; 2011; pp 137-139.
33. Mohaghegh, A.; Cristoloveanu, S.; De Pontcharra, J., Double-injection phenomena under magnetic field in SOS films: A new generation of magnetosensitive microdevices. *Electron Devices, IEEE Transactions on* **1981**, 28 (3), 237-242.
34. Dunstan, W., Variation of Photovoltaic Response with Magnetic Field for a Germanium p-n Junction. *Proceedings of the Physical Society* **1961**, 77 (2), 459.
35. Lu, M.-L.; Weng, T.-M.; Chen, J.-Y.; Chen, Y.-F., Ultrahigh-gain single SnO₂ nanowire photodetectors made with ferromagnetic nickel electrodes. *NPG Asia Mater* **2012**, 4, e26.
36. Joo, S.; Kim, T.; Shin, S. H.; Lim, J. Y.; Hong, J.; Song, J. D.; Chang, J.; Lee, H.-W.; Rhie, K.; Han, S. H.; Shin, K.-H.; Johnson, M., Magnetic-field-controlled reconfigurable semiconductor logic. *Nature* **2013**, 494 (7435), 72-76.
37. Xue, F.; Zhang, L.; Feng, X.; Hu, G.; Fan, F.; Wen, X.; Zheng, L.; Wang, Z., Influence of external electric field on piezotronic effect in ZnO nanowires. *Nano Res.* **2015**, 8 (7), 2390-2399.
38. Gao, Y.; Wang, Z. L., Equilibrium Potential of Free Charge Carriers in a Bent Piezoelectric Semiconductive Nanowire. *Nano Letters* **2009**, 9 (3), 1103-1110.
39. Soci, C.; Zhang, A.; Xiang, B.; Dayeh, S. A.; Aplin, D. P. R.; Park, J.; Bao, X. Y.; Lo, Y. H.; Wang, D., ZnO Nanowire UV Photodetectors with High Internal Gain. *Nano Letters* **2007**, 7 (4), 1003-1009.
40. Li, Q. H.; Liang, Y. X.; Wan, Q.; Wang, T. H., Oxygen sensing characteristics of individual ZnO nanowire transistors. *Applied Physics Letters* **2004**, 85 (26), 6389-6391.
41. Fan, Z.; Chang, P.-c.; Lu, J. G.; Walter, E. C.; Penner, R. M.; Lin, C.-h.; Lee, H. P., Photoluminescence and polarized photodetection of single ZnO nanowires. *Applied Physics Letters* **2004**, 85 (25), 6128-6130.

42. Sanjeev, K.; Vinay, G.; Sreenivas, K., Synthesis of photoconducting ZnO nano-needles using an unbalanced magnetron sputtered ZnO/Zn/ZnO multilayer structure. *Nanotechnology* **2005**, *16* (8), 1167.
43. Li, Q. H.; Gao, T.; Wang, Y. G.; Wang, T. H., Adsorption and desorption of oxygen probed from ZnO nanowire films by photocurrent measurements. *Applied Physics Letters* **2005**, *86* (12), 123117.
44. Hernandez-Ramirez, F.; Prades, J. D.; Tarancon, A.; Barth, S.; Casals, O.; Jimenez-Diaz, R.; Pellicer, E.; Rodriguez, J.; Morante, J. R.; Juli, M. A.; Mathur, S.; Romano-Rodriguez, A., Insight into the Role of Oxygen Diffusion in the Sensing Mechanisms of SnO₂ Nanowires. *Advanced Functional Materials* **2008**, *18* (19), 2990-2994.

Chapter 6 Conclusion and Perspective

The focus of this dissertation is on the piezo-phototronic device application of type-II core/shell nanowire heterostructures and development of new type of sensor integrated on 3D nanowire arrays which utilizes the coupling of multiple intrinsic properties and study the performance of this sensor under external stimuli.

Two case studies have been done to successfully demonstrate highly efficient piezo-phototronic photodetector. In Chapter 3, a broadband piezo-phototronic photodetector based on type-II CdSe/ZnTe core/shell nanowire array is fabricated which exhibits enhanced performance under compressional load and several orders of enhancement observed in device performance highlights the importance of nearly lattice matched interface leading to reduced recombination losses. In Chapter 4, a prototype photosensing device is fabricated on truly wide band gap type-II ZnO/ZnS core/shell nanowire array. In spite of fully wide band gap core and shell material components, the device can efficiently detect photons of energies much smaller than the band gap of either core or shell, an effect arising from the indirect transfer of electrons from VBM of ZnS to CBM of ZnO and also because of the abrupt nature of interface which drastically reduces the recombination losses. The device performance is further improved by application of piezo-phototronic effect. A PL study was performed to investigate and confirm the indirect type-II transition and to quantify the indirect band gap.

A new type of prototype piezo-photo-magnetotronic sensor device is integrated on 3D ZnO nanowire array grown on ITO substrate and findings are discussed in Chapter 5. It is observed that external magnetic field has distinct effect on piezotronic and piezo-phototronic behavior of ZnO

nanowire array arising from coupling of piezoelectric, semiconducting and electrical/optical properties and Lorentz force induced deflection of majority carrier electrons in n-type ZnO leads to magnetoconcentration effect altering the conductance of the nanowires in dark and under UV illumination.

However, the field of 3D type-II core/shell nanowire array piezo-phototronic is still in nascent stage and demands further investigation from materials perspective to incorporate other radial heterostructures in order to enrich the family of piezo-phototronics devices. The field of piezo-photo-magnetotronic is a new class of sensorics and more work is underway to completely understand the underlying mechanism of this effect and to develop a sound theoretical background so that the principle can be translated to achieve improved performance of device fabricated on other materials systems such as CdSe, CdS, CdTe and designed materials heterostructures such as CdSe/ZnTe, ZnO/ZnS type of core/shell nanowire arrays. Furthermore, single nanowire array based device study is also necessary to establish theoretical framework and simulation studies are important to critically validate the findings. These devices have the potential of multiple functionalities which can be used to detect various stimuli such as magnetic field, illumination and pressure all at once or one at a time.

Appendix: Copyright Permissions



RightsLink[®]

[Home](#)[Account Info](#)[Help](#)

Title: Nanostructured materials for photon detection
Author: Gerasimos Konstantatos, Edward H. Sargent
Publication: Nature Nanotechnology
Publisher: Nature Publishing Group
Date: May 16, 2010

Logged in as:
Satish Rai
Account #:
3000956264

[LOGOUT](#)

Copyright © 2010, Rights Managed by Nature Publishing Group

Order Completed

Thank you very much for your order.

This is a License Agreement between Satish C Rai ("You") and Nature Publishing Group ("Nature Publishing Group"). The license consists of your order details, the terms and conditions provided by Nature Publishing Group, and the [payment terms and conditions](#).

[Get the printable license.](#)

License Number	3715990850875
License date	Sep 25, 2015
Licensed content publisher	Nature Publishing Group
Licensed content publication	Nature Nanotechnology
Licensed content title	Nanostructured materials for photon detection
Licensed content author	Gerasimos Konstantatos, Edward H. Sargent
Licensed content date	May 16, 2010
Type of Use	reuse in a dissertation / thesis
Volume number	5
Issue number	6
Requestor type	academic/educational
Format	electronic
Portion	figures/tables/illustrations
Number of figures/tables/illustrations	3
High-res required	no
Figures	Figure 1,2,3
Author of this NPG article	no
Your reference number	None
Title of your thesis / dissertation	Three dimensional core/shell nanowire piezo-phototronic photo sensors
Expected completion date	Oct 2015
Estimated size (number of pages)	150
Total	0.00 USD



RightsLink®

Home

Create Account

Help



ACS Publications
Most Trusted. Most Cited. Most Read.

Title: Piezotronic and Piezophototronic Effects
Author: Zhong Lin Wang
Publication: Journal of Physical Chemistry Letters
Publisher: American Chemical Society
Date: May 1, 2010

Copyright © 2010, American Chemical Society

LOGIN

If you're a [copyright.com](#) user, you can login to RightsLink using your [copyright.com](#) credentials. Already a [RightsLink](#) user or want to [learn more?](#)

PERMISSION/LICENSE IS GRANTED FOR YOUR ORDER AT NO CHARGE

This type of permission/license, instead of the standard Terms & Conditions, is sent to you because no fee is being charged for your order. Please note the following:

- Permission is granted for your request in both print and electronic formats, and translations.
- If figures and/or tables were requested, they may be adapted or used in part.
- Please print this page for your records and send a copy of it to your publisher/graduate school.
- Appropriate credit for the requested material should be given as follows: "Reprinted (adapted) with permission from (COMPLETE REFERENCE CITATION). Copyright (YEAR) American Chemical Society." Insert appropriate information in place of the capitalized words.
- One-time permission is granted only for the use specified in your request. No additional uses are granted (such as derivative works or other editions). For any other uses, please submit a new request.

If credit is given to another source for the material you requested, permission must be obtained



Book: Physics of Semiconductor Devices, 3rd Edition
Author: Simon M. Sze, Kwok K. Ng
Publisher: John Wiley and Sons
Date: Oct 1, 2006
 Copyright © 2006, John Wiley and Sons

Logged in as:
 Satish Rai
 Account #:
 3000956264

[LOGOUT](#)

Order Completed

Thank you for your order.

This Agreement between Satish C Rai ("You") and John Wiley and Sons ("John Wiley and Sons") consists of your order details and the terms and conditions provided by John Wiley and Sons and Copyright Clearance Center.

License number	Reference confirmation email for license number
License date	Sep 24, 2015
Licensed Content Publisher	John Wiley and Sons
Licensed Content Publication	Wiley Books
Licensed Content Title	Physics of Semiconductor Devices, 3rd Edition
Licensed Content Author	Simon M. Sze, Kwok K. Ng
Licensed Content Date	Oct 1, 2006
Licensed Content Pages	832
Type of use	Dissertation/Thesis
Requestor type	University/Academic
Format	Electronic
Portion	Text extract
Number of Pages	20
Will you be translating?	No
Title of your thesis / dissertation	Three dimensional core/shell nanowire piezo-phototronic photo sensors
Expected completion date	Oct 2015
Expected size (number of pages)	150
Requestor Location	Satish C Rai 1727 Savannah Circle
	O FALLON, MO 63368 United States Attn: Satish C Rai
Billing Type	Invoice
Billing address	Satish C Rai 1727 Savannah Circle
	O FALLON, MO 63368 United States Attn: Satish C Rai
Total	0.00 USD

**SPRINGER LICENSE
TERMS AND CONDITIONS**

Sep 13, 2015

This is a License Agreement between Satish C Rai ("You") and Springer ("Springer") provided by Copyright Clearance Center ("CCC"). The license consists of your order details, the terms and conditions provided by Springer, and the payment terms and conditions.

All payments must be made in full to CCC. For payment instructions, please see information listed at the bottom of this form.

License Number	3707290774031
License date	Sep 13, 2015
Licensed content publisher	Springer
Licensed content publication	Springer eBook
Licensed content title	Introduction of Piezotronics and Piezo-Phototronics
Licensed content author	Zhong Lin Wang
Licensed content date	Jan 1, 2012
Type of Use	Thesis/Dissertation
Portion	Figures
Author of this Springer article	No
Order reference number	None
Original figure numbers	don't know yet
Title of your thesis / dissertation	Three dimensional core/shell nanowire piezo-phototronic photo sensors
Expected completion date	Oct 2015
Estimated size(pages)	150
Total	0.00 USD
Terms and Conditions	

**JOHN WILEY AND SONS LICENSE
TERMS AND CONDITIONS**

Sep 09, 2015

This Agreement between Satish C Rai ("You") and John Wiley and Sons ("John Wiley and Sons") consists of your license details and the terms and conditions provided by John Wiley and Sons and Copyright Clearance Center.

License Number	3705121141389
License date	Sep 09, 2015
Licensed Content Publisher	John Wiley and Sons
Licensed Content Publication	Advanced Electronic Materials
Licensed Content Title	Phototronics: Enhanced Broad Band Photodetection through Piezo-Phototronic Effect in CdSe/ZnTe Core/Shell Nanowire Array (Adv. Electron. Mater. 4/2015)
Licensed Content Author	Satish C. Rai,Kai Wang,Jiajun Chen,Jason K. Marmon,Manish Bhatt,Sarah Wozny,Yong Zhang,Weilie Zhou
Licensed Content Date	Apr 16, 2015
Pages	1
Type of use	Dissertation/Thesis
Requestor type	Author of this Wiley article
Format	Electronic
Portion	Full article
Will you be translating?	No
Title of your thesis / dissertation	Three dimensional core/shell nanowire piezo-phototronic photo sensors
Expected completion date	Oct 2015
Expected size (number of pages)	150
Requestor Location	Satish C Rai 1727 Savannah Circle O FALLON, MO 63368 United States Attn: Satish C Rai
Billing Type	Invoice
Billing Address	Satish C Rai 1727 Savannah Circle O FALLON, MO 63368 United States Attn: Satish C Rai



Title: Piezo-phototronic Effect
Enhanced UV/Visible
Photodetector Based on Fully
Wide Band Gap Type-II ZnO/ZnS
Core/Shell Nanowire Array

Logged in as:
Satish Rai

LOGOUT

Author: Satish C. Rai, Kai Wang, Yong
Ding, et al

Publication: ACS Nano

Publisher: American Chemical Society

Date: Jun 1, 2015

Copyright © 2015, American Chemical Society

PERMISSION/LICENSE IS GRANTED FOR YOUR ORDER AT NO CHARGE

This type of permission/license, instead of the standard Terms & Conditions, is sent to you because no fee is being charged for your order. Please note the following:

- Permission is granted for your request in both print and electronic formats, and translations.
- If figures and/or tables were requested, they may be adapted or used in part.
- Please print this page for your records and send a copy of it to your publisher/graduate school.
- Appropriate credit for the requested material should be given as follows: "Reprinted (adapted) with permission from (COMPLETE REFERENCE CITATION). Copyright (YEAR) American Chemical Society." Insert appropriate information in place of the capitalized words.
- One-time permission is granted only for the use specified in your request. No additional uses are granted (such as derivative works or other editions). For any other uses, please submit a new request.

VITA

Satish C. Rai was born in Ghazipur district in the province of Uttar Pradesh, India. He attended University of Allahabad from year 2000-2003 and graduated with a Bachelor's in Physics/Chemistry. He then joined Banaras Hindu University in 2003 and graduated with a Master's of Science in Physics in 2005 and a Master's of Technology in Materials Science and Technology from Institute of Technology (now IIT)-Banaras Hindu University. He then had short stints as a Process Engineer in Falcon Technology International, LLC. in Ras-Al-Khaima, UAE and as a Senior Project Associate at Indian Institute of Technology, Kanpur before joining Advanced Materials Research Institute, University of New Orleans for doctoral study in Spring Semester 2010.